6-3-2019

Cost Effective, Highly Efficient Wireless Power Transfer Systems for EV Battery Charging

Amir Masoud Bozorgi
amir.m.bozorgi@gmail.com

COST EFFECTIVE, HIGHLY EFFICIENT WIRELESS POWER TRANSFER SYSTEMS FOR EV BATTERY CHARGING

A Dissertation

Submitted to Graduate Faculty of the
Louisiana State University and
Agricultural and Mechanical College
in partial fulfillment of the
requirements for the degree of
Doctor of Philosophy

in

The Department of Electrical and Computer Engineering

by
Amir Masoud Bozorgi
B.S, Ferdowsi University of Mashhad, 2010
M.S, Ferdowsi University of Mashhad, 2013
August 2019

ACKNOWLEDGEMENTS

Throughout my PhD program, I have received a great deal of support and assistance.

I would first like to thank my adviser, Dr. Mehdi Farasat, who always was supportive and provided required conditions and tools in pursuit of my research projects.

I would like to acknowledge my internship supervisor at Witricity Co., Dr. Milisav Danilovic, for his wonderful collaboration and great supports during and after my internship. In addition, I would particularly like to thank my friend, Dr. Reza Tavakoli, who provided me extensive guidance in completing my dissertation setup. Also, I am so grateful to my lab mate, Juan Nunez, who was a great help whenever I needed.

Nobody has been more important to me in successful completion of my dissertation than my family members. I would like to thank my parents, whose love and guidance are with me throughout my life. Their happiness is the highest motivation for me. Most importantly, I wish to say my deepest thank to my loving and supportive wife, Maryam, for being besides me in all difficult and long days. You are the best partner in my journey.

TABLE OF CONTENTS

LIST OF TABLES

LIST OF FIGURES

ABSTRACT

The impact of changing inner diameter of wireless power transfer (WPT) coils on coupling coefficient is studied. It is demonstrated that at a certain outer and inner coil diameter, turn space variation has minor effect on the coupling coefficient. Next, two compensation networks, namely primary LCC and secondary LCC, which offer load-independent voltage transfer ratio and zero voltage switching for WPT, are presented. For both compensation networks, the condition for having zero voltage switching operation are derived. In addition, load-independent voltage transfer ratio (VTR) frequencies are obtained and VTR at each frequency is derived. Then, required equations for calculation of WPT system efficiency based on its equivalent circuit are presented. Eventually, by defining a time-weighted transfer average efficiency (TWTAE), and based on measured values of resistance and inductance of a WPT prototype and experimental charging curve of a Li-ion battery, a design procedure for both compensation networks is proposed. The proposed design leads to high TWTAE as well as low material usage. Simulation and experimental results verify the superiority of proposed coil and compensation design compared to conventional one.

1. INTRODUCTION

The problems of depletion of fossil fuels and global warming along with recently introduced restrictions on CO2 emission are among the major forces for driving the societies and governments towards plug-in hybrid electric vehicles (PHEV) and electric vehicle (EV) in the transportation system. The automobile industries have faced an increasing demand and EV sales is expected to reach 5.9 million units by 2020. One of the challenges in development of PHEVs and EVs is to provide convenient and safe battery charging. EV's battery charging methods can be classified into two methods: wired (conductive) and wireless charging.

In the wired charging method, the user connects a cable from the power outlet or charging station to the EV. Wired charging is not convenient due to handling heavy gauge cable or even is dangerous due to tripping hazards, especially in inclement weather. Compared with wired charging, wireless charging has some inherent advantages, such as safety, convenience, reliability, and weather proof [55], [68].

The concept of wireless energy transmission was first proposed by Nikola Tesla in 1899. For the last few decades, wireless power transfer (WPT) technology has been studied and implemented for different applications such as biomedical implants [15], induction heating [16], mobile battery chargers [4], E-bicycle [56], EVs [45], electric buses [61], [69] and trains [21].

WPT technologies are categorized as far field electromagnetic and near field electromagnetic. Microwave and laser radiation, which are categorized as far field, work with radio frequency and can transfer relatively low power (for safety issues) over several meters [17]. On the other hand, near field (non-radiative) electromagnetic, such as inductive coupling, capacitive coupling and magnetic coupling operates with frequency in the range of tens to hundreds of kHz. In near field WPTs, transferred power can be in the level of tens of kW, while transfer distance is limited to a

range of centimeters [19]. Among near field WPTs, due to simplicity and high efficiency, inductive coupling and magnetic coupling are widely used technologies [32]. In both methods, there is one coil in the transmitter (also referred to as primary side) that creates alternating electromagnetic field and there is another coil in the receiver (secondary side) to receive the transferred power. Actually, except higher frequency and use of ferrite, magnetic coupled WPT is no different from inductive coupled WPT, which has been studied for many years [41].

Generally, magnetic coupled WPT systems can be categorized into either distributed or lumped topologies. A distributed system includes a transmitter coil forming a long track and receiver coil(s) coupled to a small portion of the transmitter coil. The distributed system is designed to transfer continuous power. The lumped system consists of two discrete coils at transmitter and receiver placed at a fixed position and is able to transfer power when coils are aligned. The lumped system can be categorized into closely coupled and loosely coupled systems. In closely coupled lumped system, air gaps between coils is relatively small and similar to charge paddles, the user has to plug in the primary [1], [2]. In loosely coupled lumped system, air gap is large and do not need user intervention.

In this report, loosely coupled lumped WPT systems for the application of EVs and PHEVs are investigated. In section 2, fundamentals of magnetic coupled WPT are presented. In section 3, the state of the art of WPT is reviewed. In the next section, factors affecting the coupling coefficient variation in circular and square coils are investigated. Then, in section 5, two compensation topologies with load-independent voltage transfer ratio are presented, and a condition to provide zero voltage switching for both compensation networks are proposed. In section 6, based on equivalent circuit, mathematical equations to calculate efficiency of different stages of WPT system are presented. Next, time-weighted transfer average efficiency concept is presented and

primary and secondary coils are designed based on it. Matlab simulation results are shown and discussed in section 8. Experimental results of a 1.2 kW WPT prototype system are presented in section 9 to verify proposed design methods.

2. FUNDAMENTAL OF WPT

Figure 2.1 depicts typical block diagram of a WPT system. The main principle of operation of a wireless charger and a wired charger is the same. The charger is connected to an AC power. Then, AC voltage is rectified with an AC to DC converter with power factor correction (PFC).

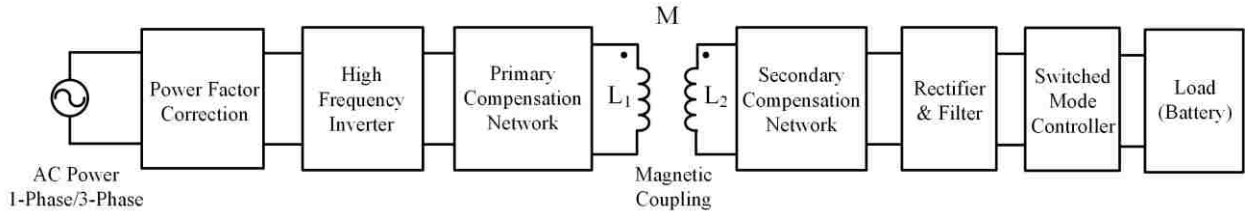

Figure 2.1 WPT system structure.

Afterwards, using a high frequency (HF) DC to AC converter (inverter), DC power is converter to AC. The next stage, in a wired charger, is an isolated transformer, whereas in a WPT charger, is a set of loosely coupled coils. WPT applications may require inclusion of an HF transformer to provide electrical isolation of the WPT primary coupler and cabling from the utility. In the secondary side, there is an HF rectifier and filter. Also, to boost the power transfer capability, a switched mode controller may be employed before load.

To have better idea about the difference between tightly and loosely coupled coils, Figure 2.2 should be taken into account. In this figure, L_1 and L_2 are self-inductances of the primary and secondary coils, respectively. Also, I_1 and I_2 represent the current in the two coils. U_{12} and U_{21} denote induced voltage in the primary and secondary coils, respectively.

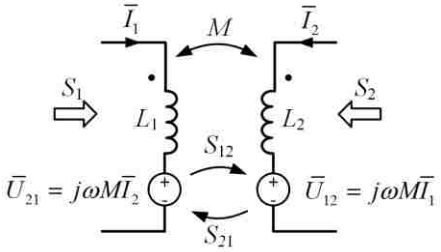

Figure 2.2 Two-coil WPT model

Apparent power going into the primary and secondary coils are shown with S_1 and S_2, respectively. Also, S_{12} and S_{21} are the exchanged power between the primary and secondary coils and calculated as follows [41]

$$\bar{S}_{12} = -\bar{U}_{12}\bar{I}_2^* = -j\omega M\bar{I}_1\bar{I}_2^* = \omega M I_1 I_2 \sin\varphi_{12} - j\omega M I_1 I_2 \cos\varphi_{12}, \quad (2\text{–}1)$$

$$\bar{S}_{21} = -\bar{U}_{21}\bar{I}_1^* = -j\omega M\bar{I}_2\bar{I}_1^* = -\omega M I_1 I_2 \sin\varphi_{12} - j\omega M I_1 I_2 \cos\varphi_{12}. \quad (2\text{–}2)$$

Here, φ_{12} is the phase deference between $\bar{I}_1$ and $\bar{I}_2$. Active power transferred from the primary coil to the secondary coil can be written as follows

$$P_{12} = \omega M I_1 I_2 \sin\varphi_{12}. \quad (2\text{–}3)$$

Maximum active power is transferred for $\varphi_{12}=\pi/2$ .Total reactive power in the two coils system can be expressed as

$$Q = \omega(L_1 I_1^2 + L_2 I_2^2 + 2M I_1 I_2 \cos\varphi_{12}). \quad (2\text{–}4)$$

Higher reactive power means higher magnetizing power, which can increase copper and core losses. To improve transfer efficiency, the active to reactive power ratio should be maximized. This ratio is defined as follows [41]

$$\frac{P_{12}}{Q} = \frac{\omega M I_1 I_2 \sin\varphi_{12}}{\omega(L_1 I_1^2 + L_2 I_2^2 + 2M I_1 I_2 \cos\varphi_{12})} = \frac{k\sqrt{1-(\cos\varphi_{12})^2}}{x + \frac{1}{x} + 2k\cos\varphi_{12}}, \quad (2\text{–}5)$$

where

$$k = \frac{M}{\sqrt{L_1 L_2}}, \quad (2\text{–}6)$$

$$x = \sqrt{\frac{L_1}{L_2}}\frac{I_1}{I_2}. \tag{2–7}$$

k denotes the coupling coefficient and is a useful measure for comparing magnetic properties of various coupler topologies; it is the fraction of magnetic flux produced by one coil and link to the opposite one [10].

To achieve maximum active to reactive power ratio, the following equation must be satisfied

$$\cos\varphi_{12} = -\frac{2k}{x+\frac{1}{x}}. \tag{2–8}$$

In tightly coupled coils, *k* is close to 1 and since I_2 is induced current by I_1, *x* will be close to 1 (if L_1=L_2). Therefore, cosφ_{12}≈-1 and therefore, φ_{12}≈180°. In the case of loosely coupled coils, *k* is close to 0 and therefore, φ_{12} is around 90° [41].

In the case of loosely coupled WPTs, where k<0.5, usually compensation network is added to both primary and secondary sides and designed to achieve maximum power transfer. Based on (2-3) to achieve this goal, φ_{12} must be equal to 90° and this is independent of *k* value. This means I_2 should lag I_1 by 90°. In this case, U_{12} will be in phase with I_2. Therefore, at the operating frequency, impedance seen from U_{12} will be pure resistive. To this end, secondary compensation network is designed to achieve φ_{12} close to 90° and therefore, reduce VA of the coils. Consequently, it will reduce the losses in the coils. On the other hand, primary compensation network is designed to cancel reactive power and consequently, reduce VA of the power electronics converter, hence their losses.

The output power of a WPT system is quantified by the short-circuit current (I_{sc}), the open-circuit voltage (V_{oc}) of the pickup coil and the quality factor, *Q*, as follows [11], [27]

$$P_{out} = P_{su}Q = V_{oc}I_{sc}Q = \omega M I_1 \frac{MI_1}{L_2}Q = V_{in}I_1k^2Q. \tag{2–9}$$

where, P_{su} is the product of V_{oc} and I_{sc} and represents the uncompensated power rating (without switch mode power supply). Also, V_{in} is voltage across L_1. As it can be seen from (2-9), output power can be reduced if coupling coefficient is reduced. Switched mode controller is used to boost power transfer by enabling compensation network to work at a load-dependent quality factor (Q) and to regulate DC output. For most applications, pad is chosen to provide desired P_{out} with Q of 1 when pads are ideally aligned. If a misalignment occurs, P_{out} is maintained by increasing the operational Q [11].

The transfer power control methods can be classified based on where control action is carried out. A general classification could be primary side control [7], [22], secondary side control [6], [8], and dual-side control [23]. In most cases with power being transferred from one primary pad to one receiver pad, primary and dual-side control are employed. For cases that primary pad transfers power to multiple receiver pads, secondary side control methods are used [41].

To achieve maximum power transfer capability to the load, the power supply is controlled to operate at a specific operating frequency and a primary current. To control the operating frequency, fixed- and variable-frequency control can be employed. Fixed-frequency controllers work with a predetermined frequency and consequently, are much simpler; however, in different operating conditions, such as change in load and coupling coefficient, required power rating (VA) of the power supply may increase. To minimize the power rating of the power supply, variable-frequency controllers operate at zero phase angle (ZPA) of input impedance seen from the power supply. By changing coupling coefficient and load impedance, more than one ZPA frequency can appear. This phenomenon is called bifurcation [13], [41]. If controller cannot cope with the bifurcation region, the operating frequency will move away from the desired frequency or set unstably to several

undesirable operating conditions. Under such a condition, power transfer capability will drop significantly [41].

3. LITERATURE REVIEW

Several positive features of wireless chargers compared with wired chargers, such as safe operation and convenience, have attracted attention of researchers in recent years. However, due to the structure and applications of WPTs, many new challenges that are not applicable for wired chargers, arise, some of which are listed below

- Variation of coupling coefficient due to coils' misalignment, air gap and couplers topology
- Power output dependency on coupling coefficient
- Power transfer efficiency dependency on coupling coefficient
- Power transfer efficiency dependency on load status
- Soft switching condition dependency on operating frequency, load status and coupling coefficient
- System efficiency dependency on load status
- Compensation network dependency on coupling coefficient and (or) load status
- Coupler topology impact on coupling coefficient and cost.

In the following subsections, major publications on the state of the art of WPT are reviewed. The papers are categorized into three main groups based on the topic they target: magnetic couplers, compensation networks, and power transfer efficiency.

3.1. Magnetic Couplers

The most common magnetic coupler for WPT chargers is circular coil. Figure 3.1 shows the components of a circular pad [11]. In this structure, Litz wire is used for coils to reduce skin and proximity losses in high frequencies. The ferrite tile or bars are employed under (above) primary (secondary) coil to limit magnetic field to one side of coils. Usually, aluminum shielding is added to the primary to prevent magnetic field from entering metal bars under the coupler and to avoid eddy current loss. This is used in the secondary side, as well to block the magnetic field from

leaking to the vehicle chassis (which causes losses) and also protect the passengers [47]. Plastic cover is employed to protect pad's components from damage and water penetration.

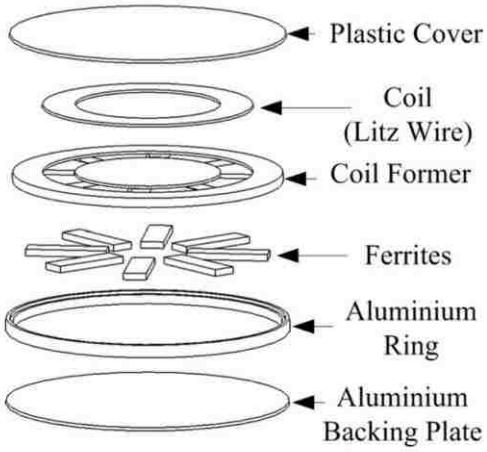

Figure 3.1 Components of a circular pad [11].

Coupling coefficient varies with position of coils with respect to each other. WPT is prone to misalignment and change of air-gap length. Typical air gap tolerance is up to 200-mm and horizontal misalignment tolerance from center to center should be greater than ± 200-mm [11]. As it is shown in (2-9), output power depends on coupling coefficient. On the other hand, as it will be discussed later, reduction in the coupling coefficient will result in reducing maximum transfer efficiency. Therefore, many efforts have been made to propose new topologies and analyze the parameters influencing the coupling coefficient. Due to field shaping produced based on ferrite structure in different topologies, mathematical analysis of coupling coefficient is complex. Therefore, majority of analyses are carried out with finite element analysis (FEA) software [11].

In [11], a comprehensive design for circular magnetic structure is proposed. Uncompensated power (P_{su}) variation in various structures of circular magnetic coupler is investigated. The effect of horizontal offset on P_{su} for specified vertical offset is shown. It is demonstrated that by increasing the horizontal and vertical offset, P_{su} is reduced. Also, at approximately 40% of pad

dimeter, there is a null in P_{su} profile. In addition, impact of other variables in pad structure, such as hole diameter of ferrite bars, angle of ferrite sector and ferrite arrangement, on P_{su} as well as pad volume are studied. Regarding ferrite size, simulation shows that length of ferrite has the highest effect on coupling coefficient and P_{su}, while ferrite thickness has the least influence. Furthermore, the leakage magnetic flux of charging system is simulated and measured. Finally, a magnetic coupler is designed that can meet human exposure regulations.

The design of a unipolar square coil is studied in [47]. Based on simulation results, larger size of the core pad than coil pad leads to higher coupling coefficient. However, the increase rate of coupling coefficient is insignificant if size of the core pad exceeds the coil pad. Also, simulation results demonstrate that by increasing the size of the aluminum shielding, the coupling coefficient is reduced. Thus, its size is fixed to be the same as the coil size. Another contribution of the paper is to design the coils to achieve maximum coupling coefficient for misaligned coils rather than for aligned coils.

In [27], two polarized coupler topologies, called double D (DD) and DDQ are proposed. The DD topology has highly desirable characteristics such as single-sided flux paths, insensitivity to aluminum shielding, an average flux path height that is proportional to half of the pad's length and a very low leakage magnetic flux out of its back [27].

Thickness and turn number of coils are investigated in [27]. It is revealed that narrow and closely spaced coils shorten the flux pipe, thus reducing the coupling coefficient for a given air gap. Conversely, if the coils are wound with an extremely large space, magnetic flux will leak out of the gaps between the turns and weaken the air-gap flux. Consequently, flux pipe will be shortened. If the coil has large number of turns, the length of the flux pipe will increase; however, the inductance of the coil will increase which in turn results in high voltage over the coils.

A serious problem of DD pad system is its weak performance along the x-axis. Simulation results show that when a horizontal offset in the x-axis reaches about 34% of the pad length, coupling coefficient becomes close to zero. In other words, at this misalignment level, flux enters and exits the same coil, and consequently, no voltage is induced at the secondary coil. To solve this problem, a quadrature coil is added to the receiver pad. The new configuration is called DDQ. This configuration solves the problem of null coupling coefficient to a considerable extend. The quadrature coil is tuned independent of the DD coil and added to the output of the DD coil after a rectification stage. Although DDQ shows a charge zone five times higher than that of a circular pad, it requires about two times more copper, however.

An alternative for DDQ is called bipolar pad [12]. It consists of two partially overlapped large D pads which are positioned such that no mutual inductance exists between them. This topology consumes 25% less power while it possesses similar performance to that of a DDQ pad. In [43], DD, DDQ and bipolar pads are compared. It is concluded that DDQ and bipolar pads can have good interoperation with a simple receiver pad. A drawback of DDQ and bipolar pads is that they need an additional power supply in the primary side.

In [44], variations in coupling coefficient, primary inductance, leakage fluxes, quality factors, and size have been studied for various combinations of circular, bipolar, and solenoid. It is demonstrated that non-polarized pads, such as circular and solenoid, have the lowest leakage and coupling coefficient. It is also shown that bipolar pad shows an acceptable leakage flux and is interoperable with solenoid, circular and polarized topologies.

In [39], a WPT system is optimized with respect to efficiency and power density. Losses in the HF inverter, transmitter and receiver coils, capacitors of compensation networks, and rectifier diodes are considered. In [42], it is demonstrated that mutual inductance variation with respect to

air gap can be minimized if radius of the transmitter and receiver coils are chosen to be different. Also, when radius of the transmitter is larger than the receiver, mutual inductance will be improved for long distances [42]. In [46], coupling coefficient variations with respect to air gap distance and misalignment are investigated. It is shown that if the inner diameter of the primary coils is larger than the outer diameter of the secondary coil, coupling coefficient is less sensitive to misalignment and gap distance variation, while for larger inner diameter of the primary, coupling coefficient is smaller than that of identical coils in a fully aligned situation.

To improve power transfer capacity and energy efficiency, intermediate coils (also referred to as repeater, relay resonator, domino resonator) are proposed [63]. Figure 3.2 depicts a four-coil structure. The power transfer can be improved by impedance matching and tuning the parameters of the intermediate coils [19], [29], [30]. It is worth noting that the physical parameters, such as self-inductance and coupling coefficient between the source and the load coils of a multi-coil system, is similar to that of a two-coil system. However, power transfer capability and efficiency improves through increasing apparent coupling coefficient [60], [31].

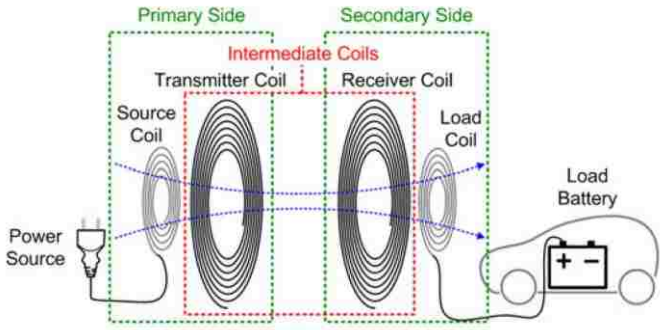

Figure 3.2 Four-coil resonator [60].

In [63], based on circuit theory, the two- and three-coil structures are compared. Based on a simplified model, the condition that a three-coil structure can achieve higher power transfer efficiency than its two-coil counterpart is obtained. The study is carried out for the case that all

coils are compensated with series capacitors. It is shown that the current stress and the electromagnetic field emission in the three-coil structure is less than the two-coil structure. Also, it is demonstrated that the difference observed in energy efficiency of the two- and three-coil structures is due to resistance of primary coil or internal resistance of the power source [57]. The study shows that the three-coil structure enhances the maximum energy efficiency provided that the transmitter and source coils are placed close enough.

In [60], an asymmetric four-coil system is proposed. The primary side consists of a source coil and two intermediate coils. In the secondary side, there is a single receiver coil. Compared to a symmetric four-coil structure, the proposed structure has higher efficiency because intermediate coils boost coupling coefficients two times around the operating frequency. It is shown that due to high coupling coefficient in the four-coil structure, the bifurcation phenomenon occurs, due to which three ZPA frequencies exist. This work proposes a method to work on an operating frequency that leads to constant output voltage characteristics.

3.2. Compensation Networks

In WPT applications, compensation networks are employed on both the primary and the secondary. The main purpose of using compensation network on the primary side is to minimize the VA of the switching power supply and its losses. Compensation network in the secondary side is designed to increase the short-circuit current of the secondary coil and thus, improve the power transfer capability [14].

Due to large air gap between the primary and the secondary, mutual inductance is low. Therefore, there is high magnetizing current. The situation gets worse when air gap increases or a misalignment occurs. Under this circumstance, leakage inductance is much larger than the mutual inductance. Thus, there is high circulating current and consequently loss in the coil. To reduce the

circulating current, hence the losses, the imaginary part of the input impedance must be decreased. This is achieved by employing a compensation network [35].

Four basic compensation networks, called series-series (SS), series-parallel (SP), parallel-series (PS) and parallel-parallel (PP), are shown in Figure 3.3. These networks are named based on the position of the capacitor with respect to the coils' inductances. A common method is to select secondary capacitor to resonate with the self-inductance of the secondary coil. The primary capacitance, though, is designed to compensate the primary coil self-inductance as well as the reflected imaginary impedance. Through this, the zero phase angle frequency of the impedance seen from the source is set equal to the secondary resonant frequency [41].

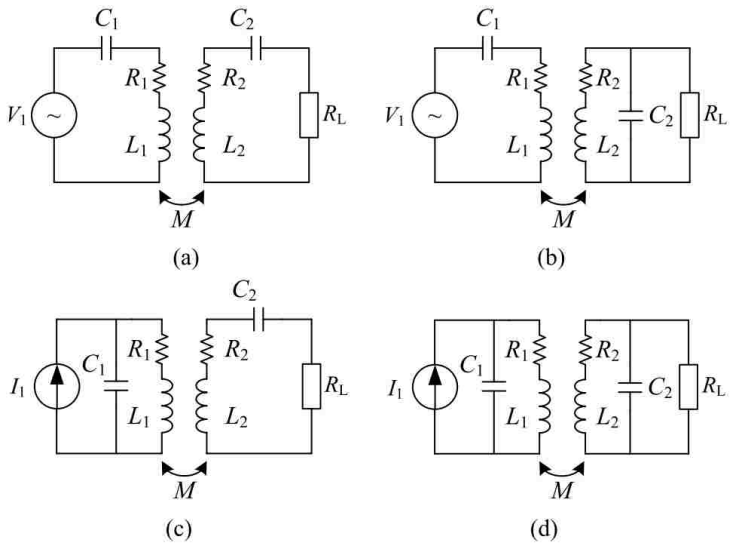

Figure 3.3 Four common compensation topologies (a) SS (b) SP (c) PS (d) PP [41].

Table 3.1 summarizes the reflected resistance and reactance when there is series and parallel compensation in the secondary. In this figure, Z_r denotes the reflected impedance from the secondary to the primary. As it can be observed, imaginary part of the reflected impedance for series-compensated secondary is zero, while a parallel-compensated secondary reflects a capacitive load. This is a major difference between series and parallel-compensated secondary [5].

Table 3.1. Reflected impedance for series and parallel-compensated secondary

Serious Secondary	$\mathrm{Re}(Z_r) = \frac{\omega_0^2 M^2}{R}$	$\mathrm{Im}(Z_r) = 0$
Parallel Secondary	$\mathrm{Re}(Z_r) = \frac{M^2 R}{L_2^2}$	$\mathrm{Im}(Z_r) = -\frac{\omega_0 M^2}{L_2}$

A common way for designing primary capacitance for four basic compensation networks are shown in Table 3.2. As it can be observed, for SS topology, the required primary compensation capacitance is independent of the mutual inductance and the load, while for SP topologies, capacitance depends on the mutual inductance. In addition, for parallel-compensated primary, the required primary compensation capacitance is a function of both the mutual inductance and the load. Therefore, the primary compensation capacitance for parallel-compensated primary must be designed for the required power [5].

Table 3.2. Conventional primary capacitor design for four basic compensation networks

SS	$C_1 = \frac{1}{\omega_0^2 L_1}$
SP	$C_1 = \frac{1}{\omega_0^2 (L_1 - M^2 / L_2)}$
PS	$C_1 = \frac{L_1 - M^2 / L_2}{(RM^2 / L_2^2)^2 + \omega_0^2 (L_1 - M^2 / L_2)^2}$
PP	$C_1 = \frac{L_1}{(\omega_0^2 M^2 / R)^2 + \omega_0^2 L_1^2}$

Impedance seen from power supply, Z_{in}, can be expressed as follows

$$Z_{in} = \begin{cases} \dfrac{1}{j\omega C_1} + j\omega L_1 + Z_r & \text{Series-compensated primary} \\ \dfrac{1}{j\omega C_1 + \dfrac{1}{j\omega L_1 + Z_r}} & \text{Parallel-compensated primary} \end{cases} \quad (3\text{–}1)$$

If design procedure in Table 3.2 is followed, imaginary part of the input impedance will be zero, and thus, reactive power flow will be eliminated. Generally, there are three ZPA frequencies in frequency spectrum of the input impedance. To have a unique ZPA frequency, which is equal to secondary resonant frequency, primary quality factor should be much higher than secondary quality factor. Primary and secondary quality factors are defined as follows [5]

$$Q_{p,s}(\omega = \omega_0) = \frac{\mathrm{VAR}_{p,s}}{P}, \quad (3\text{–}2)$$

where, VAR and P denotes reactive and transferred active power, respectively.

For compensation networks that their primary capacitance depends on coupling coefficient and/or load, changes in these variables can cause a phase shift in the impedance seen by the power supply. If the phase shift is considerable, higher VA rating must be considered for the power supply. To track ZPA under variation of coupling coefficient and/or load, variable frequency control method can be employed. However, as aforementioned, if the phase shift is significant, instability and uncontrollability may occur due to onset of bifurcation phenomenon [6].

Although operating at ZPA frequency leads to minimizing VA rating of the power supply, it is desirable that the impedance seen from the power supply to be partially inductive. In this way, the primary current will lag the inverter's output voltage, which will facilitate soft switching. With soft switching, the switches turn on while the voltage across them is zero thanks to early turn on of their body diode due to the residue current of the compensation network. This type of soft

switching is called zero voltage switching (ZVS). Under ZVS, switching loss is zero excluding the turn off switching loss of the active switch. By paralleling a capacitor (as lossless snubber) with an active switch, turn off loss can be reduced [36].

If the impedance seen from the inverter is capacitive, since the inverter current will lead the voltage, zero current switching (ZCS) can be achieved. In ZCS, turn off loss will be zero since the switch is turned off at the instant current crosses zero. This type of soft switching is not as much beneficial since all the other switching losses (turn on loss, diode recovery loss, etc) retain [36].

Myriad of studies have been conducted on the four basic compensation topologies. In [32], three ZPA frequencies of SS compensation network are analyzed. It is demonstrated that the circuit at two ZPA frequencies shows voltage follower characteristics, while at the third ZPA frequency at which compensation capacitor resonates with the self-inductance of the coils, it shows current follower characteristics. Because of high power transfer and efficiency, the operating frequency is usually set at third of the ZPA frequency. Figure 3.4 depicts voltage gain of SS versus frequency variations at different loads.

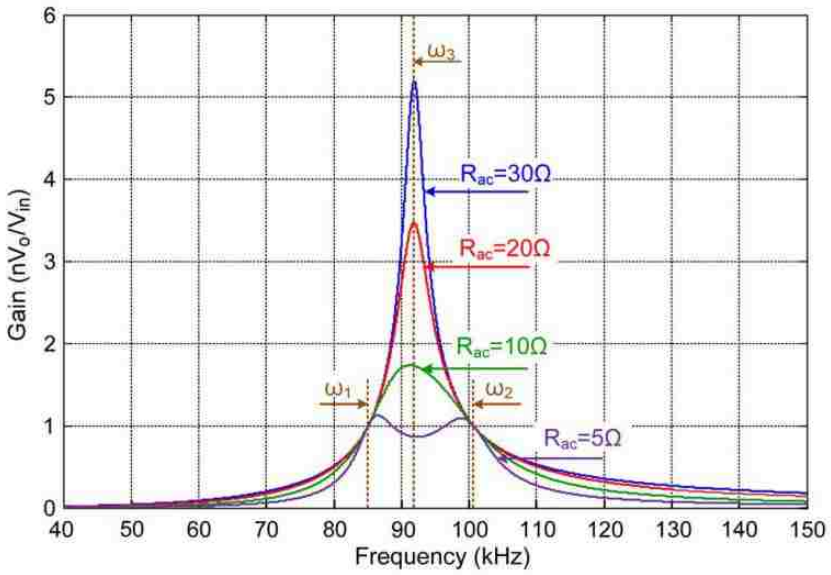

Figure 3.4 Voltage gain variation of a two-coil system with respect to frequency [32].

In [36], maximum efficiency and load-independent voltage transfer ratio operating frequencies for SS and SP compensation networks are investigated. It is shown that at two frequencies (voltage follower frequency), SS shows load-independent voltage transfer ratio, while SP shows similar characteristic only at one frequency. The operating frequency that maximum transfer efficiency is achieved for SS is derived and called ω_M. It is demonstrated that resonant frequency of SS is close to ω_M, while its voltage follower frequency (ω_H), which is higher than resonant frequency, is far from ω_M. Also, it is shown that operating at ω_H can lead to ZVS. However, in SS, both resonant frequency and ω_M do not possess voltage follower characteristics. On the other hand, for SP compensation, a design procedure can be followed so that maximum power transfer efficiency and voltage follower characteristics occur at the same frequency. For such an operating frequency, soft switching (ZVS) can be achieved automatically.

In [52], four basic compensation networks with voltage and current sources are compared in terms of five criteria: maximum efficiency, maximum load power transfer, load-independent output voltage and current, *k*-independent compensation and allowance of no magnetic coupling. It is found that current source SS is the only compensation that can meet all the five criteria. Also, current source SP compensation can meet the criteria except its weak *k*-dependency on the maximum efficiency.

In [66], it is demonstrated that in SS compensation, if resonance frequency of the transmitter coil is too close to the operating frequency, the buck converter in the receiver side cannot operate at high duty cycles; hence power transfer efficiency is reduced. A new frequency selection approach is proposed to avoid the region in which the relation between the received power and buck converter's duty cycle is inverse.

In [40], based on experimental results, it is shown that the efficiency of SS compensation is higher than SP compensation when the load value is small, i.e. during the constant-current stage and the beginning of the constant-voltage stage of the battery charging. On the contrary, the power transfer efficiency of the SP compensation is higher for larger values of load, i.e. during constant-voltage charging stage of the battery.

To address the aforementioned shortcomings, multiple modifications to the four basic compensation networks have been proposed [54], [59]. To achieve constant current and constant voltage characteristics, a dual topology is proposed in [26]. It uses semiconductor switches to switch between a series-compensated and parallel-compensated in the secondary side. In [9], a unity power factor WPT pick up is proposed that uses LCL network at the secondary. By minimizing the reactive current in the secondary coil and also decreasing the reflected reactive power on the power supply, efficiency is improved and cost is reduced. The proposed design compensates the effective inductive loading caused by the rectifier by adding a series capacitor.

In [20], four basic topologies are analyzed and compared based on their misalignment behavior. Combining the characteristics of SS and PS compensations, a new topology called SPS is proposed. The proposed topology is capable of transferring rated power with high efficiency in presence of up to 25 % misalignment without any additional control loops. In [28], a mixed-resonant coupling circuit, shown in Figure 3.5, is proposed.

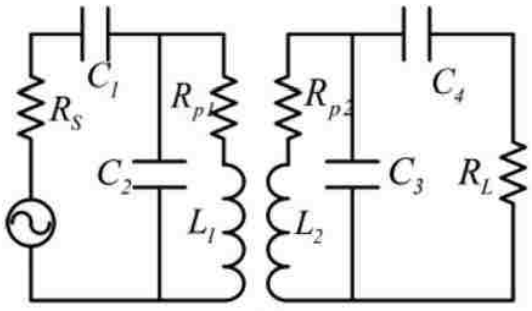

Figure 3.5 Mixed-resonant compensation for WPT [28]

It features higher transfer efficiency than SP since it inherits the low sensitivity characteristics of the SS compensation. The obtained results show that if the compensation capacitors are optimized, the mixed-resonant coupling circuit has stable transfer efficiency when load varies in a wide range.

In [51], two compensation structures, i.e. SP and another one with LCL at the primary side and a parallel capacitor in the secondary side, are compared. It is shown that SP is 2.45% cheaper than LCL compensation; however, LCL compensation can achieve higher peak efficiency at rated load. This is due to the fact that in LCL, the inverter only handles the current required to supply active power and overcome the loss in the resonant tank. Also, LCL shows better efficiency than SP in light loads. This occurs because in light loads, the input impedance of the LCL network becomes very high. As a result, the inverter output current becomes low, and thus, the conduction loss remains low. In addition, control complexity of SP is higher than LCL due to sensitivity of the reflected secondary impedance of SP to changes of load. The LCL topology uses partial series compensation in the primary and the secondary to boost the secondary coil current and reduce the VA rating of components of the resonant tank.

In [34], a compensation method is proposed that is suitable for application with one transmitter and multiple receivers. It is also suitable for dynamic WPTs where the receiver is highly dynamic. The proposed structure uses the reflected reactance of the receiver to strengthen the field in the coupled portions of the transmitter and the receiver and weaken it for uncoupled portions. In this way, power transfer can be carried out efficiently. Also, without complex shielding, electromagnetic field emissions standard are met.

In [14], an LCC primary compensation is proposed. The compensation components are designed by taking high order harmonics into account. The LCC structure features voltage follower characteristic and ZCS. Also, the input current is limited in absence of the receiver or in no load

condition. A doubled-sided LCC compensation network is proposed in [53]. The main features of the proposed compensation is that its resonant frequency is independent of the coupling coefficient and the load. Also, by tuning the compensation network, ZVS can be realized for the HF inverter.

In [59], a comprehensive review of compensation networks is presented. It is demonstrated that if a voltage source is used, the compensation network should have a T-circuit configuration in order to achieve a constant output voltage. Also, to achieve constant output current with an input current source, π-circuit configuration should be used. In [67], an LC/S compensation topology is introduced. The proposed method leads to constant output current. Compared with the double-sided LCC, the LC/S topology offers higher efficiency and lower cost due to less component count. In [62], an LCC compensation is proposed that is robust against wide coupling coefficient variations. The main goal is to achieve smooth power characteristics while coupling coefficient varies. This feature make the LCC compensation a promising candidate for dynamic WPTs.

3.3. Power Transfer Efficiency

Power transfer efficiency depends on several factors including load status, coupling coefficient, coils structure, operating frequency, and compensation network [65]. In [48], maximum power transfer and maximum energy efficiency loads are derived and is shown that they are different from each other. To achieve maximum power transfer, several closed loop methods have been reported, which can be classified into three main groups: dynamic impedance matching, frequency tracking, and using DC/DC converters. In the first group, the system operates at a fixed frequency and the impedance network is dynamically adjusted through relays and semiconductor switches to maximize power transfer frequency [24], [31]. In the second group, operating frequency is varied based on the output power feedback [25]. In the third group, maximum power transfer load is

adjusted by changing the duty cycles of a DC/DC converter [33]. Similar methods can be employed for following maximum power transfer efficiency load.

In [48], by using a switched mode controller in the receiver side, the optimal load value is emulated for maximum power transfer efficiency. The proposed method achieves maximum efficiency based on varying the input voltage to find an operating point at which the input power is minimized for a given output power. Since the search process is conducted in the transmitter side, no wireless communication feedback from the receiver side is required.

To follow maximum power transfer efficiency load, some methods use circuit models. Therefore, knowledge about the coupling coefficient value is necessary. To estimate the coupling coefficient value, several methods have been reported. References [37] and [58] propose a method for dynamically estimating the coupling coefficient based on the secondary coil parameters only. Also, [49] proposes a method for estimation of the coupling coefficient with recursive least squares (RLS) filter.

In [33], the output voltage is regulated by a boost converter in the receiver side, while a buck converter in the transmitter side searches for the maximum transfer efficiency by perturbing the operating point. Using an active single-phase rectifier with an auxiliary measurement coil, system maximum efficiency is tracked under load variation [64]. An inverter in the transmitter side is used to regulate the output voltage and an active rectifier regulates the desirable load impedance.

In [65], based on a dynamic coupling coefficient estimation, a method is proposed that takes the variation in coupling coefficient, load and output controllability into account. Two DC/DC converters are employed in the proposed WPT system. The duty cycle of the DC/DC converter in the secondary side is controlled to adjust the output load to the optimum value required for

maximum transfer efficiency. The DC/DC converter in the transmitter side regulates the output voltage.

4. FACTORS AFFECTING THE COUPLING COEFFICIENT VARIATION

In this section, the circular and square coils are compared in terms of achievable coupling coefficient and material usage. Figure 4.1 shows circular and square coils topology. Increasing the outer diameter of circular coils and also, external length in square coils leads to increase of the coupling coefficient [11]; however, in real world applications, due to physical and cost limitations, the outer diameter and external length of the coils are restricted. To this end, analysis are carried out to investigate the impact of coils structure on coupling coefficient for certain length and width. It is noteworthy to mention that the goal of this section is not to propose a coil design with highest coupling coefficient, but it is to show the trend of variation of the coupling coefficient with respect to physical construction of the coils. As studied in [11] and [47], thickness of Litz wires and ferrites has low impact on coupling coefficient. On the other hand, increasing the length of ferrite can enhance coupling coefficient.

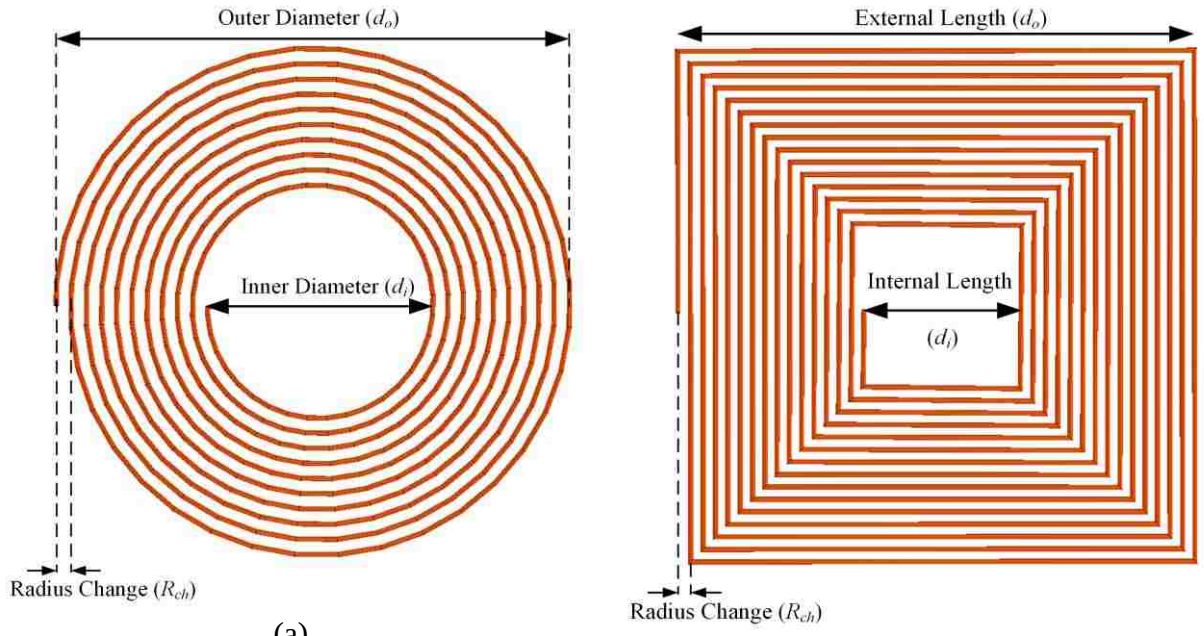

(a) (b)

Figure 4.1. Coils topology and dimensions (a) circular (b) square.

Therefore, to reach maximum achievable coupling coefficient, ferrite length is set equal to outer diameter and outer length of circular and square coils, respectively. Hence, the analysis are limited to variations in the inner diameter (length) and the turn space of coils.

All the tests are conducted in finite element analysis (FEA) software, ANSYS Maxwell. The simulation parameters match those of the prototype listed in Table 4.1. Figure 4.2 and Figure 4.3 depict exploded view of circular and square pads modeled in ANSYS Maxwell when ferrite tile and ferrite bars are employed, respectively.

Table 4.1. Ansys/Maxwell Simulation and Experimental Parameters

Parameter	Value
Ferrite Length/Width/Height (mm)	90/10/5
Ferrite Bars	32
Air Gap (mm)	150
Litz Wire	38 AWG×1000
AC Resistance per Meter (mΩ)	15
Outer Diameter (mm)	500

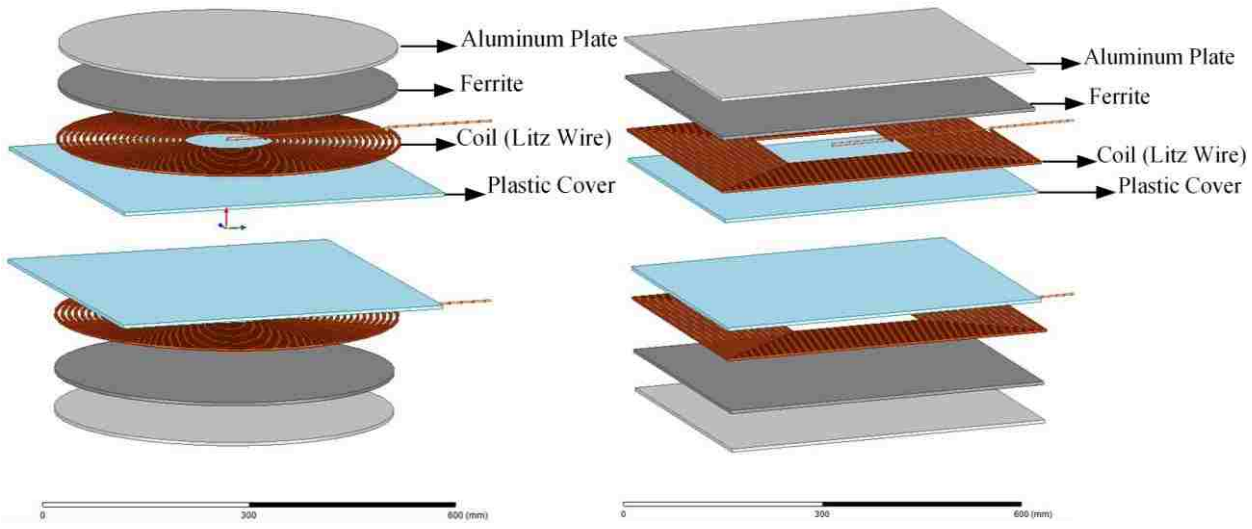

(a) (b)

Figure 4.2. Exploded view of (a) circular pad with ferrite tile (b) square pad with ferrite tile.

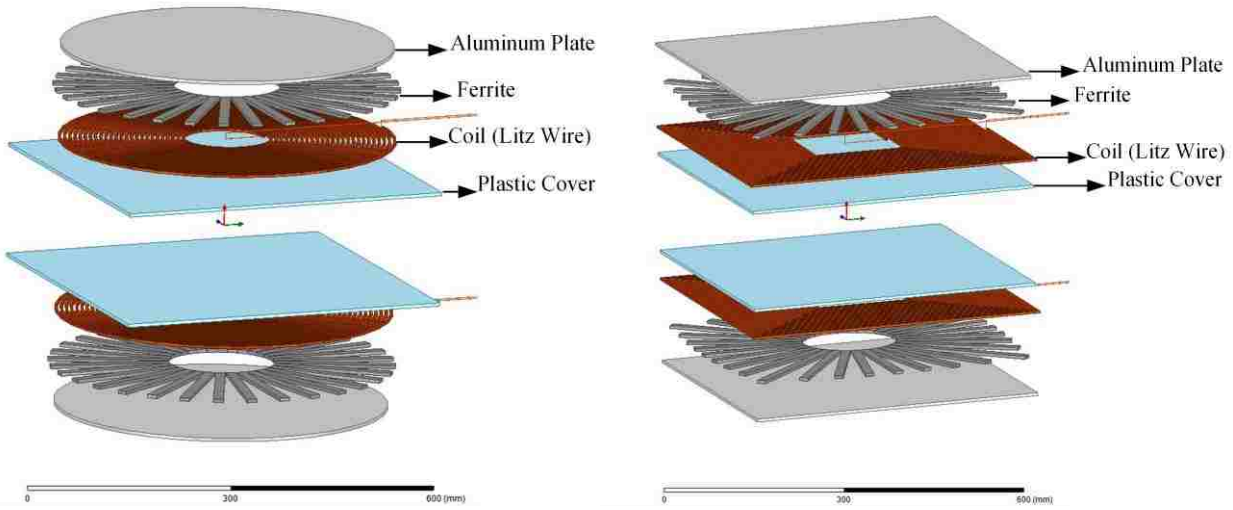

(a) (b)

Figure 4.3. Exploded view of (a) circular pad with ferrite bars (b) square pad with ferrite bars.

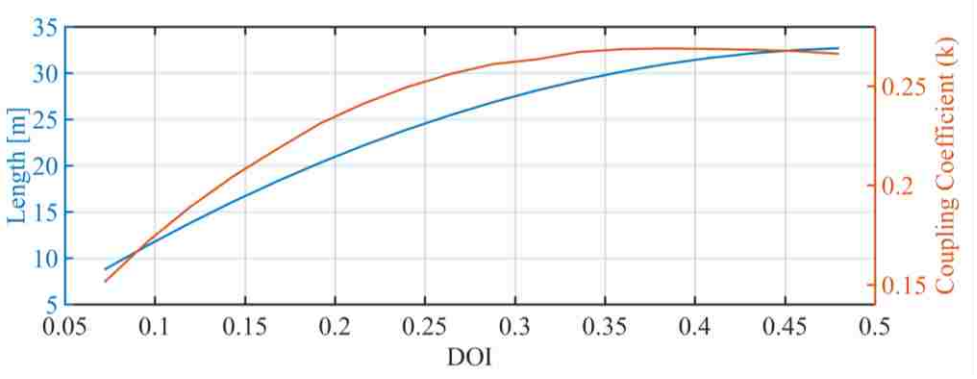

(a)

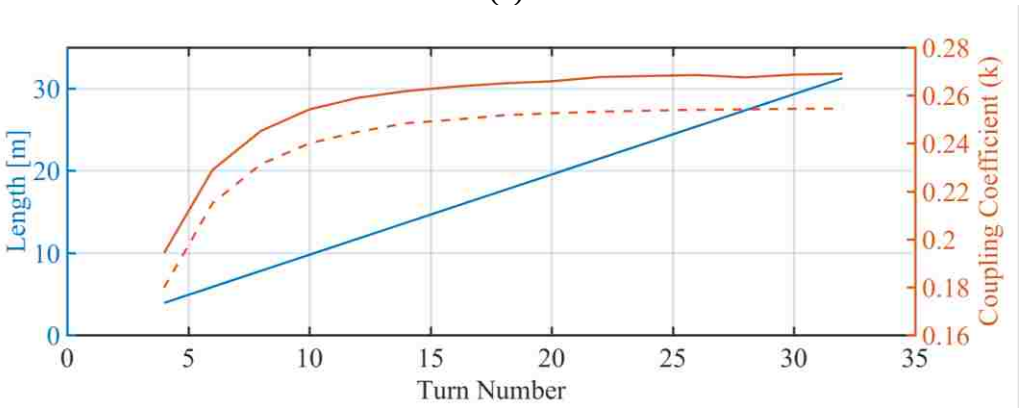

(b)

Figure 4.4. Coupling coefficient and coil wire length of circular coupler with ferrite tile (solid line) and ferrite bars (dashed line) (a) for variation of DOI and with no turn space (b) for variation of turn number and DOI=0.38 m.

In the first test, the impact of inner diameter (length) variations on the coupling coefficient as well as the length of Litz wire is evaluated. The turn space is considered almost zero. The obtained results are shown in Figure 4.4. (a) and Figure 4.5 (a) for circular and square pads, respectively, when ferrite tile is used as pad's core. As it can be seen, by increasing the difference between the outer and inner diameters (DOI) of circular pad and the difference between the outer and inner length (LOI) of square pad, the coupling coefficient and the wire length are increased.

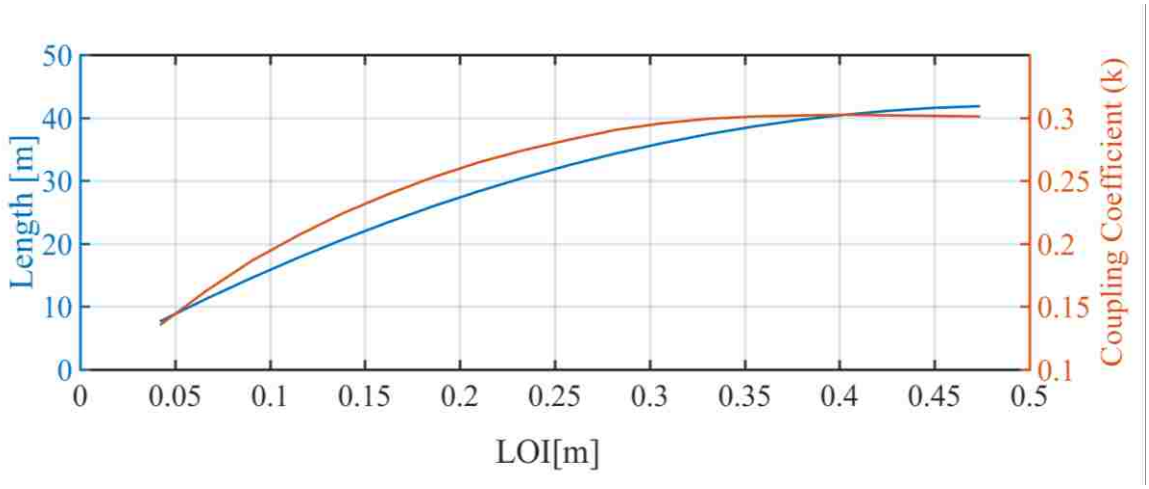

(a)

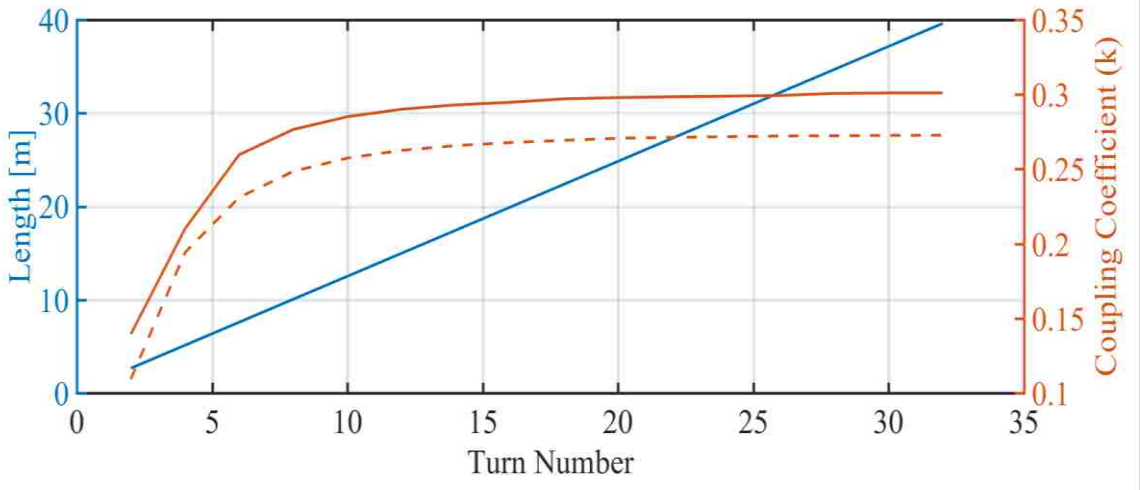

(b)

Figure 4.5. Coupling coefficient and coil wire length of square coupler with ferrite tile (solid line) and ferrite bars (dashed line) (a) for variation of LOI and with no turn space (b) for variation of turn number and LOI=0.35 m.

Based on Figure 4.4. (a), for DOI more than 0.38 m, the coupling coefficient is almost constant, while the wire length increases. Also, for square pad, coupling coefficient increase for LOI more than 0.35 is insignificant. Figure 4.4. (b) shows the variation of the coupling coefficient and wire length versus the turns number for a circular pad when the outer and inner diameters are considered constant (DOI=0.38m). In this figure, dashed line illustrates coupling coefficient of circular pad when ferrite bars are used as core and the turn space or the turns number is varied.

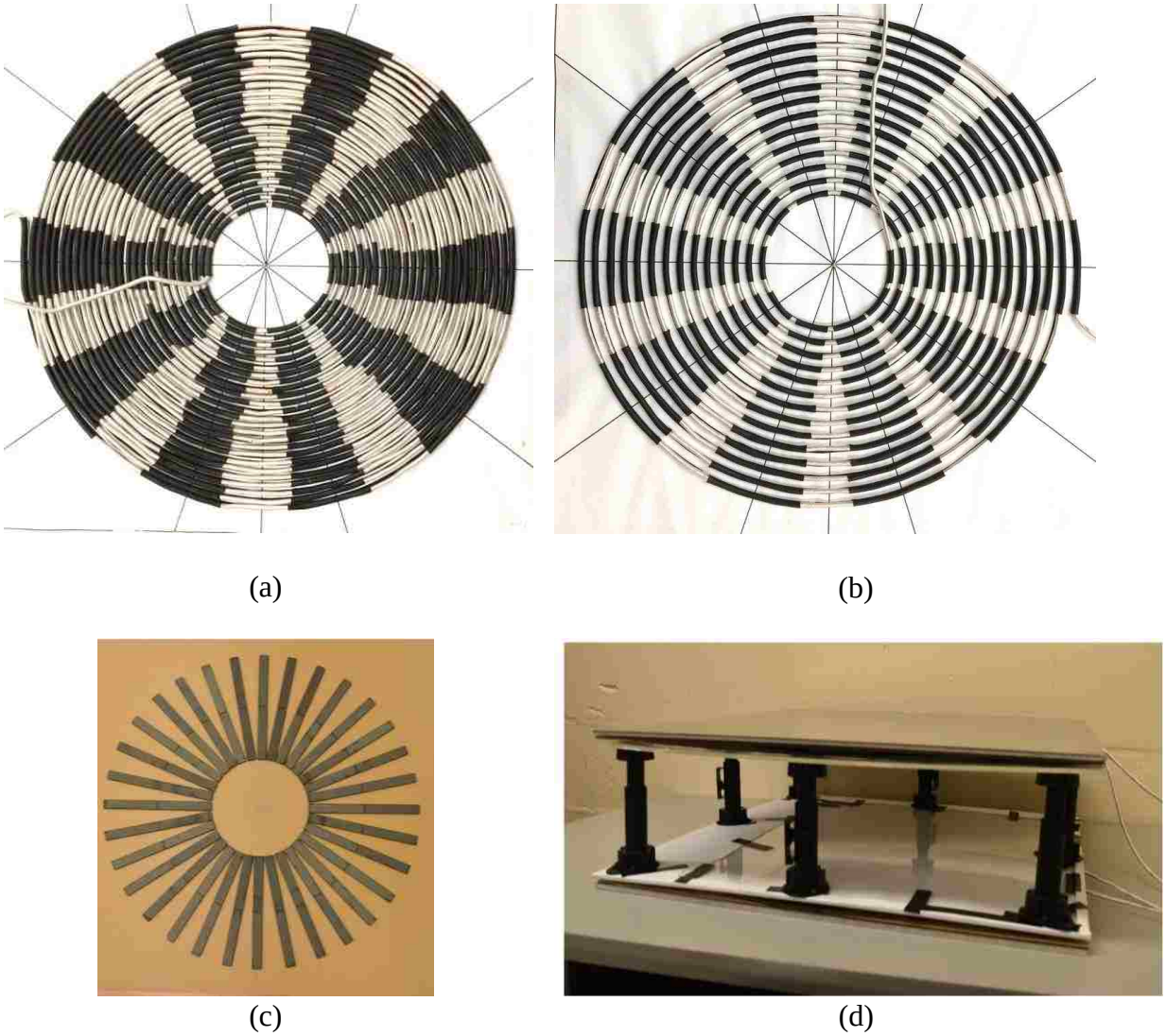

(a) (b)

(c) (d)

Figure 4.6. Coil with (a) 25 turns (b) 14 turns (c) ferrite plane (d) experimental WPT setup.

As it can be observed, coupling coefficients for pads with discrete ferrites is lower than the same quantity for pads with ferrite tile; however, the difference is insignificant and cost and weight reduction of pad justify it. Figure 4.5 (b) shows the obtained results for similar test when square pad is used. Based on the obtained results for two pads, it can be noticed that the changes in the coupling coefficient are insignificant for a wide range of turns number. This feature is used in the next section to improve the TE of WPT.

Figure 4.6 depicts the structure of a WPT prototype constructed in the lab with Litz wire circular coil, ferrite bars and aluminum shielding

.

5. PROPOSED COMPENSATION TOPOLOGIES

5.1. WPT System Structure

Various WPT system structures are proposed in the literature. The structure presented in [14] is employed in this work as it satisfies the requirements of the utility and the battery. In addition, it improves the compactness of the system. Two different WPT systems, shown in Figure 5.1, are employed for this work. The first system is used when the input voltage is DC (see Figure 5.1 (a)) and the second one is used when the input voltage is AC (see Figure 5.1 (b)). As it can be observed in Figure 5.1, a DC-DC converter is connected after the DC power supply and a single phase PFC is connected to the AC voltage. Its goal is to control the input DC voltage of the HF inverter and also in the case of the PFC, to provide a sinusoidal input current in phase with the input voltage. Voltage fed full-bridge inverter is used to produce an HF square wave with desired operating frequency from the input DC voltage.

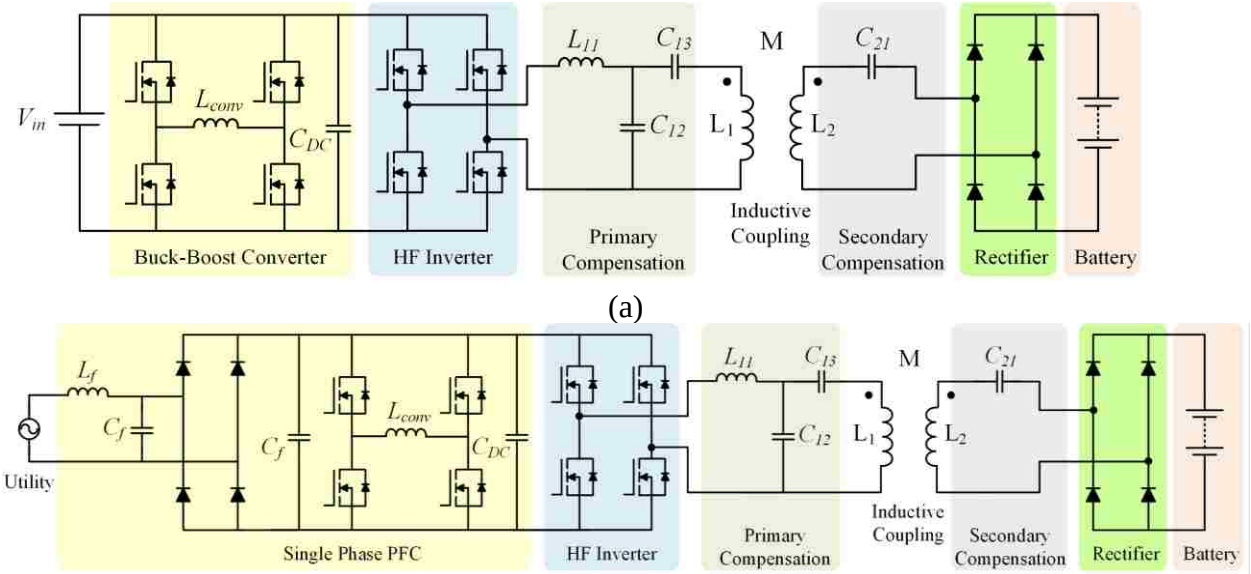

Figure 5.1. Architecture of the employed WPT system with (a) DC power supply, (b) AC grid.

To minimize the VA rating of the primary side converters as well as switching losses in the HF inverter, primary compensation network is used. Secondary compensation network is also employed to increase the power transfer capability. To reduce the control complexity of the converters and restricting the voltage rating of the WPT system components, compensation network with load-independent VTR capability is used. In the secondary side, to convert HF AC voltage to DC, a full-bridge rectifier is used. Active rectifier can be another alternative if the reflected load to the primary needs to be controlled. The load is a battery and is charged with constant voltage and constant current methods.

5.2. Constant Voltage Compensation Networks

Two compensation topologies are proposed and based on their derived efficiency equations, primary and secondary coils are designed (in the next section). Figure 5.2 depicts the structure of the two compensation networks.

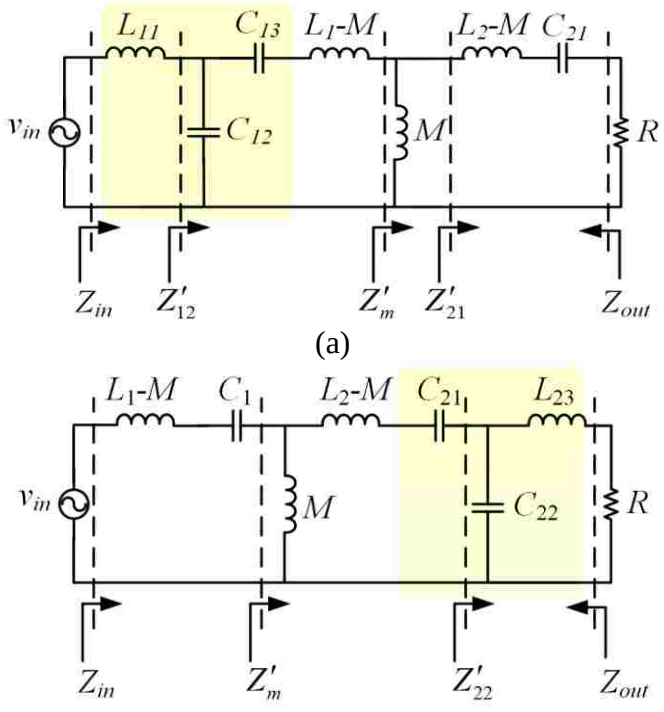

Figure 5.2. Equivalent circuit of WPT system with (a) primary LCC compensation, and (b) secondary LCC compensation.

Both topologies are designed to feature constant output voltage, i.e., load-independent VTR, which is of paramount importance in WPT systems.

5.3. Primary LCC Compensation (PLCC)

In this compensation network, LCC is adopted in the primary side and a capacitor is connected in series with the coil at the secondary side. Figure 5.2 (a) shows the configuration of this network. Based on SAE standard recommendation, operating frequency is set at 85 kHz [41]. Therefore, operating frequency is assumed to be known. To achieve load independent output voltage characteristic, the impedance seen from the load side (Z_{out}) must be equal to zero. To this end and by assuming that L_1 and L_2 are known, the passive components must be selected such that the following criteria is satisfied

$$C_{21} = \frac{1}{\omega_0^2 L_2}, \tag{5–1}$$

$$C_{12} = \frac{1}{\omega_0^2 L_{11}}, \tag{5–2}$$

Here, ω_0 denotes operating angular frequency. Based on (5-1) and (5-2), the load independent voltage transfer ratio (VTR) can be obtained. Also, by wise selection of C_{13}, zero voltage switching (ZVS) can be achieved. In the following section, based on equivalent circuit of the system and mathematical analysis, these important features of PLCC compensation network will be demonstrated.

5.3.1. Zero Voltage Switching of PLCC

Based on equivalent circuit of WPT system with PLCC compensation network (see Figure 5.2 (a)) the impedance seen from the input voltage source can be obtained as follows

$$Z'_{21} = j\omega_0(L_2 - M) + \frac{1}{jC_{21}\omega_0} + R, \tag{5–3}$$

$$Z'_m = \frac{jM\omega_0 \times Z'_{21}}{jM\omega_0 + Z'_{21}}, \tag{5–4}$$

$$Z'_{13} = \frac{1}{jC_{13}\omega_0} + j(L_1 - M)\omega_0 + Z'_m, \tag{5–5}$$

$$Z'_{12} = \frac{Z'_{13}\dfrac{1}{jC_{12}\omega_0}}{Z'_{13} + \dfrac{1}{jC_{12}\omega_0}}, \tag{5–6}$$

$$Z_{in} = jL_{11}\omega_0 + Z'_{12} = jL_{11}\omega_0 + \frac{\dfrac{1}{jC_{12}\omega_0} \times \dfrac{1}{jC_{13}\omega_0} + \dfrac{L_1}{C_{12}} + \dfrac{\omega_0^2 M^2}{R}\dfrac{1}{jC_{12}\omega_0}}{\dfrac{1}{jC_{12}\omega_0} + \dfrac{1}{jC_{13}\omega_0} + jL_1\omega_0 + \dfrac{\omega_0^2 M^2}{R}}. \tag{5–7}$$

Therefore, Z_{in} can be expressed as

$$Z_{in} = \frac{\dfrac{-1}{C_{12}C_{13}\omega_0^2} + \dfrac{L_1}{C_{12}} + \dfrac{\omega_0^2 M^2}{R}\dfrac{1}{jC_{12}\omega_0} + \dfrac{L_{11}}{C_{12}} + \dfrac{L_{11}}{C_{13}} - \omega_0^2 L_{11}L_1 + \dfrac{jL_{11}\omega_0^3 M^2}{R}}{\dfrac{1}{jC_{12}\omega_0} + \dfrac{1}{jC_{13}\omega_0} + jL_1\omega_0 + \dfrac{\omega_0^2 M^2}{R}}. \tag{5–8}$$

If $\omega_0 = \dfrac{1}{\sqrt{L_2 C_{21}}} = \dfrac{1}{\sqrt{L_{11}C_{12}}}$, the following expressions can be written

$$\frac{-1}{C_{12}C_{13}\omega_0^2} + \frac{L_{11}}{C_{13}} = 0, \tag{5–9}$$

$$\frac{L_1}{C_{12}} - \omega_0^2 L_{11}L_1 = 0, \tag{5–10}$$

$$\frac{\omega_0^2 M^2}{R}\frac{1}{jC_{12}\omega_0} + \frac{jL_{11}\omega_0^3 M^2}{R} = 0. \tag{5–11}$$

Hence, Z_{in} can be simplified to

$$Z_{in} = \frac{\frac{L_{11}}{C_{12}}}{\frac{1}{jC_{12}\omega_0} + \frac{1}{jC_{13}\omega_0} + j\omega_0 L_1 + \frac{\omega_0^2 M^2}{R}}. \tag{5–12}$$

To achieve zero phase angle (ZPA), *Img* (Z_{in})=0. To this end, the following expression must be satisfied

$$\frac{1}{jC_{12}\omega_0} + \frac{1}{jC_{13}\omega_0} + j\omega_0 L_1 = 0 \Rightarrow C_{13} = \frac{1}{\omega_0^2 (L_1 - L_{11})}. \tag{5–13}$$

However, to eliminate turn-on loss of inverter's switches, zero voltage switching (ZVS) is interested. To achieve ZVS, the impedance seen from inverter should be inductive, and equivalently, *Img* (Z_{in})>0. To this end, without violating load independent VTR of the system, C_{13} can be redefined as

$$C_{13} = \frac{1}{\beta\omega_0^2 (L_1 - L_{11})}. \tag{5–14}$$

Therefore, after substituting C_{13} defined in (5-14) into (5-12), Z_{in} can be expressed as

$$Z_{in} = \frac{L_{11}\omega_0^2}{\frac{(1-\beta)}{jC_{12}\omega_0} + jL_1(1-\beta)\omega_0 + \frac{\omega_0^2 M^2}{R}}. \tag{5–15}$$

After some simplifications and using coupling coefficient instead of mutual inductance, Z_{in} can be rewritten as

$$Z_{in} = \frac{RL_{11}^2 \omega_0^2 k^2 L_1 L_2}{\omega_0^2 (k^2 L_1 L_2)^2 + R^2 (1-\beta)(L_1 - L_{11})^2} + \frac{j\omega_0 R^2 L_{11}^2 (1-\beta)(L_{11} - L_1)}{\omega_0^2 (k^2 L_1 L_2)^2 + R^2 (1-\beta)(L_1 - L_{11})^2}. \tag{5–16}$$

Now, the angle of Z_{in} can be calculated as follows

$$\angle Z_{in} = arc\tan\left(\frac{R(1-\beta)(L_{11} - L_1)}{\omega_0 k^2 L_1 L_2}\right). \tag{5–17}$$

As it can be seen, the angle of Z_{in} is independent of mutual inductance of the system. From the above equation, it can be seen that if β=1, φ will be zero and ZPA can be obtained. Also, Z_{in} will be as follows

$$Z_{in} = \frac{RL_{11}^2}{M^2}. \qquad (5\text{–}18)$$

This equation shows that in case of misalignment or absence of a receiving coil (where M becomes close to zero), Z_{in} assumes a large value. In addition, if load is disconnected for any reason, its equivalent value goes high and therefore, again, Z_{in} becomes a large value. Hence, the input current is automatically reduced, which is a positive feature for a WPT system and can reduce control effort. In addition, as it can be seen from (5-18), L_{11} can be selected to modify Z_{in}. High values of L_{11} can limit the input current and therefore, efficiency of the prior stages can be improved; however, the equivalent series resistance (ESR) of L_{11} as well as core loss in L_{11} should be taken into account. Figure 5.3 shows bode plot of Z_{in} for parameters listed in Table 5.1 and when β is set at 1. In this figure, frequency response of Z_{in} is plotted for a wide range of load (R=7, 23, 46, 67 and 200 Ω). As it can be observed, magnitude of Z_{in} at operating frequency and for different values of load follows equation (5-18) and increases proportional with R. Furthermore, phase of Z_{in} at operating frequency is equal to zero regardless of load values, which shows ZPA operation.

Based on (5-17), if L_{11}>L_1, by choosing β<1 and if L_{11}<L_1, by choosing β>1, ZVS can be achieved.

shows the frequency response of Z_{in} when value of β is intentionally selected bigger than one to achieve ZVS operation for inverter. As it can be seen from the figure, although magnitude of Z_{in} at operating frequency is similar to the corresponding value for ZPA operation, phase of Z_{in} is

positive for all values of load, which means impedance seen from inverter is inductive and ZVS operation is feasible.

Table 5.1. Parameters of WPT system with PLCC compensation used for Z_{in} frequency analysis.

Parameter [unit]	Value
$f_{sw\text{-}inv}$ [kHz]	80
k [-]	0.22
R [Ω]	7, 23, 46, 67 and 200
L_1 [µH]	253
L_2 [µH]	249
L_{11} [µH]	76.5
C_{12} [nF]	51.7
C_{13} [nF]	22.4, 21.7
C_{21} [nF]	15.9

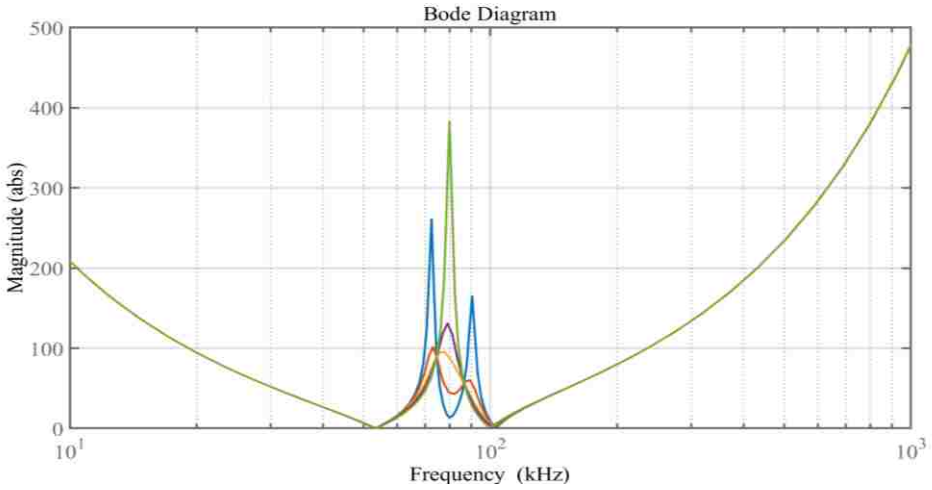

(a)

Figure 5.3. Frequency response of Z_{in} for PLCC and when β is 1 (C_{13}=22.4 nF). (a) magnitude, (b) magnitude zoomed, (c) phase, (d) phase zoomed. 7 Ω (blue), 23 Ω (red), 46 Ω (yellow), 67 Ω (purple) and 200 Ω (green) load.

(Figure 5.3 continued)

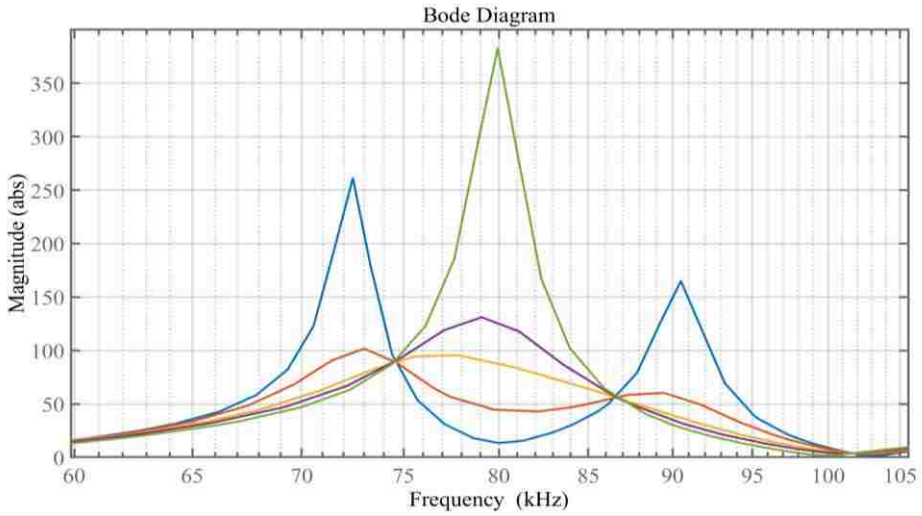

(b)

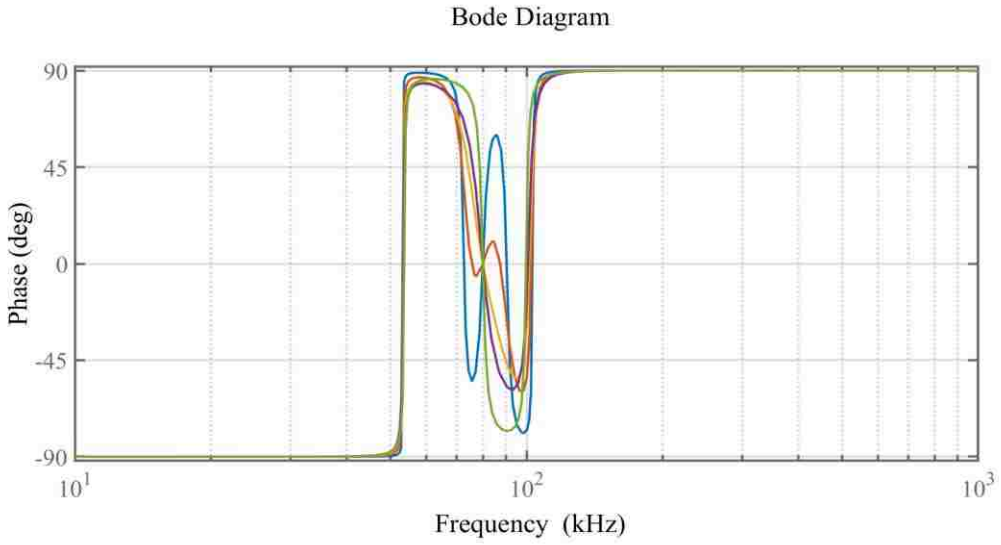

(c)

(Figure 5.3 continued)

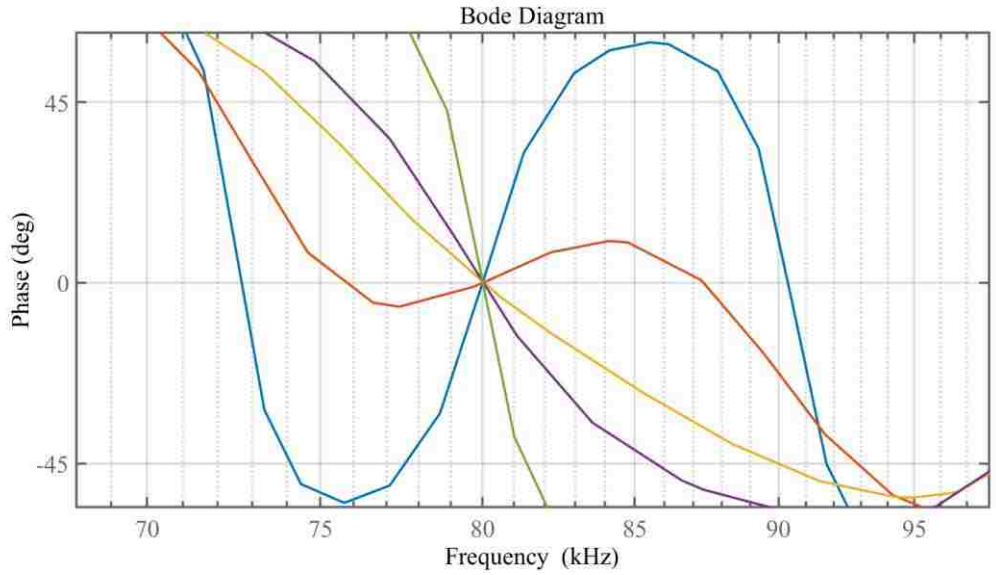

(d)

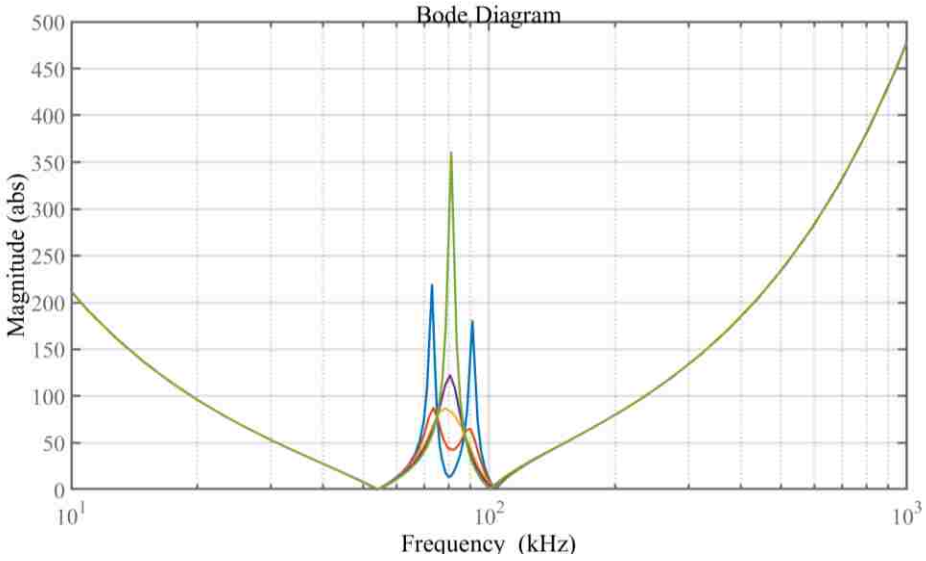

(a)

Figure 5.4. Frequency response of Z_{in} for PLCC and when β is higher than 1 (C_{13}=21.7 nF). (a) magnitude, (b) magnitude zoomed, (c) phase, (d) phase zoomed. 7 Ω (blue), 23 Ω (red), 46 Ω (yellow), 67 Ω (purple) and 200 Ω (green) load.

(Figure 5.4 continued)

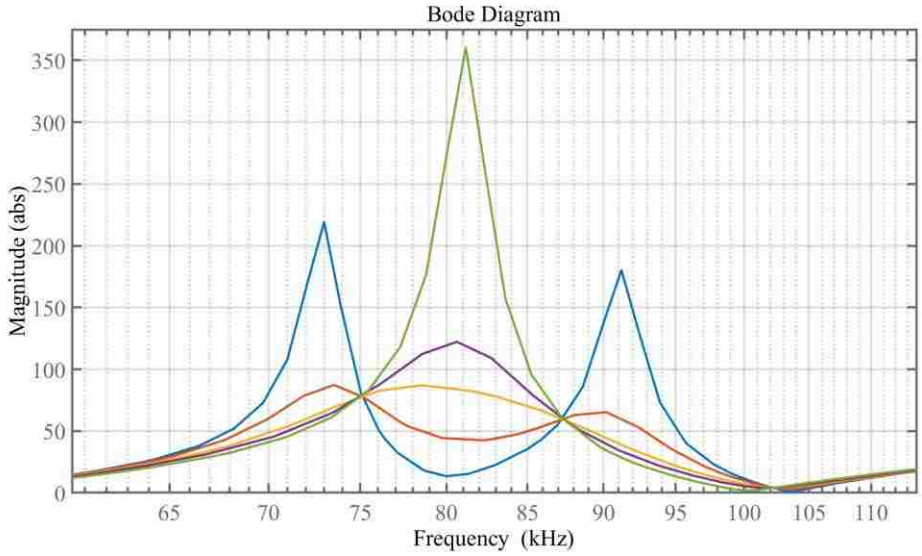

(b)

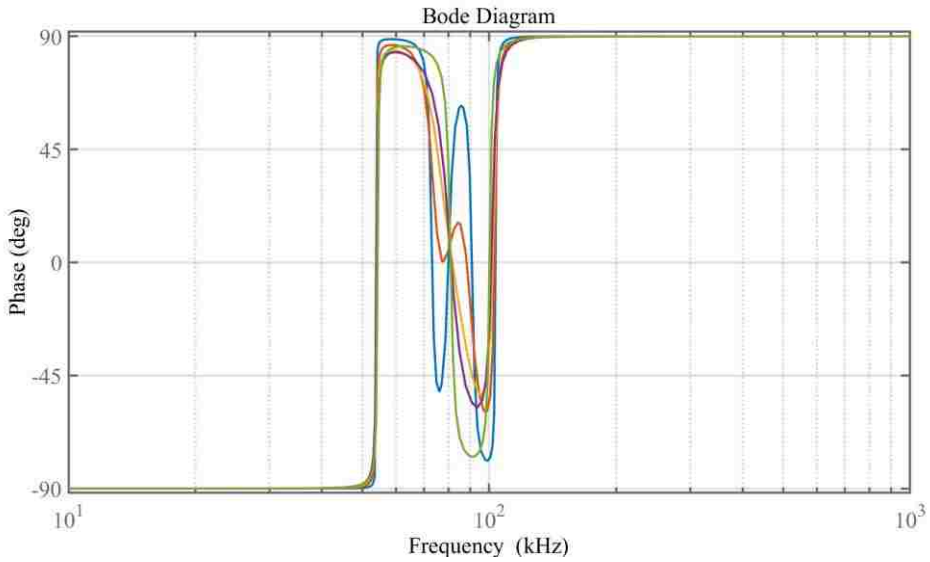

(c)

(Figure 5.4 continued)

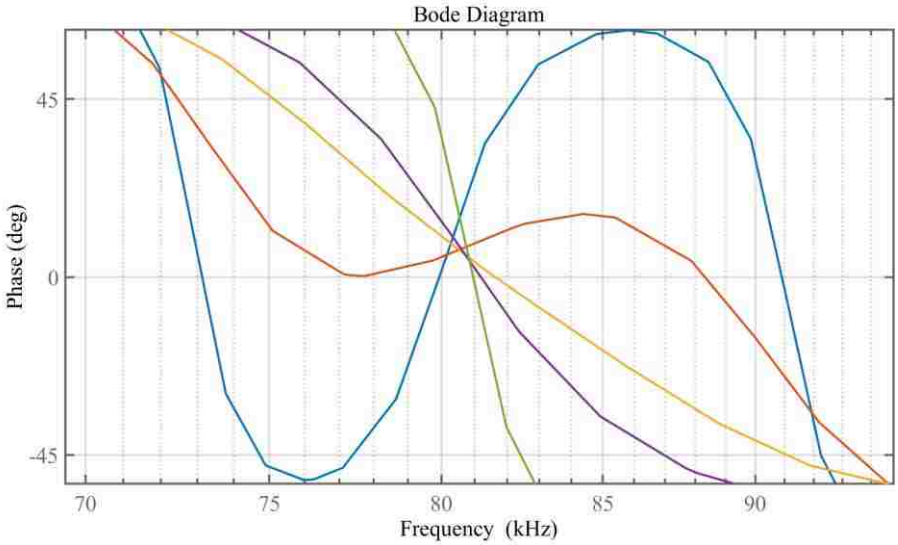

(d)

5.3.2. Load-Independent Voltage Transfer Ratio

Based on Figure 5.2 (a), VTR of WPT for primary LCC compensation can be obtained as follows

$$VTR = \frac{V_{out}}{V_{in}} = \frac{R}{Z'_{21}} \times \frac{Z'_m}{Z'_{13}} \times \frac{Z'_{12}}{Z'_{in}}. \tag{5–19}$$

Based on (5-1) and (5-2), Laplace transform of Z_{in} can be written as follows

$$Z'_{21}(s) = s(L_2 - M) + \frac{\omega_0^2 L_2}{s} + R, \tag{5–20}$$

$$Z'_m(s) = \frac{Ms \times Z'_{21}}{Ms + Z'_{21}}, \tag{5–21}$$

$$Z'_{13}(s) = \frac{\beta\omega_0^2(L_1 - L_{11})}{s} + s(L_1 - M) + Z'_m, \tag{5–22}$$

$$Z'_{12}(s) = \frac{Z'_{13} \times \frac{\omega_0^2 L_{11}}{s}}{Z'_{13} + \frac{\omega_0^2 L_{11}}{s}}, \tag{5–23}$$

$$Z_{in}(s) = sL_{11} + Z'_{12}, \tag{5–24}$$

Using (5-20) to (5-24), VTR can be simplified as follows

$$VTR = \frac{Ms^3\omega_0^2 R}{R \times DEN_1 + DEN_0}, \tag{5–25}$$

where,

$$DEN_1 = (L_1 s^5 + s^3\omega_0^2((1+\beta)L_1 + (1-\beta)L_{11}) + \beta s\omega_0^4(L_1 - L_{11})), \tag{5–26}$$

$$DEN_0 = (s^2 + \omega_0^2)((L_1L_2 - M^2)s^4 + \beta L_2\omega_0^4(L_1 - L_{11}) + L_2 s^2\omega_0^2(L_1(1+\beta) + L_{11}(1-\beta))), \tag{5–27}$$

To find frequencies with load-independent VTR characteristics, the derivative of VTR with respect to load is calculated and set equal to zero

$$\frac{\partial VTR}{\partial R} = 0. \tag{5–28}$$

After some simplification, the following equality can be derived

$$Ms^3\omega_0^2(s^2 + \omega_0^2)((L_1L_2 - M^2)s^4 + L_2\omega_0^2(L_1(1+\beta) + L_{11}(1-\beta))s^2 + \beta L_2\omega_0^4(L_1 - L_{11})) = 0, \tag{5–29}$$

The roots of above equation are as follows

$$\begin{aligned}
s_{1,2,3} &= 0 \\
s_{4,5} &= \pm j\omega_0 \\
s_{6,7} &= \pm j\sqrt{\frac{-\sqrt{L_2^2\omega_0^4(L_1(1+\beta) + L_{11}(1-\beta))^2 + \beta L_2\omega_0^4(L_1 - L_{11})(4M^2 - 4L_1L_2)} - L_2\omega_0^2(L_1(1+\beta) + L_{11}(1-\beta))}{2M^2 - 2L_1L_2}} \\
s_{8,9} &= \pm j\sqrt{\frac{\sqrt{L_2^2\omega_0^4(L_1(1+\beta) + L_{11}(1-\beta))^2 + \beta L_2\omega_0^4(L_1 - L_{11})(4M^2 - 4L_1L_2)} + L_2\omega_0^2(L_1(1+\beta) + L_{11}(1-\beta))}{2M^2 - 2L_1L_2}}
\end{aligned} \tag{5–30}$$

Substituting (5-30) into (5-25), load-independent VTRs can be derived as follows

$$VTR(s_{4,5}) = \frac{M}{L_{11}}. \tag{5–31}$$

$$VTR(s_{6,7}) = \frac{-(M^2 - L_1L_2)\sqrt{L_2}}{M(\sqrt{M^2(L_1 - L_{11}) + L_1L_2L_{11}} - \sqrt{L_2}L_1)} = \frac{-\sqrt{L_2}(k^2 - 1)}{k(\sqrt{k^2(L_1 - L_{11}) + L_{11}} - \sqrt{L_1})}. \quad (5\text{–}32)$$

$$VTR(s_{8,9}) = \frac{(M^2 - L_1L_2)\sqrt{L_2}}{M(\sqrt{M^2(L_1 - L_{11}) + L_1L_2L_{11}} + \sqrt{L_2}L_1)} = \frac{\sqrt{L_2}(k^2 - 1)}{k(\sqrt{k^2(L_1 - L_{11}) + L_{11}} + \sqrt{L_1})}. \quad (5\text{–}33)$$

From (5-31)-(5-33), it can be concluded that VTR at operating frequency only depends on M and L_{11}. If the mutual inductance in the aligned situation is known, L_{11} can be adjusted to achieve the desired VTR. When a misalignment occurs or distance of primary and secondary pads change, mutual inductance of two pads will change correspondingly. Under these conditions, a DC/DC converter or a PFC can be used to regulate the output voltage and compensate VTR variation between the inverter's output and the rectifier's input. Figure 5.5 shows frequency response of VTR for a WPT system with PLCC compensation network.

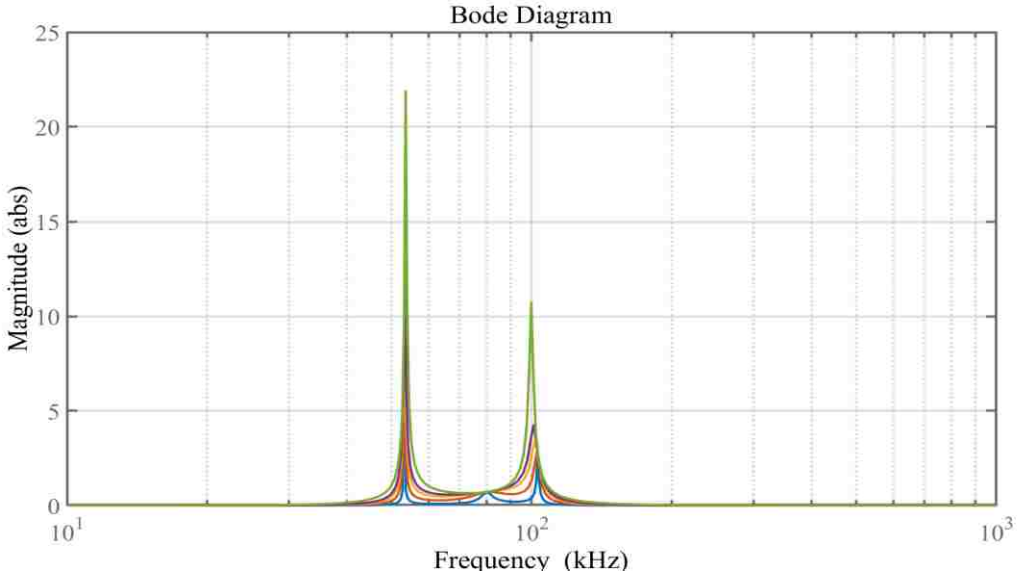

(a)

Figure 5.5. Frequency response of VTR of PLCC (C_{13}=22.4 nF). (a) magnitude, (b) magnitude zoomed, (c) phase. 7 Ω (blue), 23 Ω (red), 46 Ω (yellow), 67 Ω (purple) and 200 Ω (green) load.

(Figure 5.5 continued)

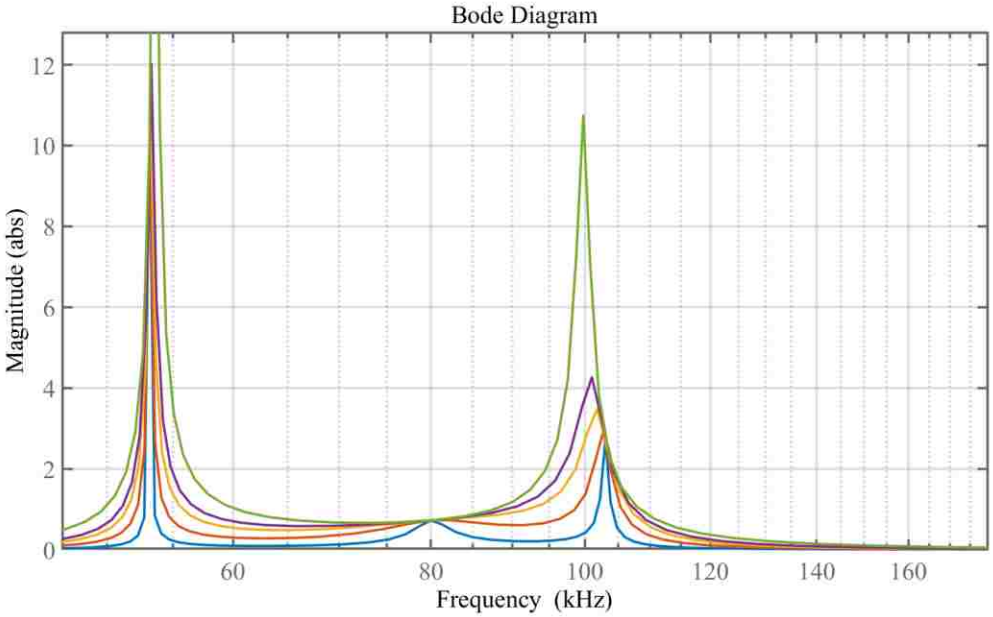

(b)

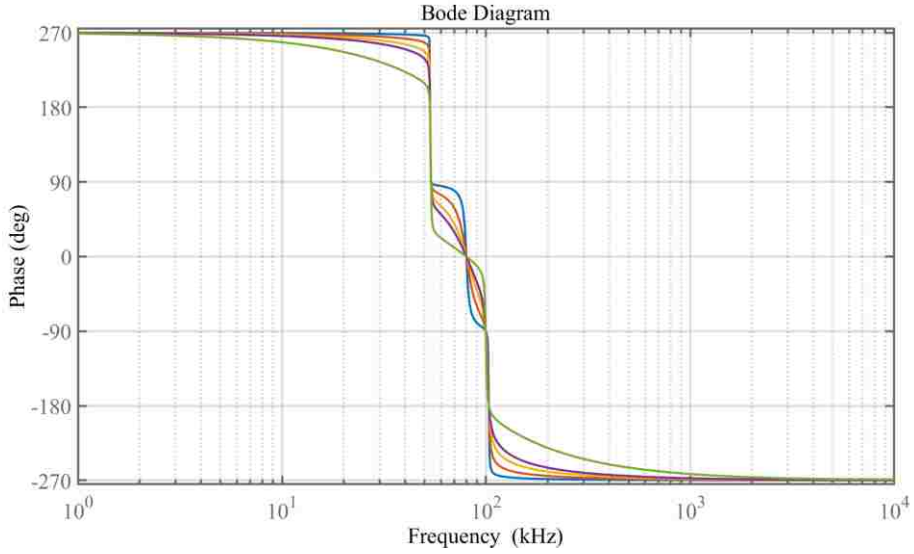

(c)

Parameters listed in Table 5.1 are used for this analysis. The load-independent frequencies of this system can be obtained using (5-30). These frequencies are listed in Table 5.2. Having examined magnitude and phase of VTR for different loads in Figure 5.5, one can observe that the load-independent frequencies are the same as the ones listed in Table 5.2. In addition, by analyzing the frequency response of Z_{in} at load-independent frequencies (see Figure 5.3), it can be concluded

that if $f_{6,7}$ is selected as operating frequency, ZSC will be achieved, while operating at $f_{8,9}$ will lead to ZVS.

Table 5.2. Load-independent frequencies for WPT with PLCC compensation.

Parameter [unit]	Value
$f_{1,2,3}$ [kHz]	0
$f_{4,5}$ [kHz]	80
$f_{6,7}$ [kHz]	53.16
$f_{8,9}$ [kHz]	103.09

5.4. Secondary LCC (SLCC) Compensation

In this configuration, series and LCC compensations are used in the primary and secondary sides, respectively (see Figure 5.2. (b)). In order to achieve constant voltage characteristic, Z_{out} should be zero. To this end, the following equations should be satisfied

$$C_1 = \frac{1}{\omega_0^2 L_1}. \tag{5–34}$$

$$C_{22} = \frac{1}{\omega_0^2 L_{23}}. \tag{5–35}$$

In the next two subsections, the conditions for load-independent VTR and ZVS operation of this compensation network will be investigated.

5.4.1. Zero Voltage Switching of SLCC

Based on Figure 5.2 (b), and if $\omega_0 = \frac{1}{\sqrt{L_1 C_1}} = \frac{1}{\sqrt{L_{23} C_{22}}}$, the impedance seen from the input voltage source when SLCC compensation is employed, can be obtained as follows

$$Z'_{22} = \frac{(R + jL_{23}\omega_0)\frac{1}{jC_{22}\omega_0}}{(R + jL_{23}\omega_0) + \frac{1}{jC_{22}\omega_0}} = \frac{L_{23}^2 \omega_0^2}{R} - jL_{23}\omega_0. \tag{5–36}$$

$$Z'_{21} = Z'_{22} + j(L_2 - M)\omega_0 + \frac{1}{jC_{21}\omega_0}. \tag{5–37}$$

If C_{21} is chosen as follows

$$C_{21} = \frac{1}{\beta\omega_0^2(L_2 - L_{23})} \tag{5–38}$$

Z'_{21} can be simplified to

$$Z'_{21} = \frac{L_{23}^2\omega_0^2}{R} - jM\omega_0 + j(1-\beta)\omega_0(L_2 - L_{23}) \tag{5–39}$$

Now, Z_{in} can be obtained as follows

$$Z_{in} = j(L_1 - M)\omega_0 + \frac{1}{jC_1\omega_0} + Z'_m = -jM\omega_0 + \frac{jM\omega_0 \times Z'_{21}}{jM\omega_0 + Z'_{21}} \tag{5–40}$$

After some simplification, Z_{in} can be rewritten as follows

$$Z_{in} = \frac{L_{23}^2 M^2\omega_0^2 R}{L_{23}^4\omega_0^2 + R^2(1-\beta)^2(L_{23} - L_2)^2} + \frac{j\omega_0 M^2 R^2(1-\beta)(L_{23} - L_2)}{L_{23}^4\omega_0^2 + R^2(1-\beta)^2(L_{23} - L_2)^2} \tag{5–41}$$

Therefore, input impedance angle can be calculated as follows

$$\angle Z_{in} = \arctan\left(\frac{R(1-\beta)(L_{23} - L_2)}{L_{23}^2\omega_0}\right) \tag{5–42}$$

As it can be seen, the angle of Z_{in} is independent of mutual inductance. From the above equation, it can be seen that if β=1, phase of the input impedance will be zero and ZPA can be achieved. Also, Z_{in} can be simplified to

$$Z_{in} = \frac{RM^2}{L_{23}^2} \tag{5–43}$$

Based on (5-43), if M becomes small, Z_{in} will be reduced. Thus, the input current will increase. As a result, there is need for a current limiting control in case misalignment occurs. However, the input current can be automatically controlled if load goes to infinity. For SLCC, selection of L_{23} is

very important since it can affect transfer efficiency as well as the system efficiency. This issue will be discussed in section 7.

Table 5.3. Parameters of WPT with SLCC compensation used for Z_{in} frequency analysis.

Parameter [unit]	Value
$f_{sw\text{-}inv}$ [kHz]	80
k [-]	0.22
R [Ω]	7, 23, 46, 67 and 200
L_1 [µH]	253
L_2 [µH]	249
L_{23} [µH]	38.4
C_1 [nF]	15.6
C_{22} [nF]	103
C_{21} [nF]	18.8, 18.3

Figure 5.6 shows frequency response of Z_{in} when β is 1. From the phase plot, it can be observed that at the operating frequency, phase of Z_{in} is equal to zero for all load values, while its magnitude varies with respect to the load values. Based on (5-42), if $L_{23}>L_2$, by choosing $\beta<1$ and if $L_{23}<L_2$, by choosing $\beta>1$, ZVS can be achieved.

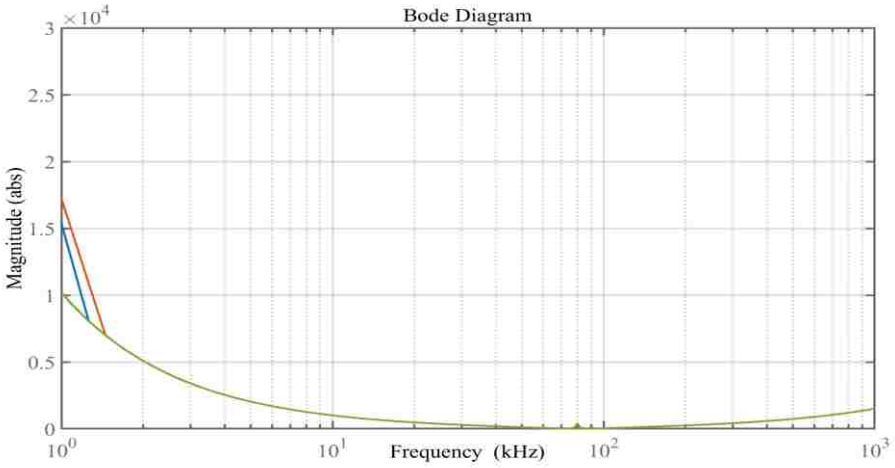

(a)

Figure 5.6. Frequency response of Z_{in} for SLCC and when β is 1 (C_{21}=18.8 nF). (a) magnitude, (b) magnitude zoomed, (c) phase, (d) phase zoomed. 7 Ω (blue), 23 Ω (red), 46 Ω (yellow), 67 Ω (purple) and 200 Ω (green) load.

(Figure 5.6 continued)

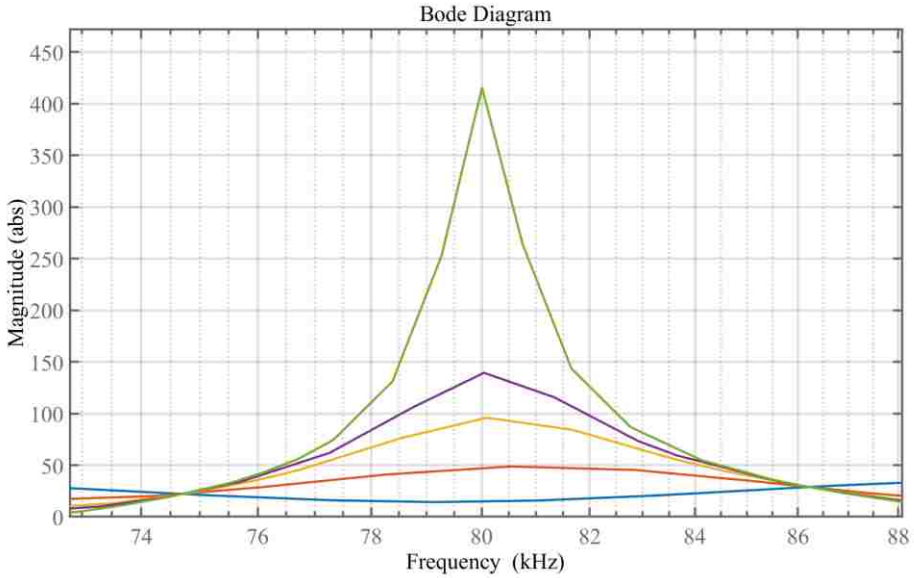

(b)

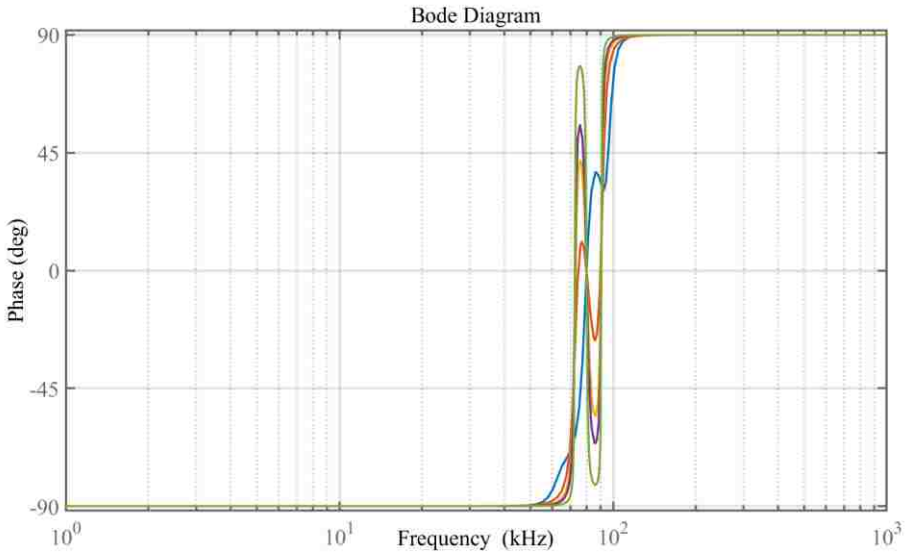

(c)
(Figure 5.6 continued)

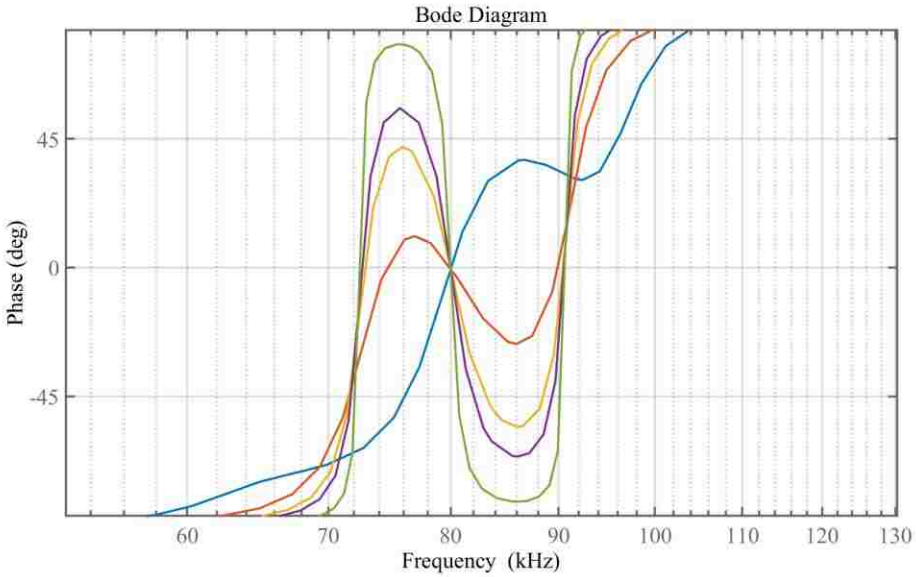

(d)

Figure 5.7 depicts frequency response of Z_{in} when β is bigger than unity. As it can be observed, although magnitude of Z_{in} at operating frequency does not change significantly when β is higher than unity, phase of Z_{in} for all loads becomes positive, which makes ZVS operation possible.

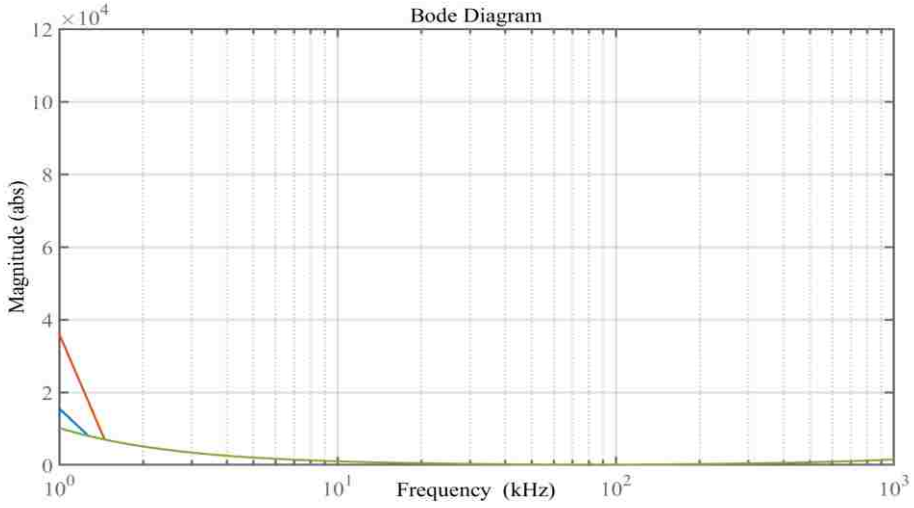

(a)

Figure 5.7. Frequency response of Z_{in} for SLCC and when β is higher than 1 (C_{21}=18.3 nF). (a) magnitude, (b) magnitude zoomed, (c) phase, (d) phase zoomed. 7 Ω (blue), 23 Ω (red), 46 Ω (yellow), 67 Ω (purple) and 200 Ω (green) load.

(Figure 5.7 continued)

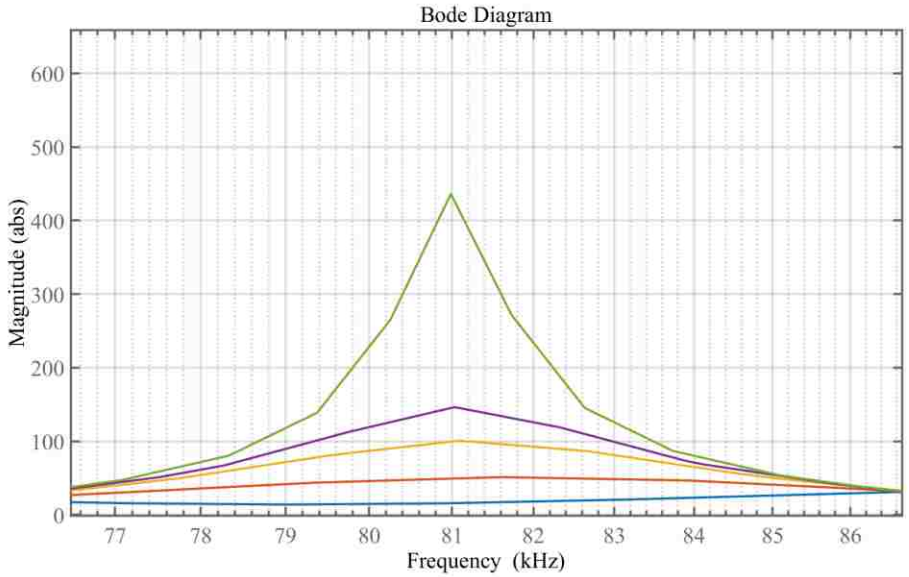

(b)

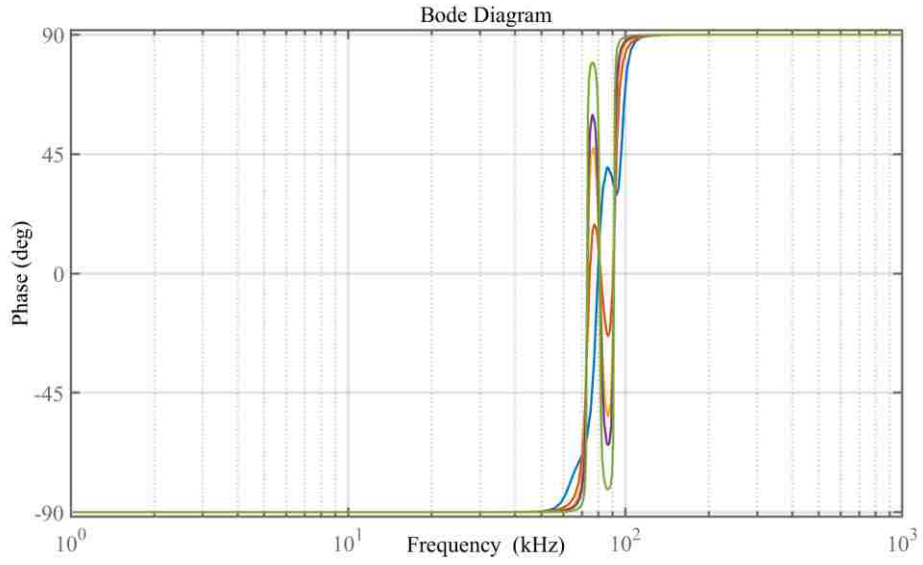

(c)

(Figure 5.7 continued)

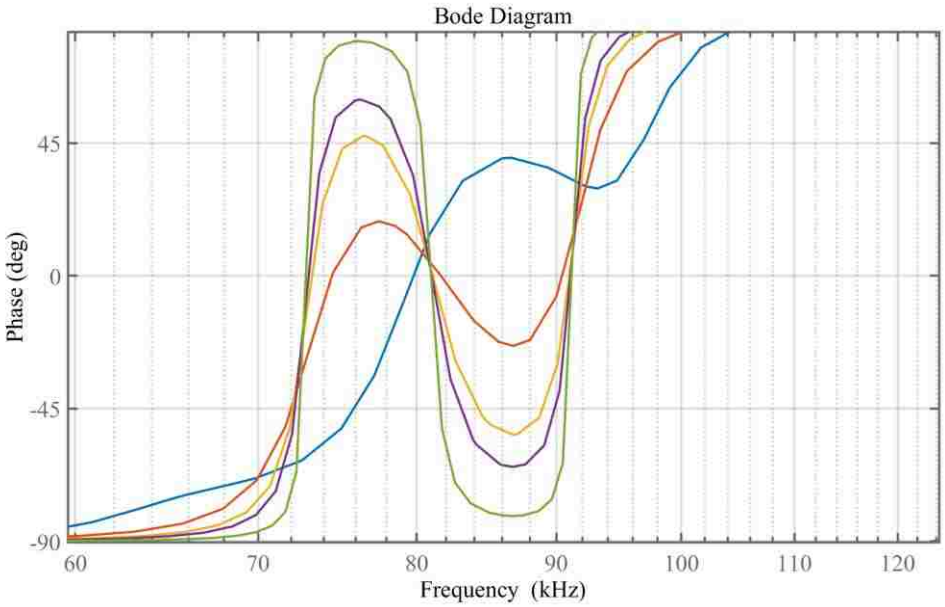

(d)

5.4.2. Load-Independent Voltage Transfer Ratio of SLCC Compensation

Based on Figure 5.2 (b), VTR of WPT with secondary LCC compensation can be obtained as follows

$$VTR = \frac{V_{out}}{V_{in}} = \frac{R}{R + sL_{23}} \times \frac{Z'_{22}}{Z'_{21}} \times \frac{Z'_m}{Z'_{in}}. \tag{5–44}$$

Based on (5-34) and (5-41), VTR can be simplified as follows

$$VTR(s) = \frac{ML_{23}s^3\omega_0^2 R}{R \times DEN_1 + DEN_0}, \tag{5–45}$$

$$DEN_1 = (L_1L_2 - M^2)s^5 + L_1\omega_0^2((1+\beta)L_2 + (1-\beta)L_{23})s^3 + L_1\omega_0^4(L_{23} + \beta(L_2 - L_{23}))s, \tag{5–46}$$

$$DEN_0 = (s^2 + \omega_0^2)L_{23}((L_1L_2 - M^2)s^4 + L_1\omega_0^2(L_2(1+\beta) + L_{23}(1-\beta))s^2 + \beta L_1\omega_0^4(L_2 - L_{23})) \tag{5–47}$$

To find frequencies with load-independent VTR characteristics, the derivative of VTR with respect to load is calculated and set equal to zero

$$\frac{\partial VTR}{\partial R} = 0 . \tag{5–48}$$

After some simplifications, the following equality can be derived

$$ML_{23}s^3\omega_0^2(s^2+\omega_0^2)L_{23}((L_1L_2-M^2)s^4+L_1\omega_0^2(L_2(1+\beta)+L_{23}(1-\beta))s^2+\beta L_1\omega_0^4(L_2-L_{23}))=0 \tag{5–49}$$

The roots of the above equation are as follows

$$\begin{aligned}
&s_{1,2,3} = 0\\
&s_{4,5} = \pm j\omega_0\\
&s_{6,7} = \pm j\sqrt{\frac{-\sqrt{L_1^2\omega_0^4(L_2+L_{23}+\beta(L_2-L_{23}))^2+\beta L_1\omega_0^4(L_2-L_{23})(4M^2-4L_1L_2)}-L_1\omega_0^2(L_2(1+\beta)+L_{23}(1-\beta))}{2M^2-2L_1L_2}}\\
&s_{8,9} = \pm j\sqrt{\frac{\sqrt{L_1^2\omega_0^4(L_2+L_{23}+\beta(L_2-L_{23}))^2+\beta L_1\omega_0^4(L_2-L_{23})(4M^2-4L_1L_2)}+L_1\omega_0^2(L_2(1+\beta)+L_{23}(1-\beta))}{2M^2-2L_1L_2}}
\end{aligned} \tag{5–50}$$

VTR at each of the above frequencies can be obtained as follows

$$VTR(s_{4,5}) = \frac{L_{23}}{M} . \tag{5–51}$$

$$VTR(s_{6,7}) = \frac{-M(\sqrt{M^2(L_2-L_{23})+L_1L_2L_{23}}-\sqrt{L_1}L_2)}{\sqrt{L_1}(M^2-L_1L_2)} = \frac{-k(\sqrt{k^2(L_2-L_{23})+L_{23}}-\sqrt{L_2})}{\sqrt{L_1}(k^2-1)} . \tag{5–52}$$

$$VTR(s_{8,9}) = \frac{M(\sqrt{M^2(L_2-L_{23})+L_1L_2L_{23}}+\sqrt{L_1}L_2)}{\sqrt{L_1}(M^2-L_1L_2)} = \frac{k(\sqrt{k^2(L_2-L_{23})+L_{23}}+\sqrt{L_2})}{\sqrt{L_1}(k^2-1)} . \tag{5–53}$$

As it can be seen, the obtained VTRs are independent of the load and only depend on parameters of the coils and compensation network. Figure 5.8 illustrates the frequency response of VTR for SLCC.

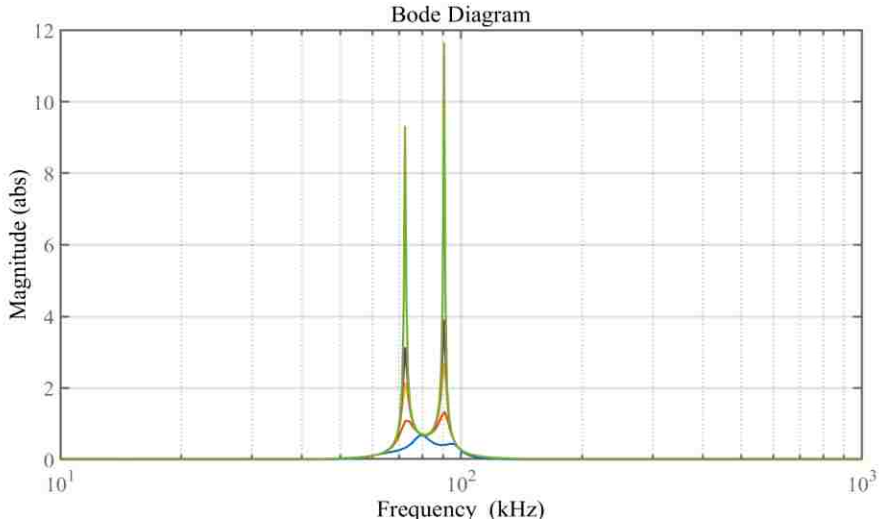

(a)

Figure 5.8. Frequency response of VTR of SLCC (C_{21}=18.8 nF). (a) magnitude, (b) magnitude zoomed, (c) phase. 7 Ω (blue), 23 Ω (red), 46 Ω (yellow), 67 Ω (purple) and 200 Ω (green) load.

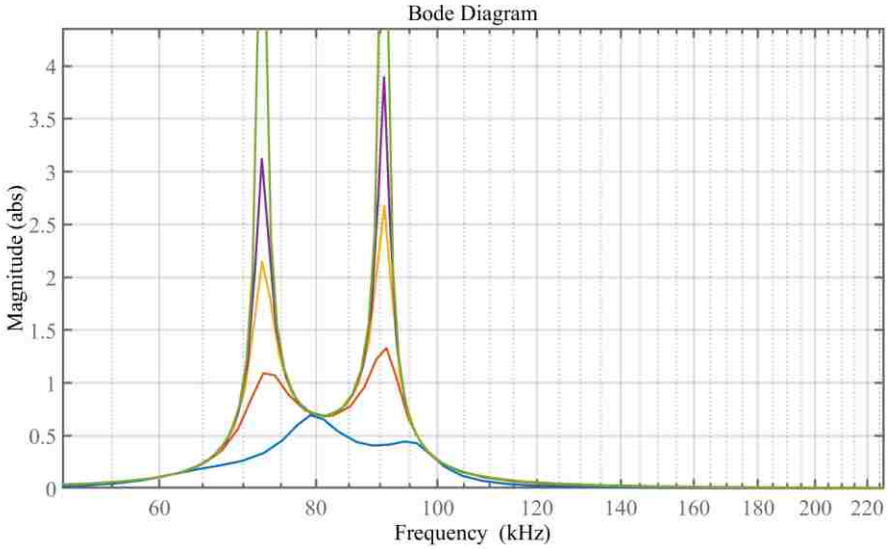

(b)

(Figure 5.8 continued)

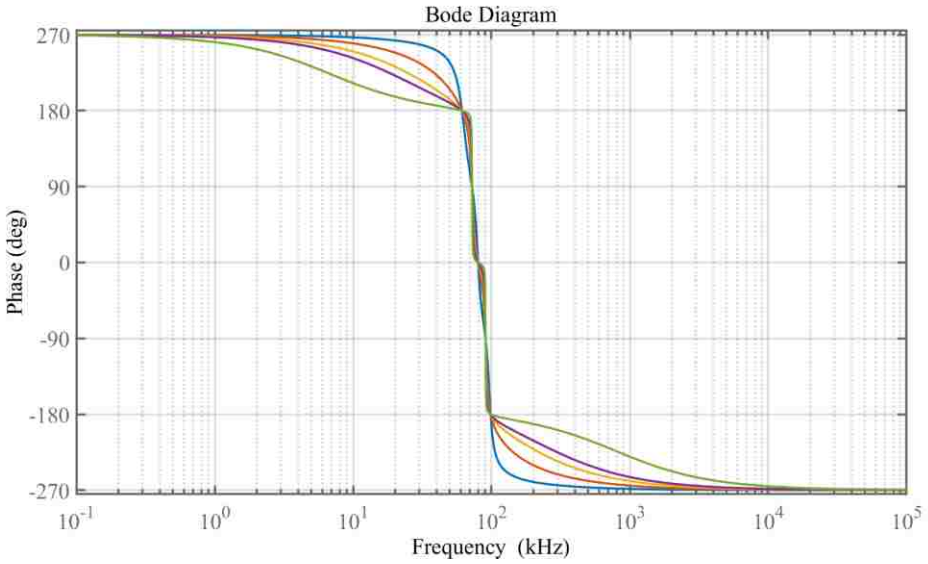

(c)

It can be seen that three load-independent frequencies exist in the frequency response. Based on (5-50), these frequencies are calculated and listed in Table 5.4.

Table 5.4. Load-independent frequencies for WPT with SLCC compensation.

Parameter [unit]	Value
$f_{1,2,3}$ [kHz]	0
$f_{4,5}$ [kHz]	80
$f_{6,7}$ [kHz]	61.26
$f_{8,9}$ [kHz]	98.48

Considering Figure 5.8, it is clear that load-independent VTR frequencies occur at the same frequencies listed in Table 5.4.

6. WPT SYSTEM EFFICIENCY

WPT system efficiency can be calculated assuming output voltage, V_{out}, output current, I_{out}, and V_{in}, input voltage are known. Since output voltage and current are DC, output power can be obtained as follows

$$P_{out} = V_{out} I_{out} . \tag{6–1}$$

6.1. High-Frequency Rectifier Efficiency

Power loss in full-bridge rectifier can be calculated using the following equation

$$P_{loss-rec} = 4(V_d I_{avg-d} + R_d I_{rms-d}^2) . \tag{6–2}$$

where, V_d is the diode forward voltage and R_d is the diode resistance. $I_{avg\text{-}d}$ and $I_{rms\text{-}d}$ are the average and rms current of each diode, which can be calculated as follows

$$I_{avg-d} = \frac{I_{out}}{2} , \tag{6–3}$$

$$I_{rms-d} = \frac{I_{out}\pi}{4} . \tag{6–4}$$

The input power and voltage of the rectifier can be calculated as follows

$$P_{in-rec} = P_{loss-rec} + P_{out} , \tag{6–5}$$

$$V_{rms-rec} = \frac{P_{in-rec}}{I_{rms-rec}} . \tag{6–6}$$

where,

$$I_{rms-rec} = \frac{I_{out}\pi}{2\sqrt{2}} . \tag{6–7}$$

6.2. Primary LCC Compensation Efficiency

Resistance seen from the rectifier input can be calculated as follows

$$R_{rec} = \frac{V_{rms-rec}}{I_{rms-rec}}. \tag{6–8}$$

Considering the conduction loss in the coils and compensation network, Z_{in} can be calculated as follows

$$Z'_{21} = j(L_2 - M)\omega_0 + R_{L2} + \frac{1}{jC_{21}\omega_0} + R_{C21} + R_{rec}, \tag{6–9}$$

$$Z'_m = \frac{jM\omega_0 \times Z_{21}}{jM\omega_0 + Z_{21}}, \tag{6–10}$$

$$Z'_{13} = \frac{1}{jC_{13}\omega_0} + R_{C13} + j(L_1 - M)\omega_0 + R_{L1} + Z_m, \tag{6–11}$$

$$Z'_{12} = \frac{Z_{13} \times (R_{C12} + \frac{1}{jC_{12}\omega_0})}{Z_{13} + (R_{C12} + \frac{1}{jC_{12}\omega_0})}, \tag{6–12}$$

$$\boldsymbol{Z'_{in} = jL_{11}\omega_0 + R_{L11} + Z_{12}}. \tag{6–13}$$

where R_{L1} and R_{L2} are ESR of primary and secondary coils, respectively, and R_{Cx} (x=21, 12 and 13) are ESR of capacitors estimated by the following equation

$$R_{Cx} = \frac{DF}{C_x\omega_0}. \tag{6–14}$$

Here, DF denotes dissipation factor of the capacitor and is available in the datasheet.

The input voltage and current of the compensation network (output voltage and current of the inverter) as well as its input power, can be calculated as follows

$$V_{coils-rms} = V_{rec-rms} \frac{Z'_{21}}{R_{rec}} \frac{Z'_m}{Z'_{13}} \times \frac{Z'_{in}}{Z'_{12}}, \tag{6–15}$$

$$I_{coils-rms} = \frac{V_{coils-rms}}{Z'_{in}}, \tag{6–16}$$

$$P_{coils} = V_{coil-rms} I_{coil-rms} \cos\delta_1, \tag{6–17}$$

where, δ_1 is the phase angle between voltage and current of the primary compensation network.

6.3. Secondary LCC Compensation Efficiency

The input impedance seen from the inverter by considering conduction losses can be obtained as follows

$$Z_{23} = R_{rec} + R_{L23} + j\omega_0 L_{23}. \tag{6–18}$$

$$Z_{22} = \frac{Z_{23}(R_{C22} + \frac{1}{jC_{22}\omega_0})}{Z_{23} + R_{C22} + \frac{1}{jC_{22}\omega_0}}. \tag{6–19}$$

$$Z_{21} = j(L_2 - M)\omega_0 + Z_{22} + R_{L2} + R_{C21} + \frac{1}{jC_{21}\omega_0}. \tag{6–20}$$

$$Z_m = \frac{jM\omega_0 Z_{21}}{jM\omega_0 + Z_{21}}. \tag{6–21}$$

$$Z_{in} = j(L_1 - M)\omega_0 + Z_m + R_{L1} + R_{C1} + \frac{1}{jC_1\omega_0}. \tag{6–22}$$

The input voltage and current of SLCC compensation network (output voltage and current of the inverter) as well as its input power, can be calculated as follows

$$V_{coils-rms} = V_{rec-rms} \frac{Z_{23}}{R_{rec}} \frac{Z'_{21}}{Z'_{22}} \times \frac{Z'_{in}}{Z'_m}, \tag{6–23}$$

$$I_{coils-rms} = \frac{V_{coils-rms}}{Z'_{in}}, \tag{6–24}$$

$$P_{coils} = V_{coil-rms} I_{coil-rms} \cos\delta_2 . \tag{6–25}$$

where, δ_2 is the phase angle between voltage and current of the secondary compensation network.

6.4. High Frequency Inverter Efficiency

Input voltage of the inverter (V_{DC}) can be estimated using the following equation

$$V_{DC} = V_{coil-\max} + R_{ds} I_{mos-rms} . \tag{6–26}$$

where, R_{ds} is the on-state resistance of the inverter's switch. $I_{mos\text{-}rms}$ can be calculated as follows

$$I_{mos-rms} = I_{coil-rms} \sqrt{\frac{2(\pi - \varphi_v) + \sin(2\varphi_v)}{8\pi}} . \tag{6–27}$$

where, φ_v is the phase difference between the output voltage and current of the inverter. The diode rms and average currents are calculated as follows

$$I_{diode-rms} = I_{coil-rms} \sqrt{\frac{2\varphi_v - \sin(2\varphi_v)}{8\pi}} . \tag{6–28}$$

$$I_{diode-avg} = \sqrt{2} I_{coil-rms} \sqrt{\frac{\cos(\varphi_v) - 1}{\omega_0}} . \tag{6–29}$$

Power losses in the inverter are obtained as

$$P_{loss-cond} = 4 R_{ds} I^2_{coil-rms} , \tag{6–30}$$

$$P_{loss-sw} = P_{coss} + P_{QRR} + P_{loss-diode} = C_{OSS} V^2_{dc} f_{sw} + Q_{RR} V_{dc} f_{sw} + 4(V_f I_{diode-avg} + R_d I^2_{diode-rms}) , \tag{6–31}$$

$$P_{loss-inv} = P_{loss-cond} + P_{loss-sw} . \tag{6–32}$$

in which, $P_{loss\text{-}inv}$, $P_{loss\text{-}cond}$, $P_{loss\text{-}sw}$, P_{COSS}, P_{QRR} and $P_{loss\text{-}diode}$ are the inverter loss, conduction loss, switching loss, the loss in output capacitor of the switches, reverse recovery loss and diode loss. f_{sw}, C_{OSS}, Q_{RR} denote switching frequency, output capacitance of switch and reverse recovery charge of switches, respectively. Finally, the inverter input power and input current and voltage of the inverter can be calculated as follows

$$P_{inv} = P_{coils} + P_{loss-inv}, \tag{6–33}$$

$$I_{DC} = \frac{2\sqrt{2}I_{coil-rms}}{\pi}, \tag{6–34}$$

$$V_{DC} = \frac{P_{inv}}{I_{DC}}. \tag{6–35}$$

6.5. Buck-Boost Converter Efficiency

The buck-boost converter can work in three modes: buck, boost and buck-boost. In the buck-boost mode, all switches are switching and therefore, switching loss is high. Thus, the converter is controlled to not work in buck-boost mode and instead work in buck or boost mode.

In the buck-boost converter, hard-switching occurs and therefore, both turn-on and turn-off switching losses exist. The losses in the switches can be calculated from the following equation

$$P_{loss-conv} = P_{cond-conv} + P_{sw-conv} + P_{ind} + P_{sn}. \tag{6–36}$$

where, $P_{loss\text{-}conv}$, $P_{cond\text{-}conv}$, $P_{sw\text{-}conv}$, P_{ind} and P_{sn} denote power loss in the converter, conduction loss in the switches, switching loss, inductor losses and snubber loss, respectively. These losses are obtained as follows

$$P_{cond-conv} = 2R_{ds}I_{DC}^2, \tag{6–37}$$

$$P_{sw-conv} = P_{sw-conv} + P_{diode-conv} + P_{COSS} = \frac{1}{2} V_{in} I_{DC} (t_r + t_f) f_{sw} + \frac{1}{2} V_d I_{DC} (t_r + t_f) f_{sw} + C_{OSS} V_{in}^2 f_{sw}, \quad (6\text{–}38)$$

$$P_{sn} = V_{in}^2 f_{sw} C_{sn}, \quad (6\text{–}39)$$

$$P_{ind} = R_{Lconv} I_{DC}^2. \quad (6\text{–}40)$$

Note that the core loss in the inductor is negligible and can be neglected.

The power loss in the boost mode can be obtained from similar equations, except V_{DC} and I_{in} must be used instead of V_{in} and I_{DC}, respectively. I_{in} and P_{in} can be estimated from the following equations

$$I_{in} = \frac{V_{DC} I_{DC}}{V_{in}}, \quad (6\text{–}41)$$

$$\boldsymbol{P_{in} = V_{in} I_{in}}. \quad (6\text{–}42)$$

6.6. WPT System Efficiency

Following the above calculations, efficiency of each power conversion stage as well as the system efficiency can be calculated using the following equations

$$\eta_{rec} = \frac{P_{out}}{P_{in-rec}}, \quad (6\text{–}43)$$

$$\eta_{coils} = \frac{P_{in-rec}}{P_{coils}}, \quad (6\text{–}44)$$

$$\eta_{inv} = \frac{P_{coils}}{P_{inv}}, \quad (6\text{–}45)$$

$$\eta_{conv} = \frac{P_{inv}}{P_{in}}, \quad (6\text{–}46)$$

$$\eta_{sys} = \frac{P_{out}}{P_{in}}. \tag{6–47}$$

Here, η_{rec}, η_{coils}, η_{inv}, η_{conv} and , η_{sys} are the efficiency of the HF rectifier, coils, inverter, DC/DC converter and the WPT system, respectively.

7. TIME-WEIGHTED TRANSFER AVERAGE EFFICIENCY

Batteries are commonly charged with constant current (CC) followed by constant voltage (CV) when their voltage reaches the cut off voltage at rated power. In this way, equivalent resistive load of battery varies in a wide range. Figure 7.1 shows the charging curve of a 25Ah Li-ion battery (with Panasonic NCR18650PF cells) used in the experimental setup.

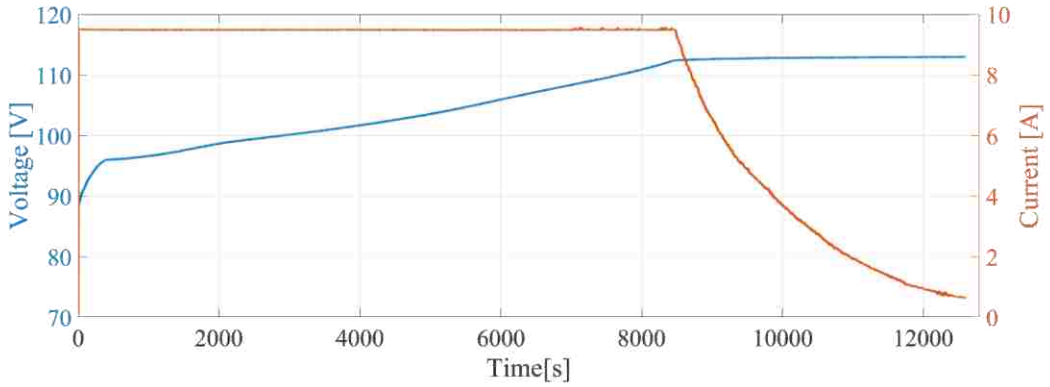

Figure 7.1. Experimental charging curve of prototype Li-ion battery

In the literature, efforts are made to design primary and secondary coils to increase the WPT system's maximum efficiency. Figure 7.2 (a) depicts system maximum efficiency variation with respect to inductance value of the primary and secondary coils for PLCC compensation networks, respectively. Also, Figure 7.2 (b) shows the load at which system maximum efficiency occurs with respect to primary and secondary coils inductance. The calculation of system efficiency is based on equations provided in section 6 and also based on parameters listed in Table 7.1, Table 7.2 and Table 7.3. As it can be seen, by increasing the inductance value of the primary and secondary coils or quality factors of the coils, system The calculation of system efficiency is based on equations provided in section 6 and also based on parameters listed in Table 7.1, Table 7.2 and Table 7.3. As it can be seen, by increasing the inductance value of the primary and secondary coils or quality factors of the coils, system maximum efficiency increases for both compensation networks.

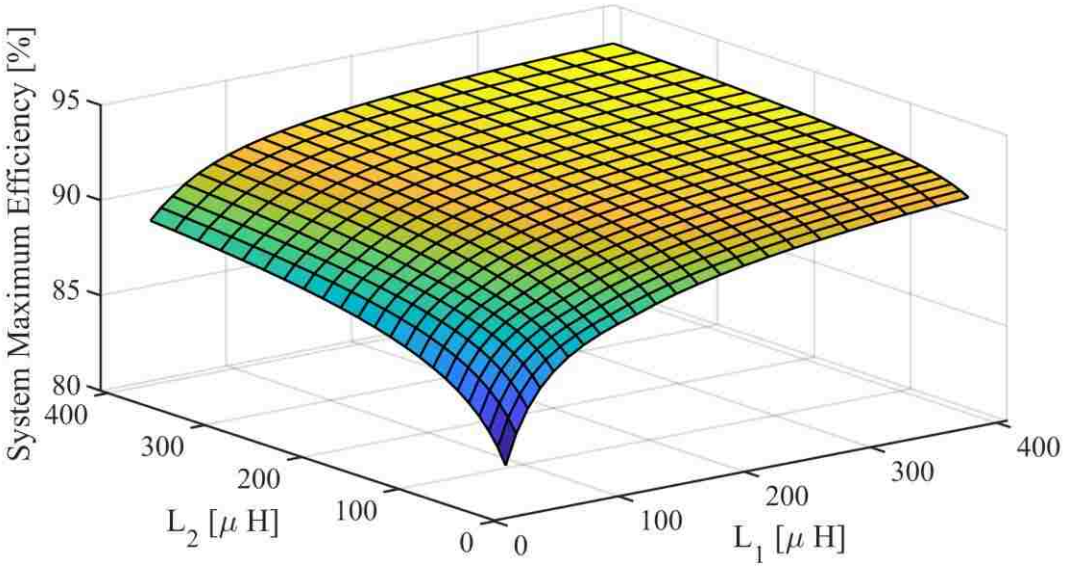

(a)

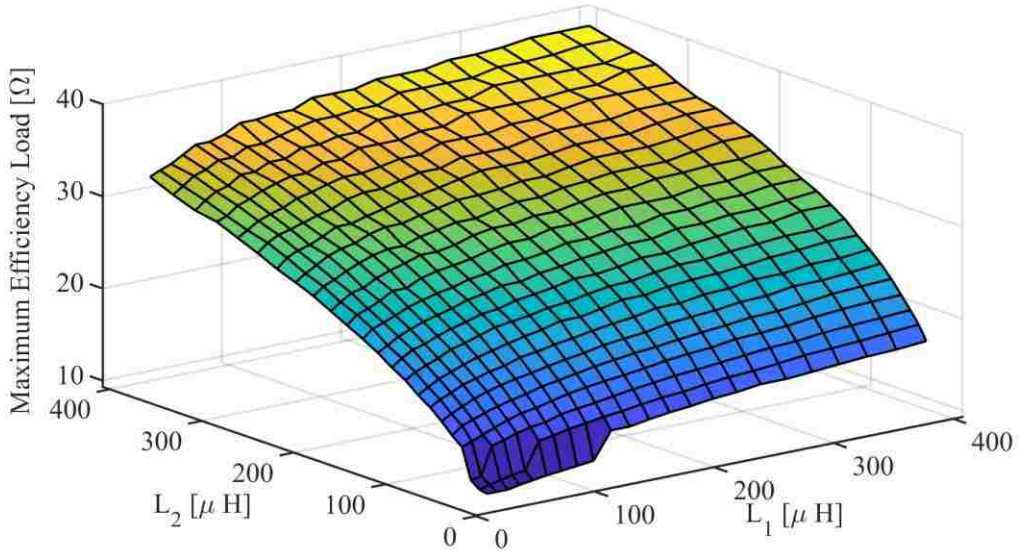

(b)

Figure 7.2. Variation of (a) system maximum efficiency and (b) maximum efficiency load of circular coil as function of L_1 and L_2 for primary LCC

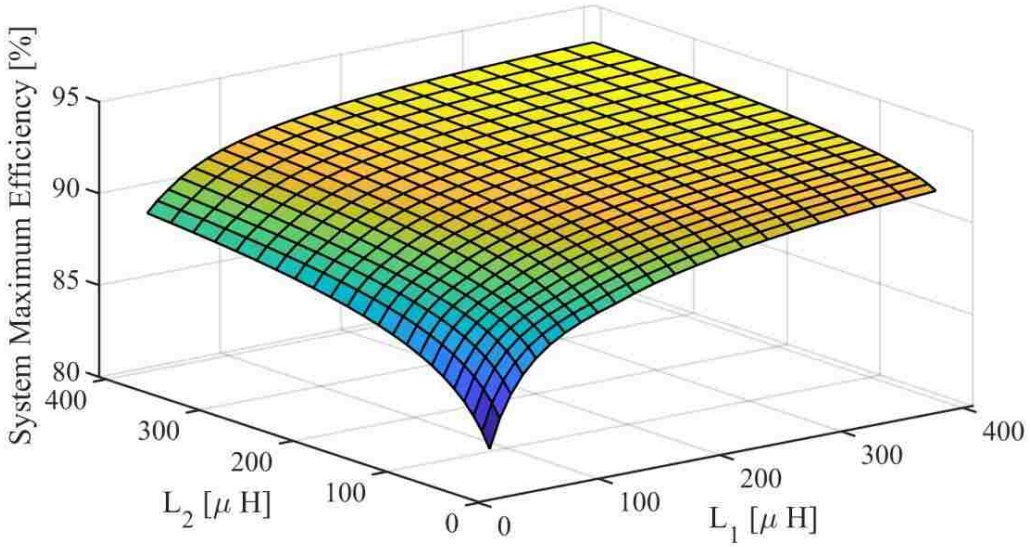

(a)

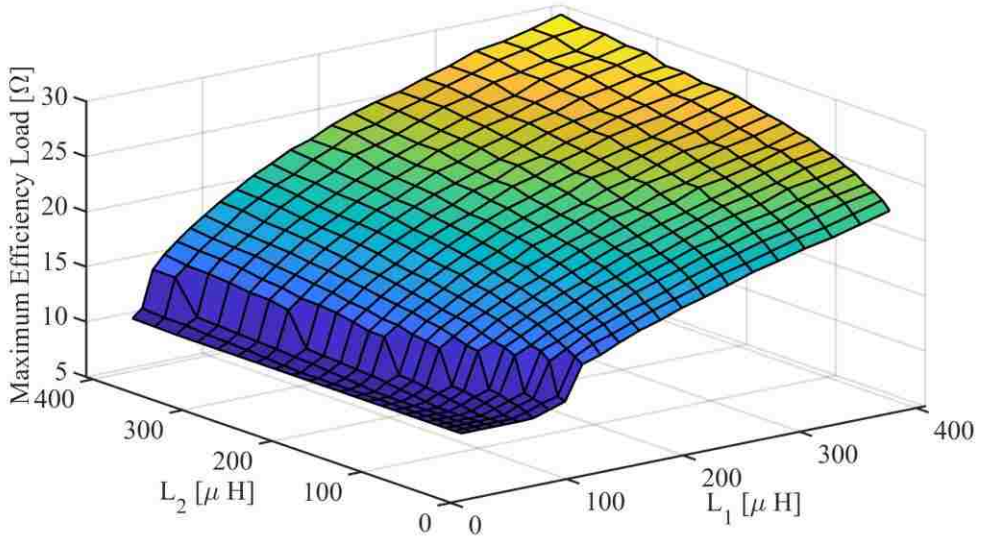

(b)

Figure 7.3. Variation of (a) system maximum efficiency and (b) maximum efficiency load of circular coil as function of L_1 and L_2 for primary LCC

In addition, it can be observed that by increasing the secondary inductance, the load at which the maximum efficiency occurs increases; however, at a specific secondary inductance, variation of maximum load with respect to primary inductance is low.

Table 7.1. Coils and compensation network specifications.

Parameter [unit]	Value
$f_{sw\text{-}inv}$ [kHz]	80
k [-]	0.22
V_{in} [V]	180
M/L_{23}	0.7
M/L_{11}	0.7
DF	2.5×10^{-4}

Table 7.2. Rectifier and inverter specifications.

Parameter [unit]	Value
V_d [V]	0.6
R_d [Ω]	0.02
R_{ds} [Ω]	0.025
Q_g [nC]	0.7
t_r [ns]	100
t_f [ns]	100
V_f [V]	0.8
R_d [Ω]	0.014
C_{OSS} [nF]	0.393
$f_{sw\text{-}inv}$ [kHz]	80

Table 7.3. DC-DC converter specifications.

Parameter [unit]	Value
R_{ds} [Ω]	0.065
Q_g [nC]	35
t_r [ns]	40
t_f [ns]	20
V_f [V]	4
R_d [Ω]	0.2
C_{sn} [pF]	1000
f_{sw} [kHz]	80

Figure 7.3 illustrates the maximum efficiency and the load at which the maximum efficiency of the WPT system with SLCC compensation occurs for variation of primary and secondary coils. Similar to the system with PLCC compensation network, by increasing the inductance of the primary and secondary coils, system maximum efficiency increases. In contrast to system with PLCC compensation, in the system with SLCC compensation, maximum efficiency load increases with increase of the primary coil inductance, while rate of increase of the maximum efficiency load is lower for increases in the secondary coil inductance. It is worth noting that in these tests, system maximum efficiency for both compensation networks is about 93%. Also, L_{11} and L_{23} in PLCC and SLCC compensations, respectively, are chosen such that VTR of WPT becomes 0.7.

As it was mentioned, the battery demand varies in a wide range. Generally, increasing the system maximum efficiency at one point (even at rated point) may not result in improved *overall* system efficiency and reduced losses during the battery charge. In this work, time-weighted average efficiency (TWAE) is defined as (7-1) and efforts are made towards improving this feature

$$\eta_{avg} = \frac{\int_0^{T_{ch}} P_{out} dt}{\int_0^{T_{ch}} (P_{out} + P_{loss}) dt} = \frac{\int_0^{T_{ch}} P_{out} dt}{\int_0^{T_{ch}} (P_{out} / \eta) dt} . \qquad (7\text{–}1)$$

Here, η_{avg} denotes TWAE during charging period, T_{ch}, and P_{out} and P_{loss} represent instantaneous output power and power loss, respectively.

As discussed before, with fixed outer and inner diameters of the coils, the coupling coefficient varies insignificantly with respect to the turn space. Thus, it can be assumed constant. However, by changing the number of turns, the coils inductance and resistance, hence the efficiency, vary. This feature can be taken advantage of for improving TWAE while reducing the required material and accordingly, the cost.

The inductance of a coil with a particular shape can be estimated by $L = \lambda L_o$, where, λ is a coefficient that depends on configuration of the pad (such as structure of ferrite and aluminum). L_o is inductance of a coil and for spiral and square coils can be formulated as follows [3]

$$L_o = \frac{\mu n^2 d_{avg} c_1}{2} (\ln(c_2 / \rho) + c_3 \rho + c_4 \rho^2) . \tag{7–2}$$

where, n is turn number and c_i are coefficients depending on the layout of coils and are summarized in Table 7.4. Also, d_{avg} is average of coil's diameter (length) and ρ is calculated from following equation

$$\rho = \frac{d_o - d_i}{d_o + d_i} . \tag{7–3}$$

Table 7.4. Coefficient for self-inductance expression

Layout	c_1	c_2	c_3	c_4
Circular	1.00	2.46	0	0.2
Square	1.27	2.07	0.18	0.13

After calculating L_o for a specific coil layout from (7-2), λ can be obtained by dividing the inductance obtained by Ansys Maxwell simulation. Following such a procedure, λ is obtained as 1.45 and 1.37 for the circular and square coils, respectively. Figure 7.4 shows the inductances calculated from (7-2) and obtained from Ansys Maxwell with respect to turn number variation.

As it can be seen, the results from the employed model and Ansys Maxwell are very close. Therefore, after obtaining the inductance for one or more number of turns in Ansys Maxwell, λ can be obtained. Having λ, inductance of the coils can be calculated readily thereafter.

The estimated length of circular and square coils, D, can be calculated using (7-4) and (7-5)

$$D = \frac{n\pi}{2} (d_i + d_o) . \tag{7–4}$$

$$D = n(2(d_i + d_o) - R_{ch}) \,. \tag{7–5}$$

Here, R_{ch} denotes radius change, d_i and d_o denote inner and outer diameter of circular coil, respectively, and internal length and external length of square coil.

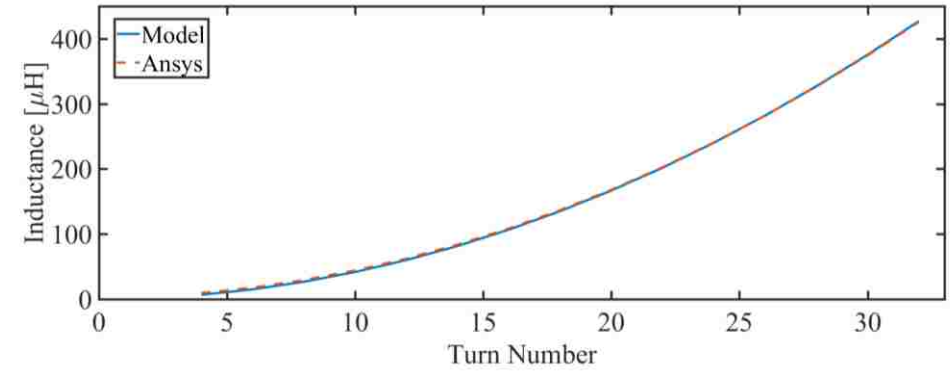

(a)

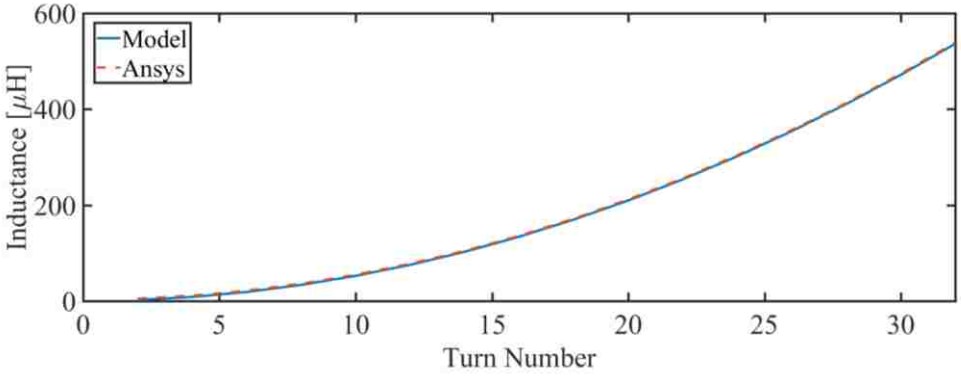

(b)

Figure 7.4. Inductance of coils based on modeling and Ansys Maxwell (a) circular and λ=1.45 (b) square and λ=1.37

Resistance of the coils can be calculated as

$$R = R_{pu} D \,. \tag{7–6}$$

where, R_{pu} is the coil resistance per meter.

As it was discussed, L_{11} and L_{23} affect efficiency of a WPT system with PLCC and SLCC, respectively; therefore, wise selection of them is of great importance. Figure 7.5 shows variation of average efficiency with respect to L_{11}/M for WPT system with PLCC and primary and secondary

coils both with 25 turns. Output power and load values are obtained from charging curve of the battery for calculating TWAE. Per meter AC resistance of the coil at 85 kHz is measured by E5071C Agilent Network Analyzer and inductance is measured with Global Specialties LCR-600. Based on this result, L_{11}=1.4M is selected and used for the rest of this work.

Figure 7.6 (a) and (b) depict, respectively, variation of time-weighted transfer average efficiency (TWTAE) and time-weighted system average efficiency (TWSAE) with respect to primary and secondary coils inductance when PLCC compensation is adopted. It can be seen that for both transfer and system efficiencies, the maximum occurs when primary coil is large, even when the secondary coil inductance is small. This result contradicts those obtained for system maximum efficiency where by increasing both the primary and secondary coils turns, the system maximum efficiency increases. In other words, a design based on system average efficiency rather than system maximum efficiency not only leads to lower power losses throughout the charging period, but also results in reduced cost and weight.

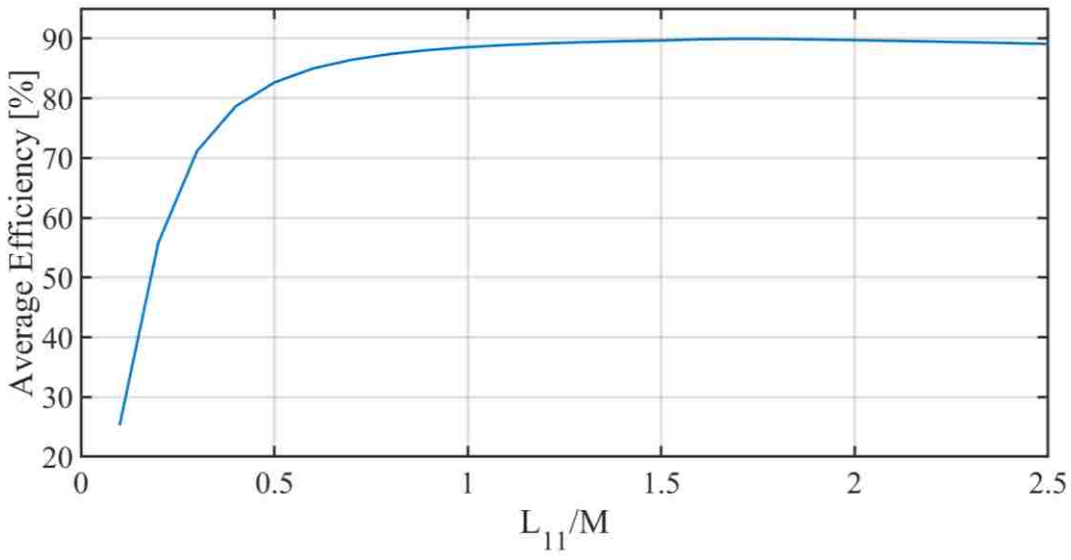

Figure 7.5. System average efficiency with respect to L_{11}/M for PLCC compensation and 25 turns primary and secondary coils.

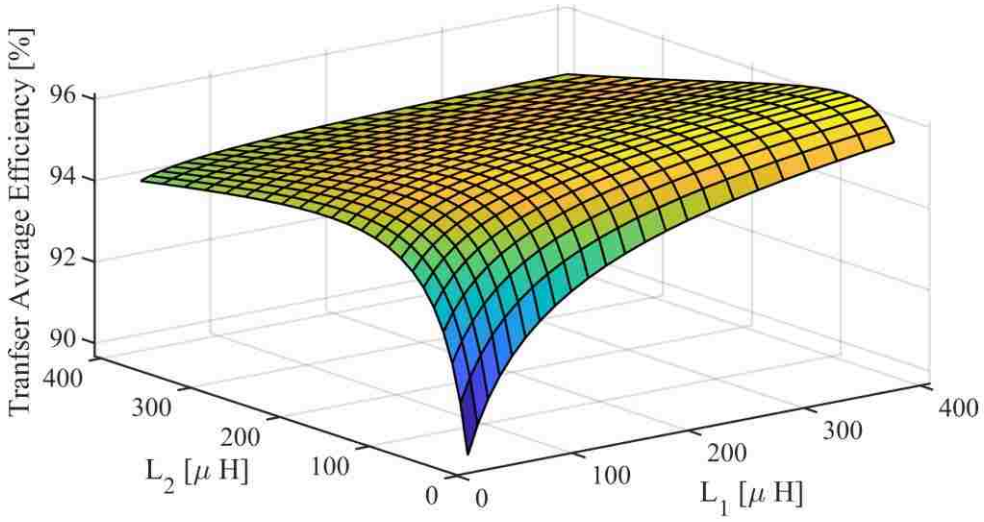

(a)

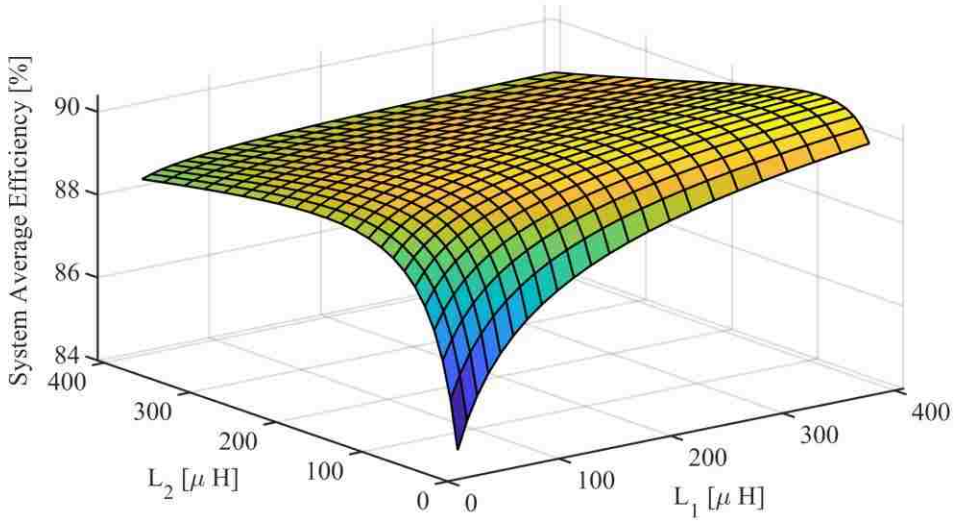

(b)

Figure 7.6. Variation of (a) TWTAE and (b) TWSAE of circular pad as function of L_1 and L_2 for primary LCC and $L_{11}=M/0.7$.

The next design is carried out for a WPT system with SLCC compensation network. Figure 7.7 illustrates system average efficiency variations with respect to L_{23}/M when the primary and secondary coils both have 25 turns. Based on the obtained results, L23=0.7M is selected that leads

to high system average efficiency. In addition, similar to WPT system with PLCC compensation network, VTR ratio is set to 0.7.

In the next step, transfer average efficiency and system average efficiency are obtained for the primary and secondary coils inductance values. Figure 7.8 (a) and (b) show the obtained results. The results shows that for a WPT system with SLCC compensation network, increasing primary and secondary coils turn number will increase the system average efficiency. This conclusion is similar to what was obtained for the system maximum efficiency with SLCC compensation network (see Figure 7.3).

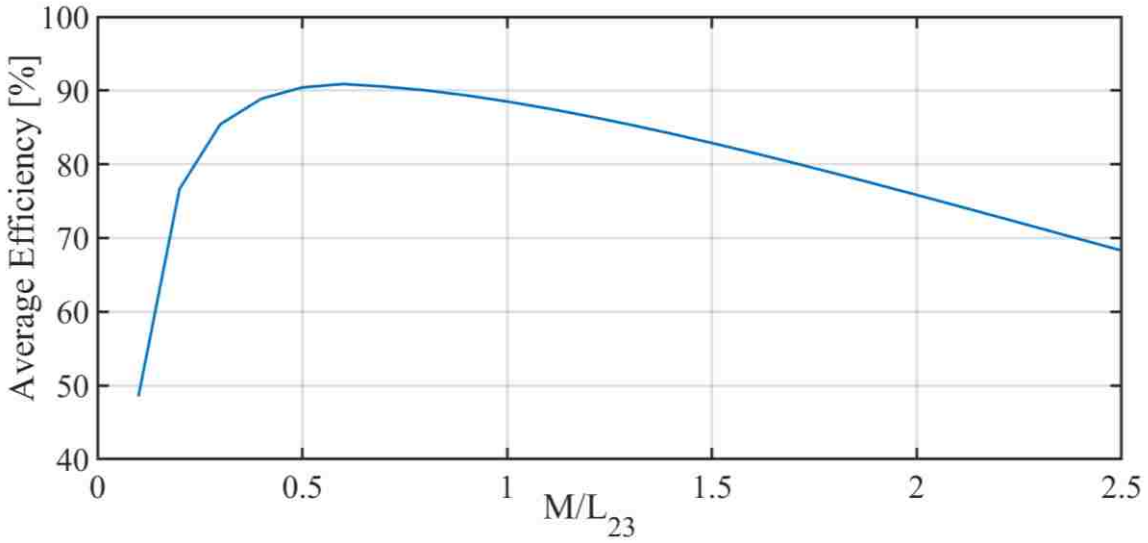

Figure 7.7. System average efficiency with respect to M/L_{23} for SLCC compensation and 25 turns primary and secondary coils.

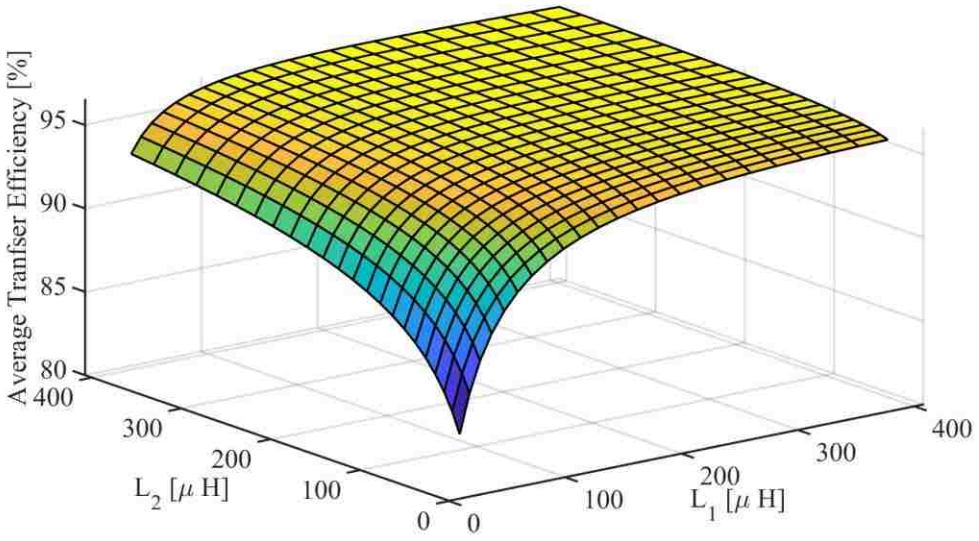

(a)

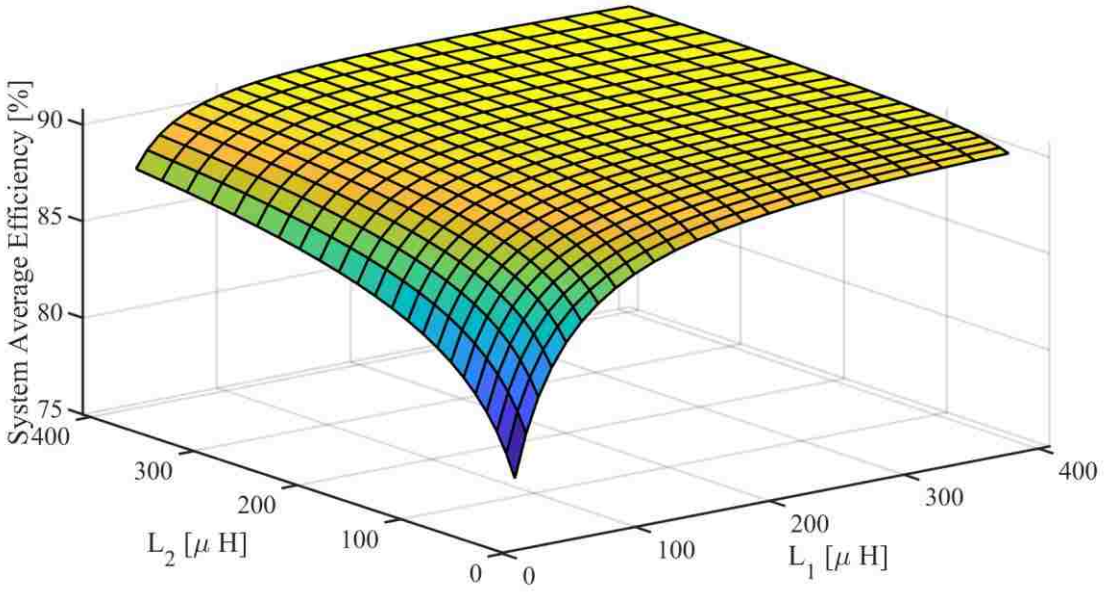

(b)

Figure 7.8. Variation of (a) TWTAE and (b) TWASE of circular pad as function of L_1 and L_2 for secondary LCC and $L_{23}=M/0.7$.

Comparing results obtained for WPT systems with PLCC and SLCC compensation networks show that similar system average efficiency is achievable with less volume of wire for PLCC. In

addition, compensation on the primary side helps with lighter WPT as well as saving space on the vehicle side while for SLCC compensation, the coil of the secondary side should be large to achieve high system average efficiency. This means heavy coil on the vehicle side.

8. MATLAB SIMULATION RESULTS

To evaluate the feasibility of the proposed WPT system, few tests are conducted in Matlab/ Simulink. Figure 5.1 depicts the WPT system modeled in Matlab/Simulink. The battery is modeled as a resistance. Table 8.1 summarizes the WPT system parameters. In the first test, the reference voltage is set to 110 V and equivalent load is R=11.5 Ω. Figure 8.1 shows the input and output voltages, output voltage and current of the HF inverter and input voltage and current of the rectifier.

Table 8.1. WPT system parameters in Matlab/Simulink

Parameter [unit]	Value
$f_{sw\text{-}inv}$ [kHz]	80
k [-]	0.22
R [Ω]	11.5, 67.5
V_{in} [V]	180
V_{out} [V]	110
C_{DC} [mF]	6
C_f [µF]	0.22
L_f [µH]	240
L_{conv} [µH]	240
L_1 [µH]	253
L_2 [µH]	249
L_{23}	38.5
L_{11}	76.5
C_{12} [nF]	51.7
C_{13} [nF]	21.7
C_{21} [nF] for PLCC	15.9
C_1 [nF]	15.6
C_{22} [nF]	103
C_{21} [nF] for SLCC	18.3

As it can be seen from Figure 8.1 (a), closed loop control of DC-DC converter works satisfactorily and the output voltage is maintained at about 110 V. From Figure 8.1 (b), it is obvious that current of the inverter is lagging the voltage, which confirms ZVS operation of the system. In

addition, based on Figure 8.1 (b) and Figure 8.1 (c), VTR of WPT can be determined, which is VTR=112/166≈0.674. In the second test, output load is selected as 67.5 Ω.

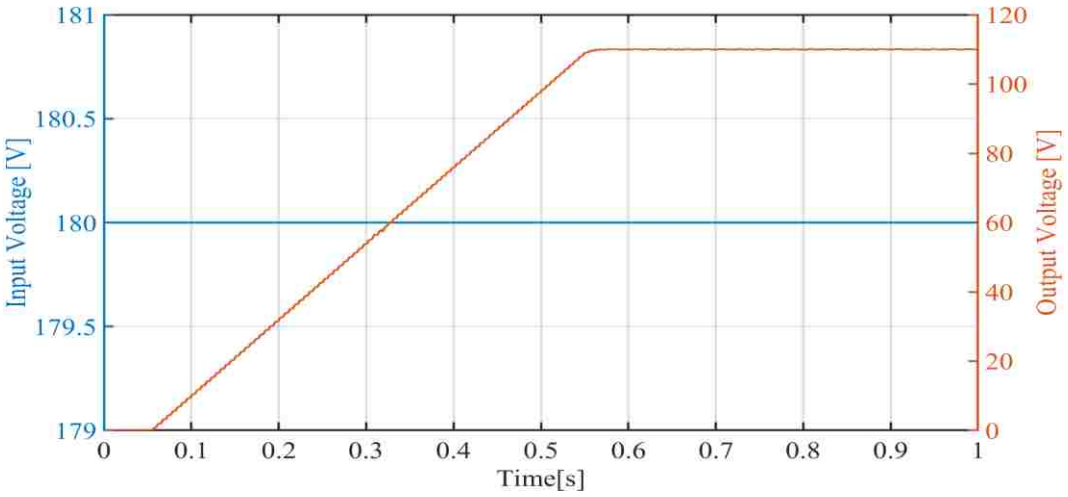

(a)

Figure 8.1. Simulation results for WPT system with primary LCC compensation when output voltage reference set to 110 V and load is 11.5 Ω (a) input and output voltage (b) HF inverter output voltage and current (d) input voltage and current of rectifier.

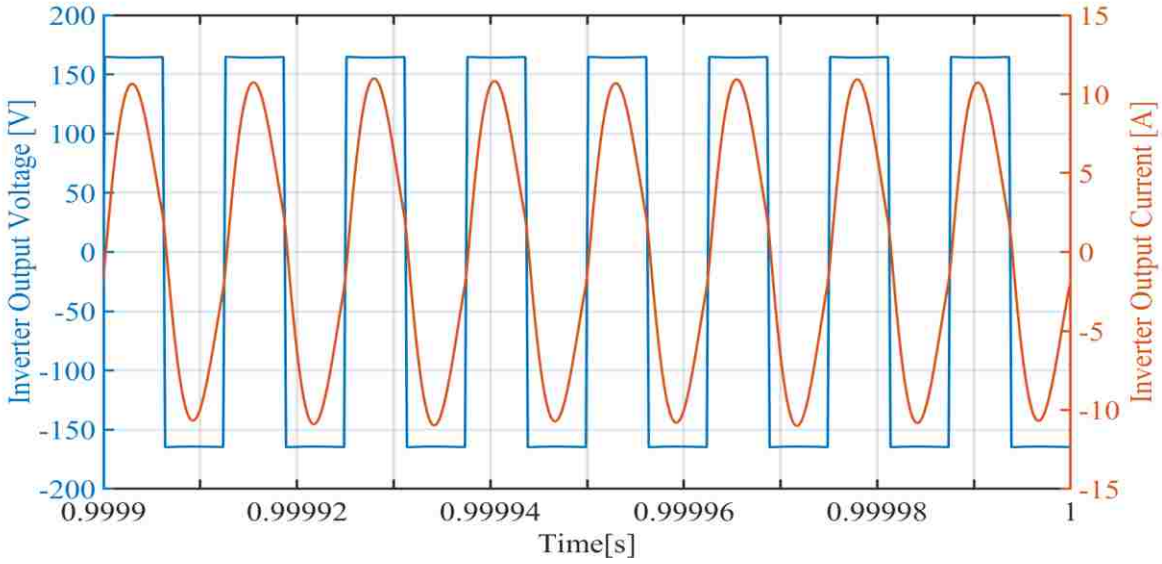

(b)

(Figure 8.1 continued)

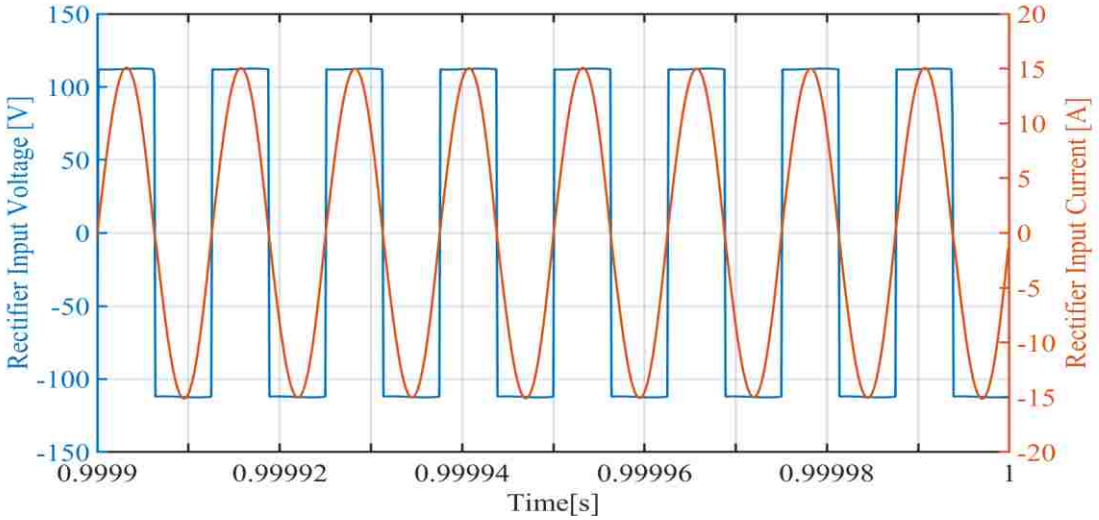

(c)

Figure 8.2 shows the obtained results. As it can be seen, the output voltage follows the reference. From output voltage and current waveforms of the inverter, it can be concluded that Z_{in} is inductive and the inverter works in ZVS mode. From the inverter output voltage and the rectifier input voltage waveforms, VTR is calculate as VTR=111.9/158≈0.71, which is close to what is expected from theory. This result shows load-independent VTR of the proposed PLCC compensation.

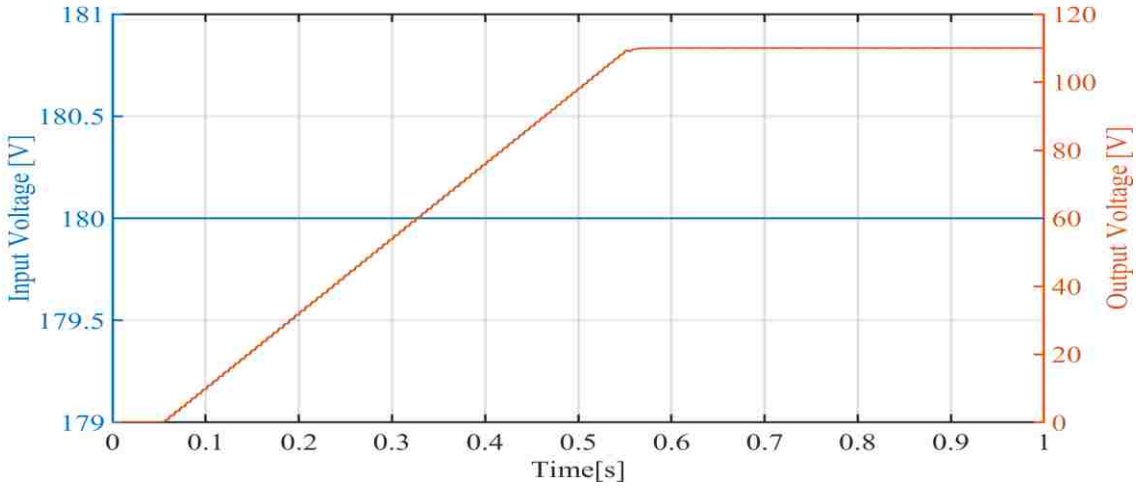

(a)

Figure 8.2. Simulation results for WPT system with primary LCC compensation when output voltage reference set to 110 V and load is 67.5 Ω (a) input and output voltage (b) HF inverter output voltage and current (d) input voltage and current of rectifier.

(Figure 8.2 continued)

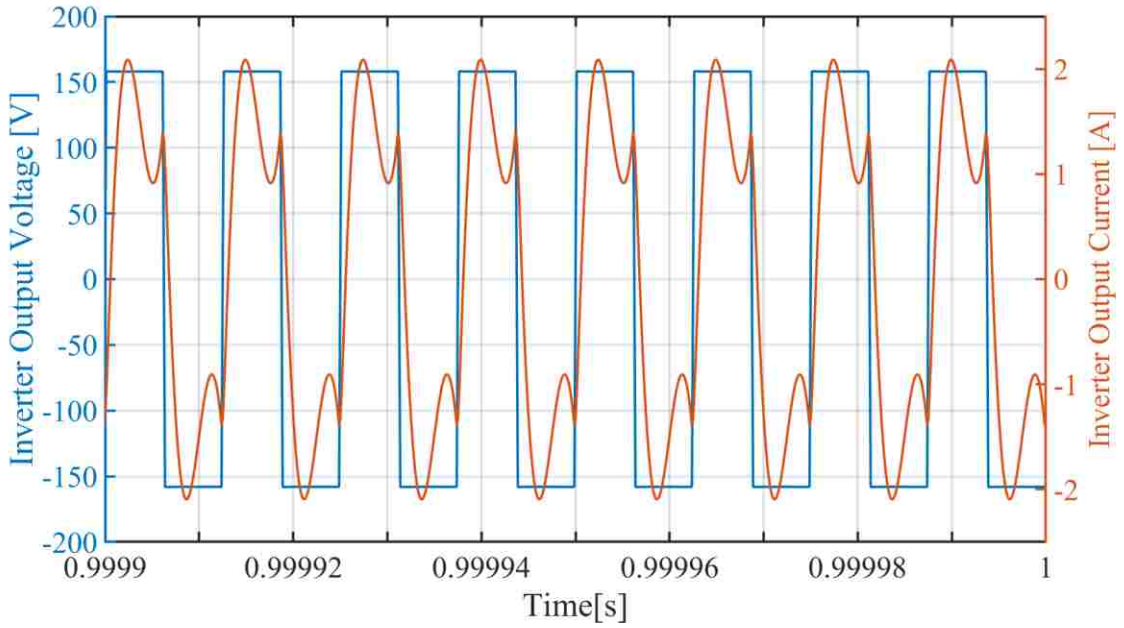

(b)

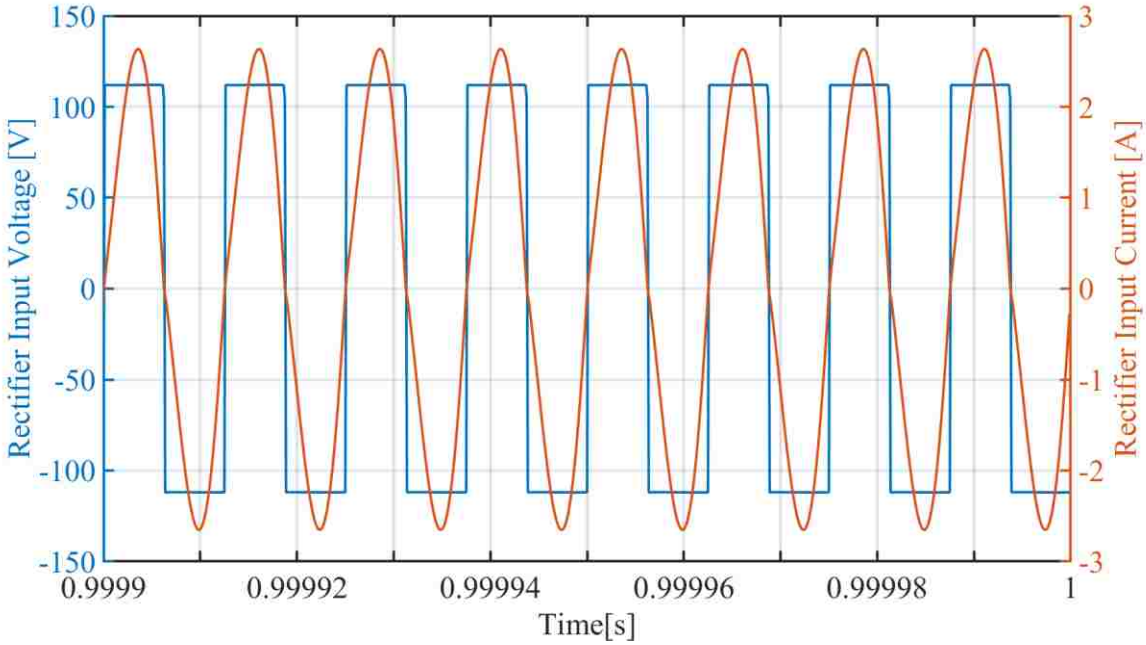

(c)

For the next test, WPT with SLCC compensation is simulated (see specification in Table 8.1). Similar to PLCC compensation simulations, two values are chosen for the load (11.5 Ω and 67.5 Ω). From Figure 8.3 (b), it can be seen that current is lagging the voltage and the inverter works in ZVS mode. Also, VTR of the system is VTR=112/164.8≈0.68. The slight discrepancy between

obtained results in simulation and what is expected from theory is attributed to conductive losses in the coils and compensation networks.

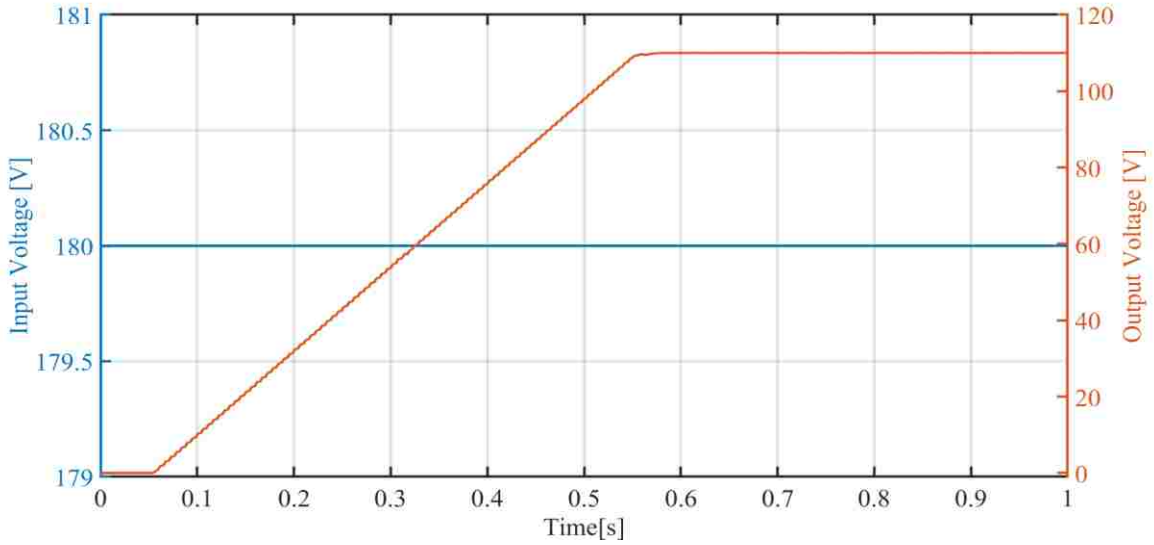

(a)

Figure 8.3. Simulation results for WPT system with primary LCC compensation when output voltage reference set to 110 V and load is 11.5 Ω (a) input and output voltage (b) HF inverter output voltage and current (d) input voltage and current of rectifier.

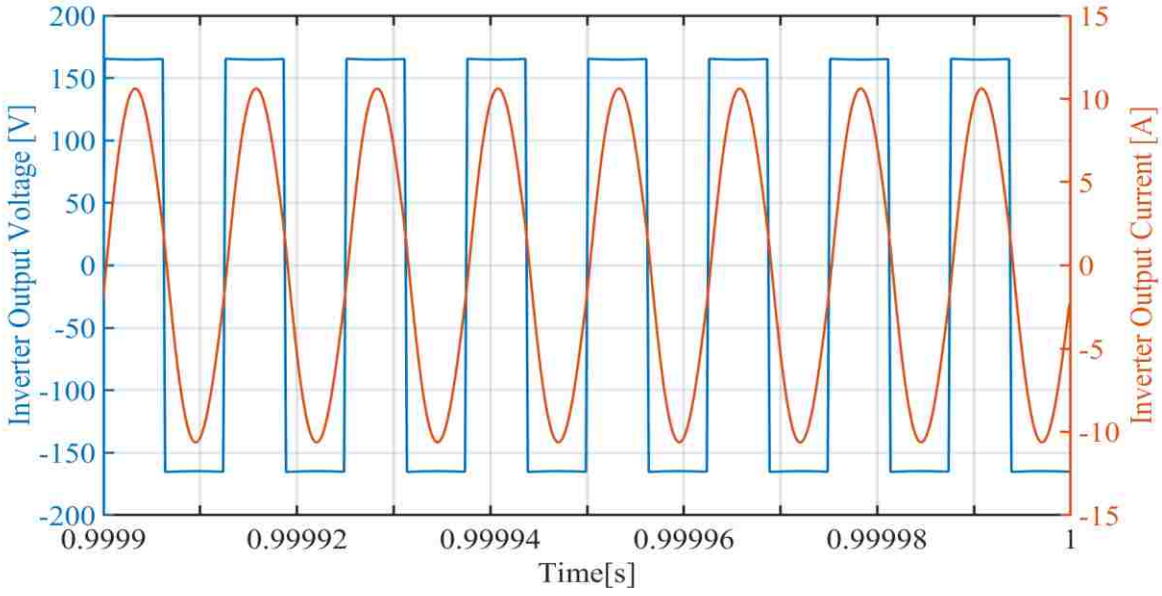

(b)

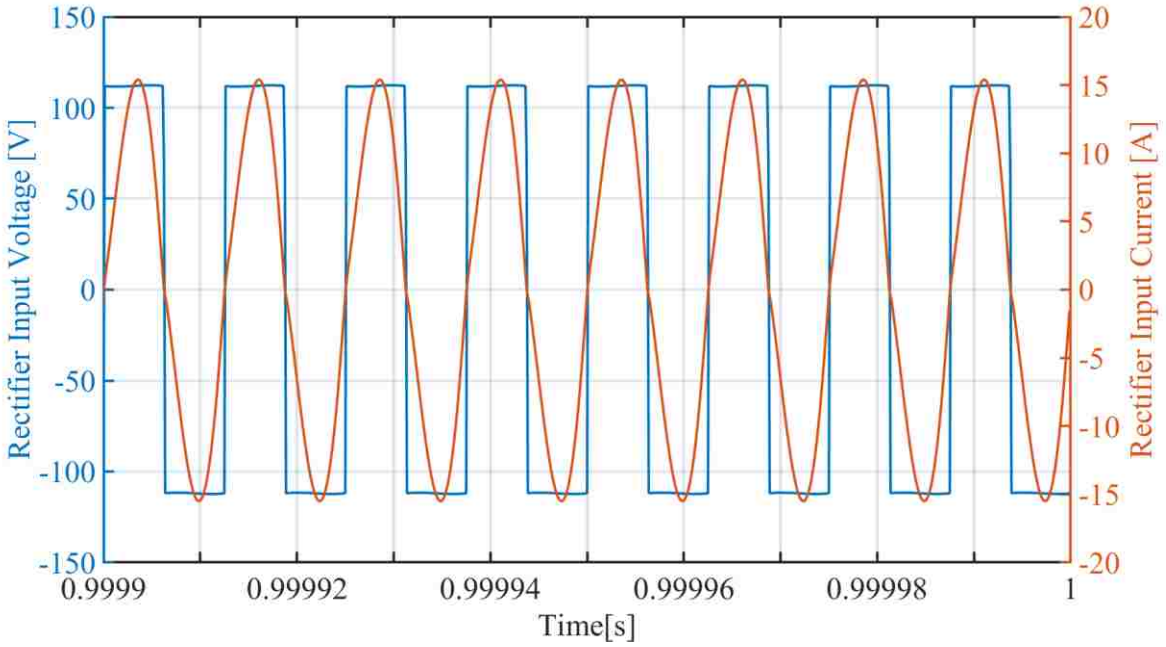

(c)

Simulation results for R=67.5 Ω are illustrated in Figure 8.4.

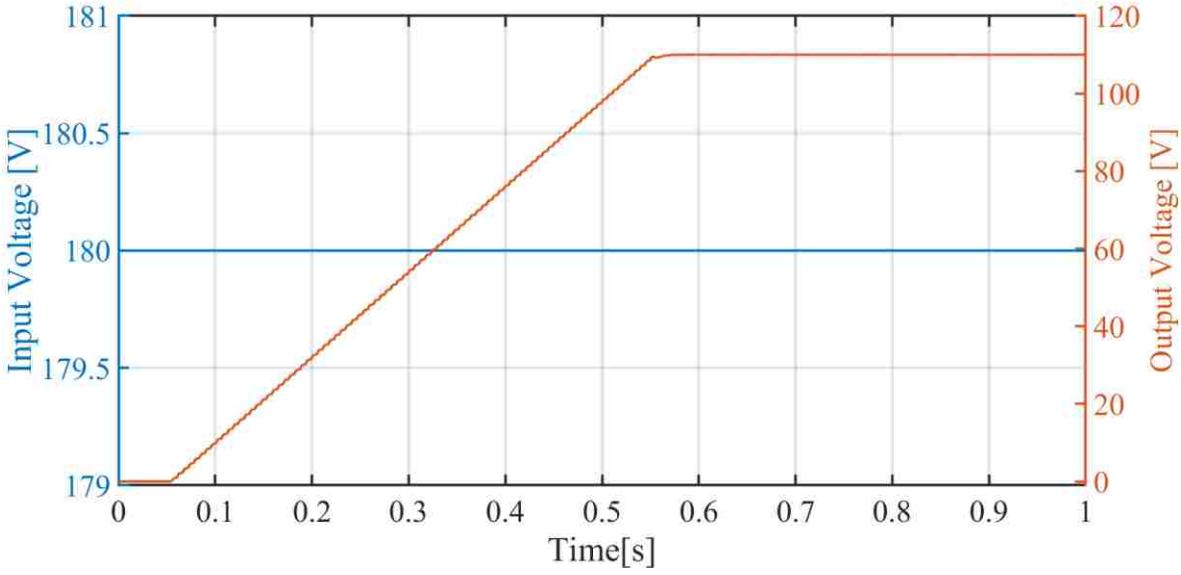

(a)

Figure 8.4. Simulation results for WPT system with secondary LCC compensation when output voltage reference set to 110 V and load is 67.5 Ω (a) input and output voltage (b) HF inverter output voltage and current (d) input voltage and current of rectifier.

(Figure 8.4 continued)

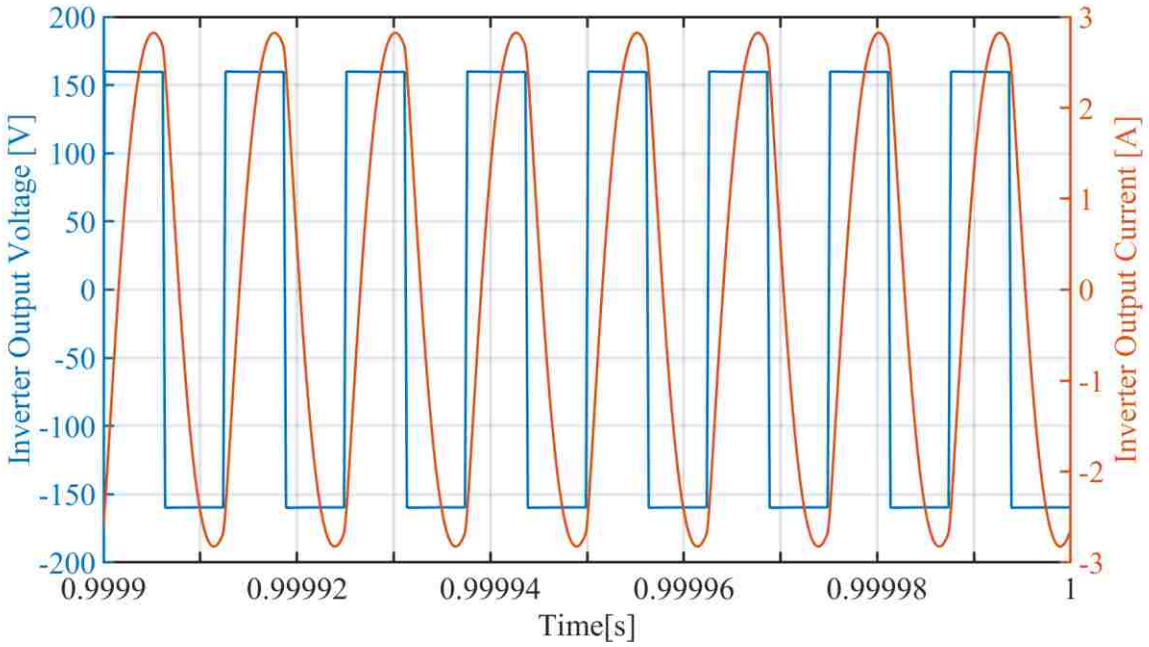

(b)

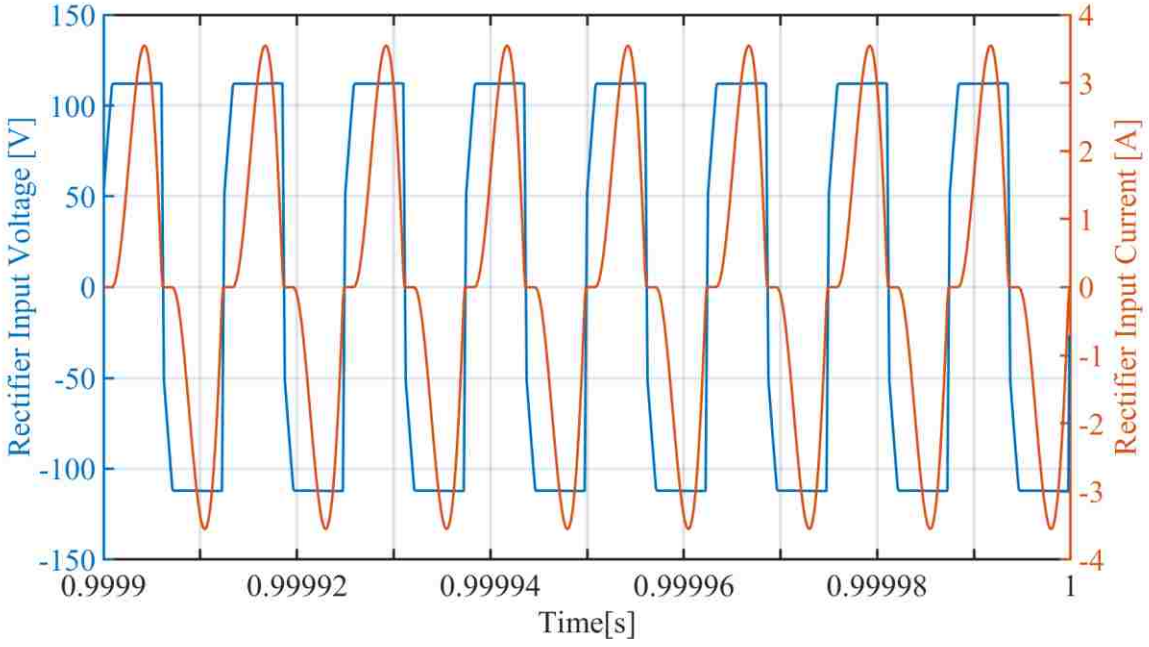

(c)

Simulation results verify that the inverter operates in ZVS mode and VTR is close to the expected value (VTR=112/159.7=0.7), which demonstrates load-independent VTR for the proposed SLCC compensation.

9. EXPERIMENTAL RESULTS AND DISCUSSION

9.1. WPT Setup

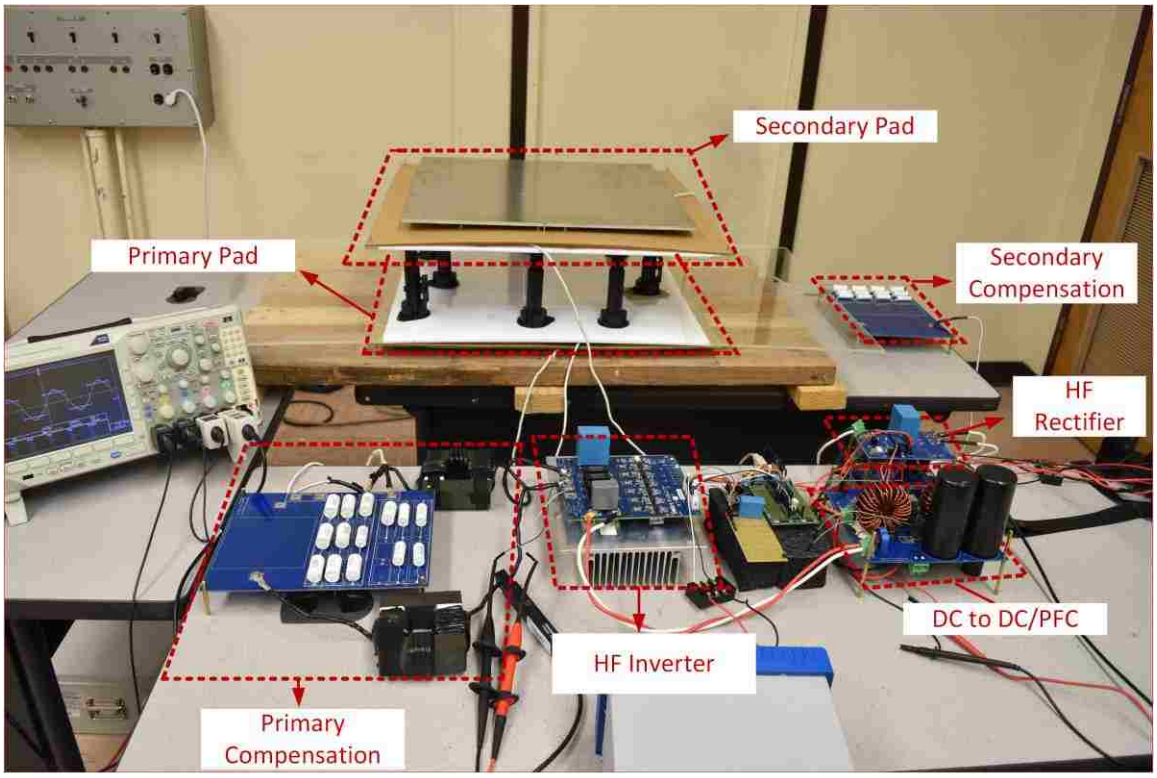

Figure 9.1. 1.2 kW WPT charger system prototype.

Figure 9.1 shows the prototype of a 1.2 kW WPT charger designed and built in the lab. A 5 kW DC power supply (SGA 600/8) is used as the power supply of the system. A buck-boost converter is designed and is used to control the input voltage of the inverter and the load voltage and current. The specifications of the DC/DC converter is listed in Table 7.3. Switching frequency of the converter is 80 kHz. SiC MOSFETs from Cree/Wolfspeed (C3M0065100K) are used in the DC/ DC converter. The gate driver used for SiC switches is from Infineon, which has DESAT protection. For inductor core, Kool Mμ 77620 from Magnetics Inc. is chosen. This core features low loss for low ripple currents and good permeability versus DC bias characteristics. To control the buck-boost converter, TMDSCNCD28335 control card is used. For control as well as

protection purposes, three sensors for the input and output currents and the output voltage are used in the converter. The currents are measured with LEM sensors. To measure the output voltage, a voltage divider is used. To provide isolation for measurements, optically isolated amplifier (ACPL-790B-300E) is employed.

Output of the DC/DC converter is connected to an HF inverter. The full-bridge inverter is controlled by phase-shift method and duty cycle of each switch is 50%. Also, a phase shift ($0 \le \theta \le \pi$) between the command signal for switches of each leg is defined and used to control the amplitude of the amplitude of the inverter's fundamental voltage. Figure 9.2 shows the output voltage of the inverter under phase-shift control method. Peak amplitude of the inverter output can be obtained from the following equation

$$V_{coil-pk} = V_{DC} \frac{4}{\pi} \sin(\frac{\theta}{2}) . \qquad (9-1)$$

To achieve maximum voltage, phase angle is set to π.

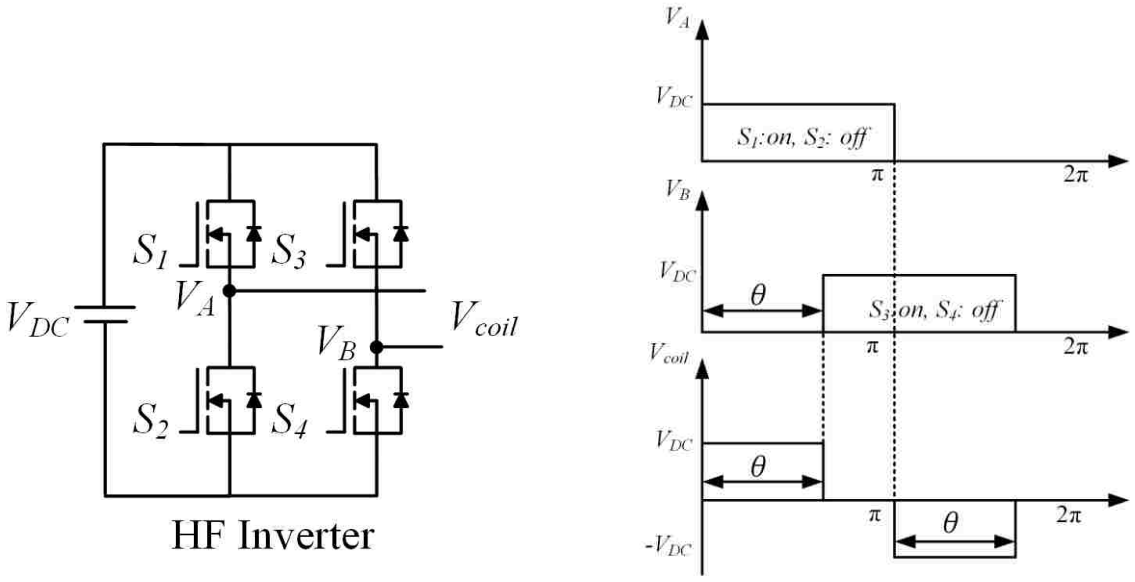

(a) (b)

Figure 9.2. HF inverter (a) schematic (b) output voltage

HF inverter is a six-pack (three-phase) module from Wolfspeed/Cree (CCS050M12CM2) with specifications listed in Table 7.2. To reduce the DC-link voltage ripple, a 20 µF film capacitor is used. Output of the inverter is connected to the primary compensation network and output of the compensation network is connected to the primary coil. The secondary coil is connected to the secondary compensation network. In PLCC and SLCC compensation network topologies, compensation networks consist of capacitors and inductors. Film capacitors from Cornell Dubilier (942C series) are used in compensation networks. The maximum rms voltage of capacitors is 500 V and their rms currents are variable based on their value. To increase the level of voltage and current, the capacitors are connected in series and/or parallel. Dissipation factor (DF) of capacitors is available in their datasheet.

To build the inductors of the compensation network, N87 ferrite is employed. N87 has low power loss density in high frequencies and therefore, has low core loss. To reduce conduction loss of the inductors, Litz wire is used for windings. A problem of ferrite cores is their low saturation flux density. To avoid saturation, providing an airgap in core is mandatory. However, having a large airgap will reduce permeability of the core. Thus, the airgap length should be selected carefully to achieve required inductance and avoid saturation in the core. The design of inductor is carried out in Ansys Maxwell and airgap length is set to 8 mm.

To verify the proposed coil design procedure, three coils were built. Two of them have 25 turns and the third one has 14 turns. The other specifications of coils are the same as those listed in Table 4.1. The ferrite bars are of N87 kind and their structure is the same for both 25 and 14 turns coils. Figure 4.6 depicts the built coils and the ferrite plane. An aluminum plate with thickness of 6 mm is used at back of pads to shield the flux.

Output of the secondary compensation network is connected to the HF rectifier. The full-bridge rectifier consists of four fast recovery diodes (APT60D40BG). A 20 µF film capacitor is connected to output of the rectifier. For constant current and constant voltage charging of the battery, output voltage and current of the rectifier are measured. These quantities are sent to the DC/DC converter. The converter is controlled such that the desired voltage and current are regulated at its output.

9.2. WPT for Constant Load

To verify the proposed coil and compensation networks design, WPT system is connected to constant loads. 2000 W resistors from TE are employed to form the required output loads. Two loads, namely, 11.5 Ω (formed by two parallel 23Ω resistors) and 67.5 Ω (formed by three series 23Ω resistor) are used in the experimental tests. In the first test, a WPT system that has 25 turns coils both in the primary and the secondary is used and compensated with PLCC network. The input voltage is 150 V, the output voltage is set to 60 V and the output resistor is 11.5 Ω. Figure 9.3 depicts the input voltage and current, the inverter output voltage and current and the output voltage and current.

As it can be seen from Figure 9.3 (b), the inverter current is lagging the voltage, which demonstrates ZVS operation. Output voltage shows low ripple which confirms load-independent VTR of the system as well as effective closed-loop control of the DC/DC converter. Based on the input current and voltage and the output voltage and current values measured by digital multimeter (DMM), efficiency of the WPT system is calculated.

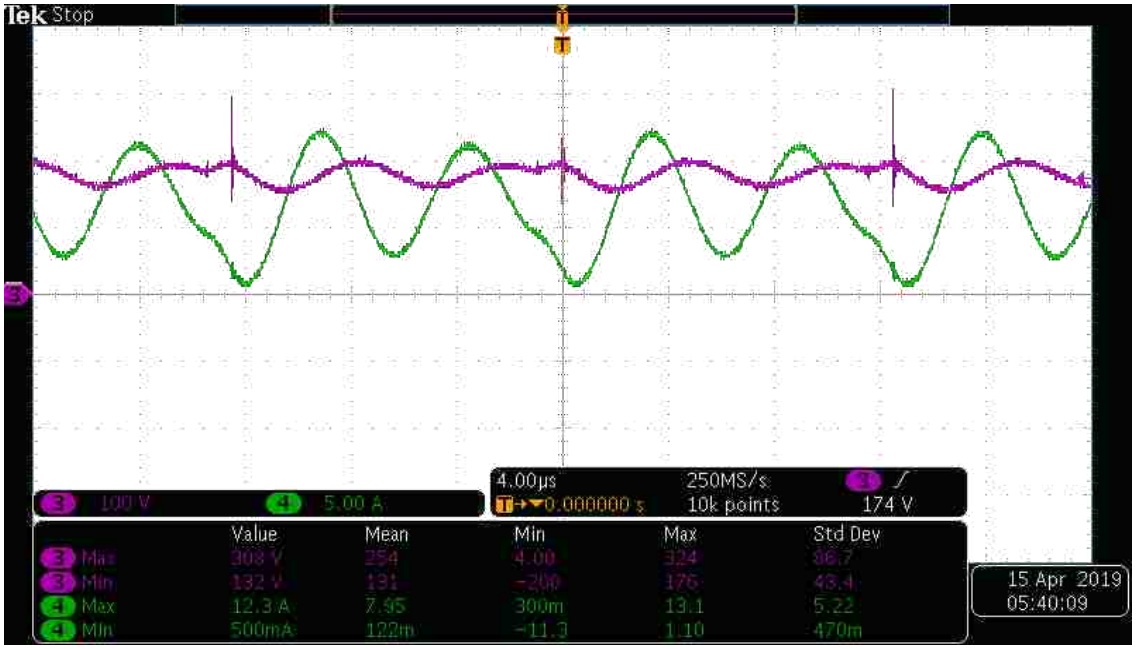

(a)

Figure 9.3. Experimental results for WPT system (25 turns primary and 25 turns secondary) with primary LCC compensation when output voltage reference set to 60 V and load is 11.5 Ω (a) input voltage and current (b) HF inverter output voltage and current (d) output voltage and current.

(b)

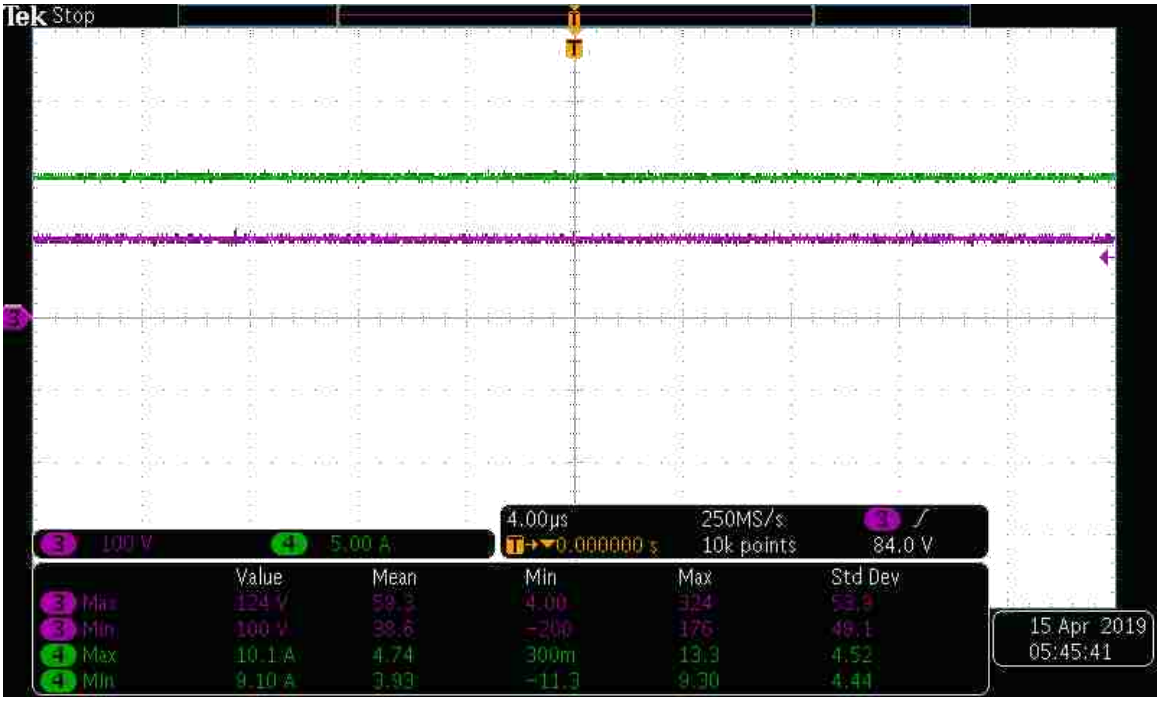

(c)

Table 9.1 shows efficiency of WPT system for all tests. Similar tests are carried out for 67.5 Ω load and results are shown in Figure 9.4. As it can be seen, ZVS operation is maintained for this load. Also, comparing the inverters output voltage and the load voltage levels in both tests, one can see that VTR is almost constant. A slightly higher value of VTR in higher load is due to less voltage drop at lower output power. This shows load-independent VTR characteristics of the system. Based on Table 9.1, when turn number of both the primary and secondary coils are 25, the system efficiency for 67.5 Ω load is more than that for the 11.5 Ω load.

In the next scenario, WPT system with PLCC compensation and primary coil with 25 turns and secondary coil with 14 turns is tested (see Figure 9.5 and Figure 9.6). As it can be seen, for both 11.5 Ω and 67.5 Ω loads, the inverter operates in ZVS mode. Efficiencies of this system in Table 9.1 show that the system has higher efficiency in lower loads compared to the previous system (with 25 primary turns to 25 secondary turns). This is while in higher loads, the previous system has higher efficiency. However, since the output power is higher in low loads, the obtained results

suggest that the system average efficiency with lower turn number in the secondary should be higher.

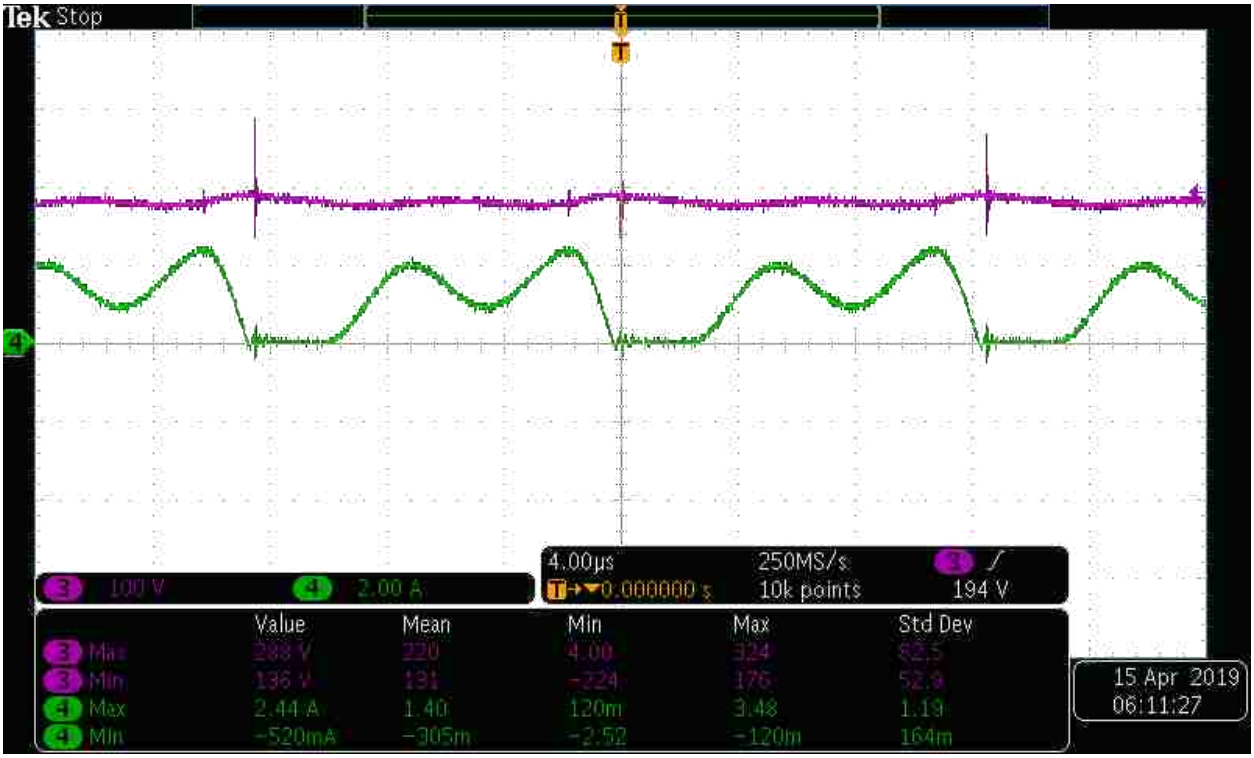

(a)

Figure 9.4. Experimental results for WPT system (25 turns primary and 25 turns secondary) with primary LCC compensation when output voltage reference set to 60 V and load is 67.5 Ω (a) input voltage and current (b) HF inverter output voltage and current (d) output voltage and current.

(Figure 9.4 continued)


Tek Stop
4.00µs 250MS/s
10k points
84.0 V
100 V
2.00 A
Value Mean Min Max Std Dev
Max 224 V 161 4.00 324 99.2
Min -224 V -143 -224 176 83.9
Max 2.36 A 2.36 2.36 2.36 0.00
Min -2.44 A -2.42 -2.52 -2.36 76.6m
15 Apr 2019
06:07:40

(b)

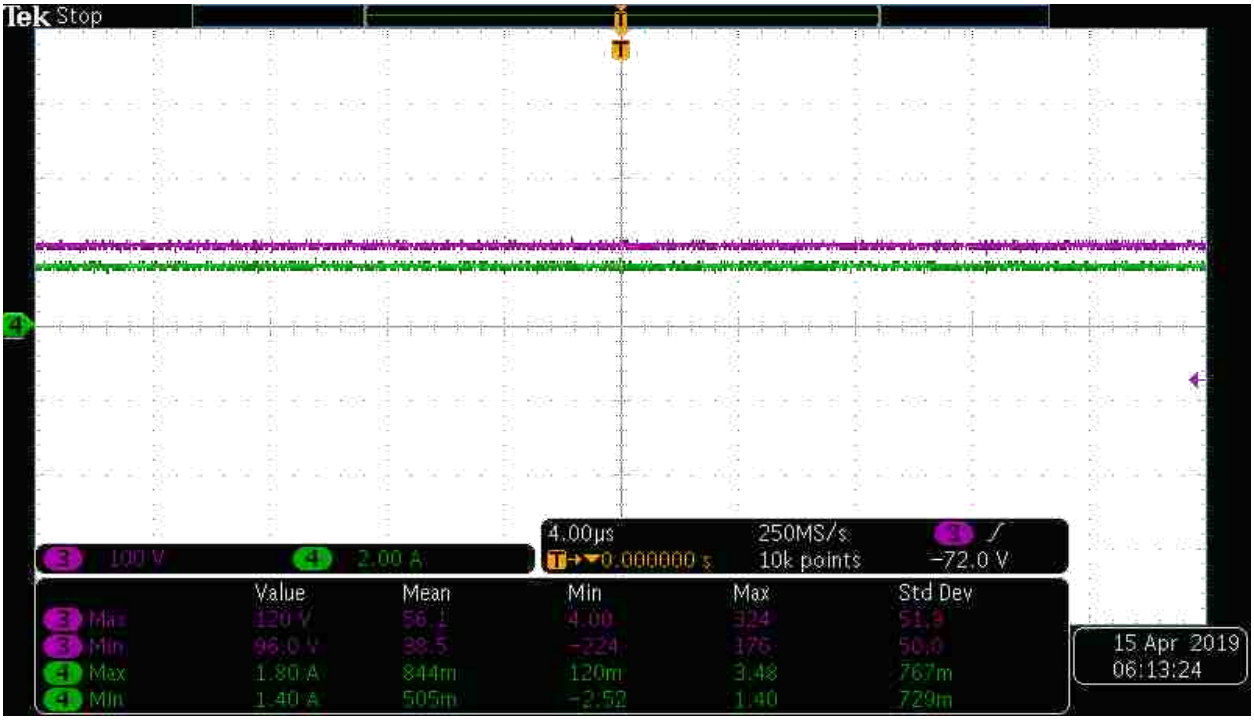
Tek Stop
4.00µs 250MS/s
10k points
-72.0 V
100 V
2.00 A
Value Mean Min Max Std Dev
Max 120 V 56.1 4.00 324 51.9
Min 96.0 V 88.5 -224 176 50.0
Max 1.80 A 844m 120m 3.48 767m
Min 1.40 A 505m -2.52 1.40 729m
15 Apr 2019
06:13:24

(c)

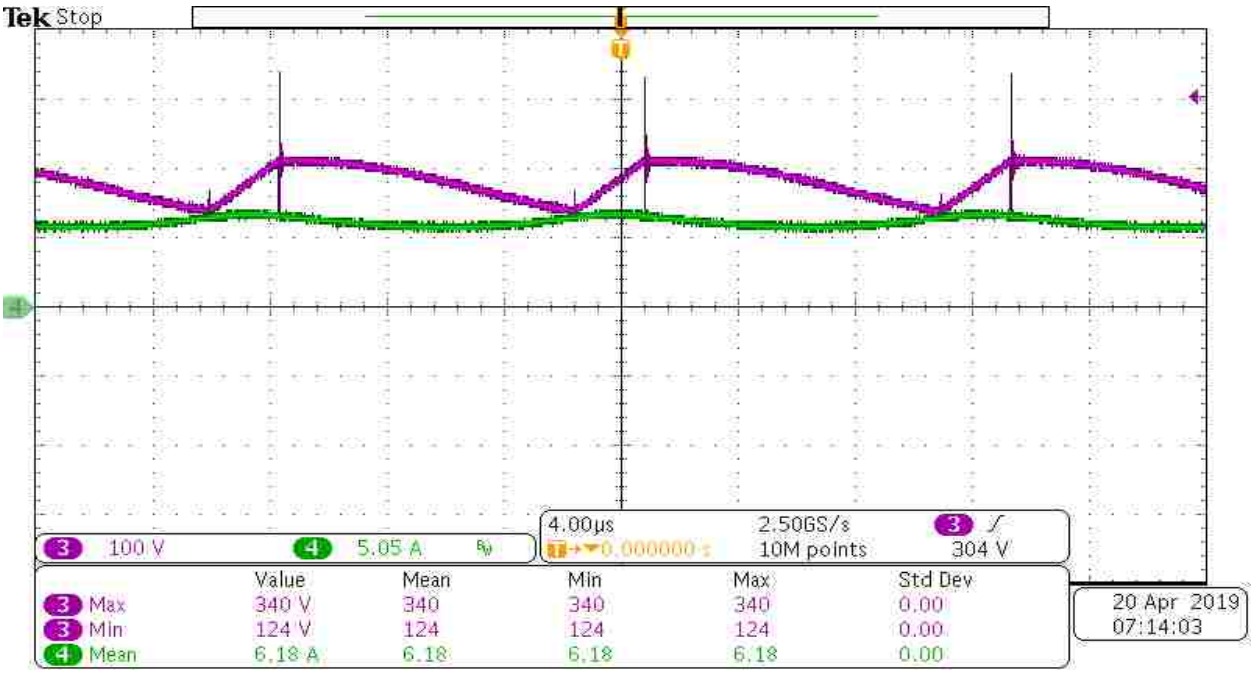

(a)

Figure 9.5. Experimental results for WPT system (25 turns primary and 14 turns secondary) with primary LCC compensation when output voltage reference set to 110 V and load is 11.5 Ω (a) input voltage and current (b) HF inverter output voltage and current (d) output voltage and current.

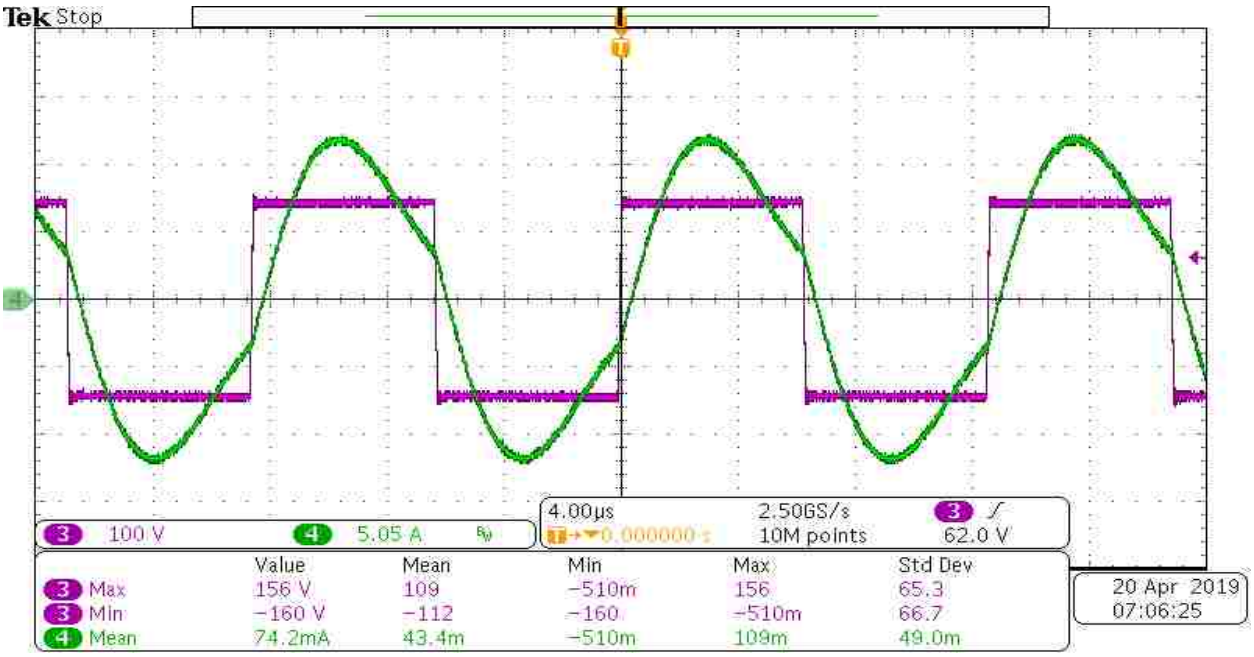

(b)
(Figure 9.5 continued)

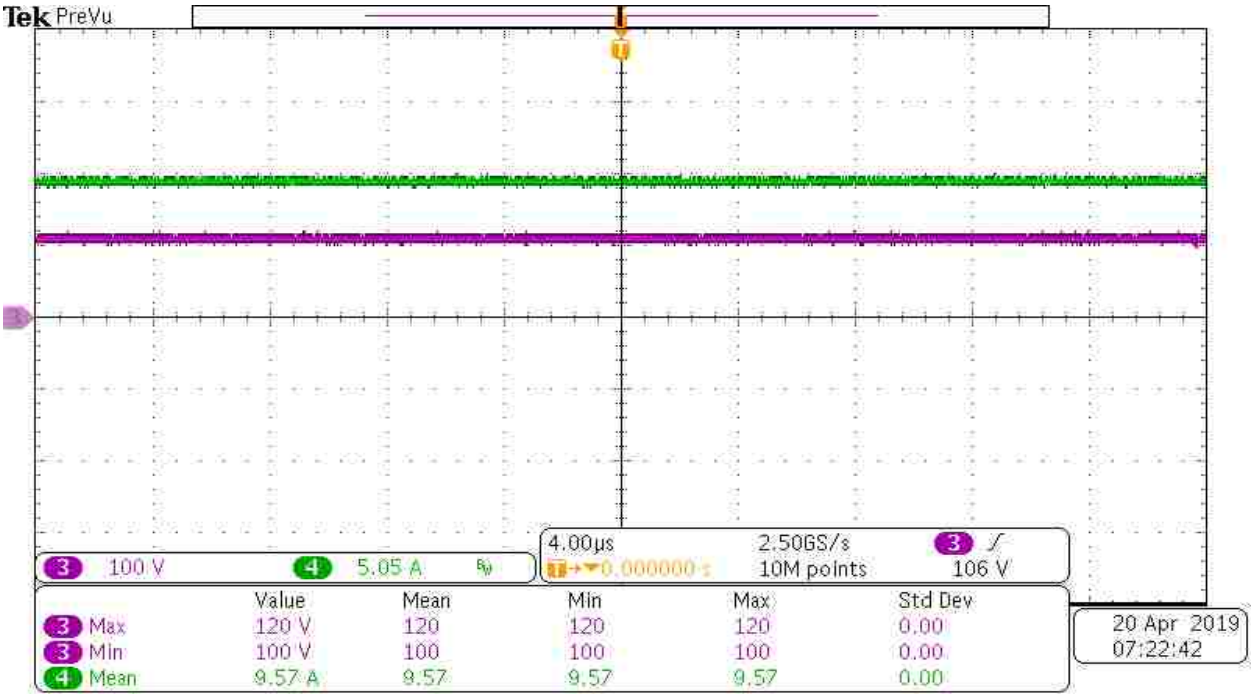

(c)

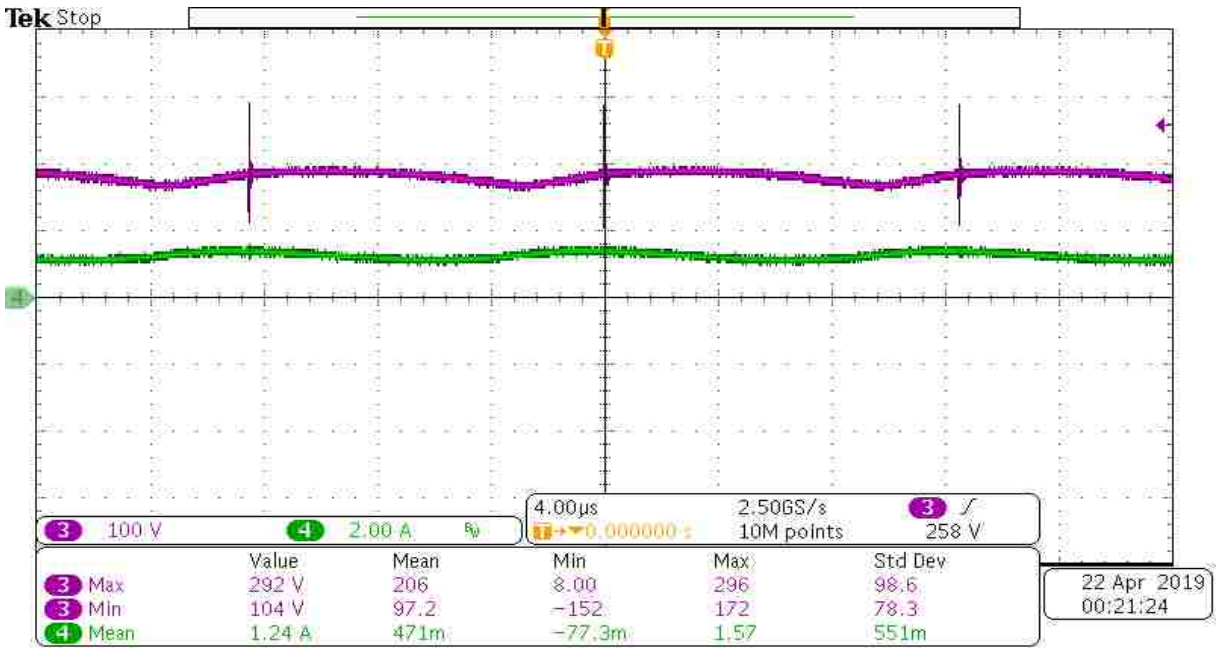

(a)

Figure 9.6. Experimental results for WPT system (25 turns primary and 14 turns secondary) with primary LCC compensation when output voltage reference set to 110 V and load is 67.5 Ω (a) input voltage and current (b) HF inverter output voltage and current (d) output voltage and current.

(Figure 9.6 continued)

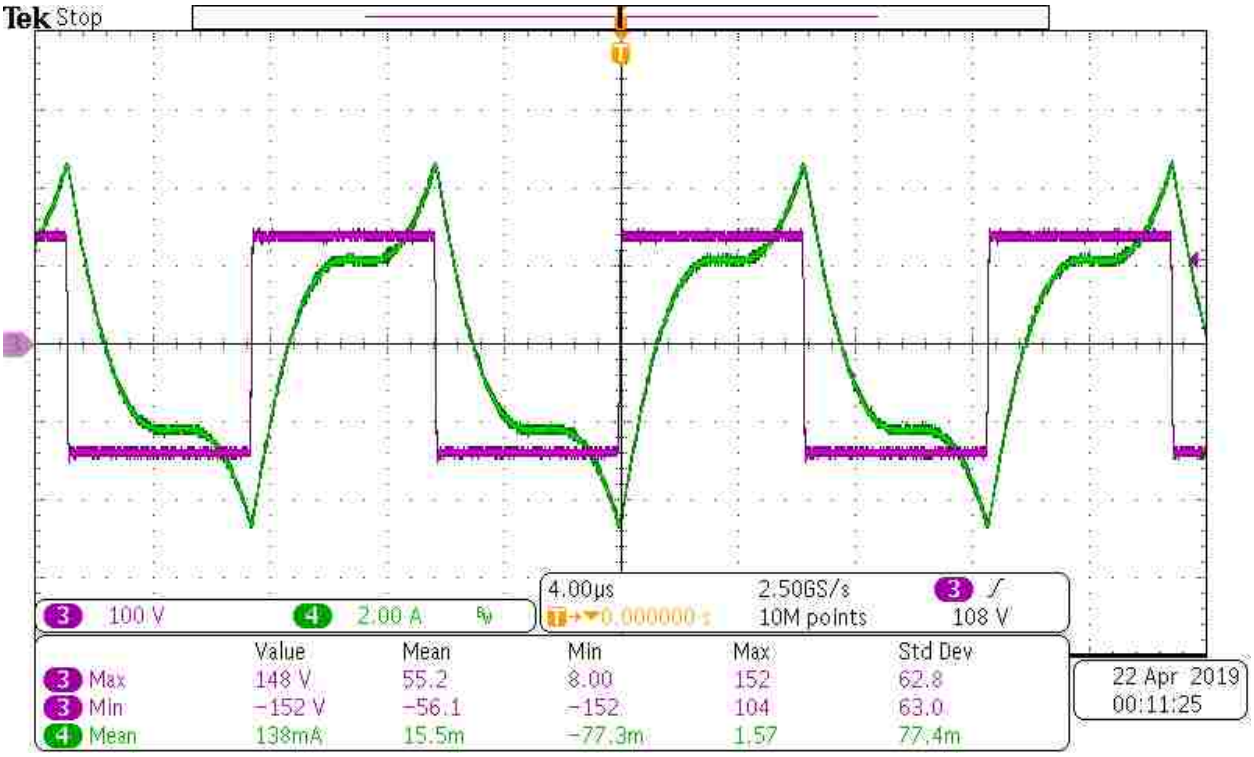
Tek Stop
4.00µs 2.50GS/s
10M points
108 V
3 100 V
4 2.00 A
Value Mean Min Max Std Dev
3 Max 148 V 55.2 8.00 152 62.8
3 Min −152 V −56.1 −152 104 63.0
4 Mean 138mA 15.5m −77.3m 1.57 77.4m
22 Apr 2019
00:11:25

(b)

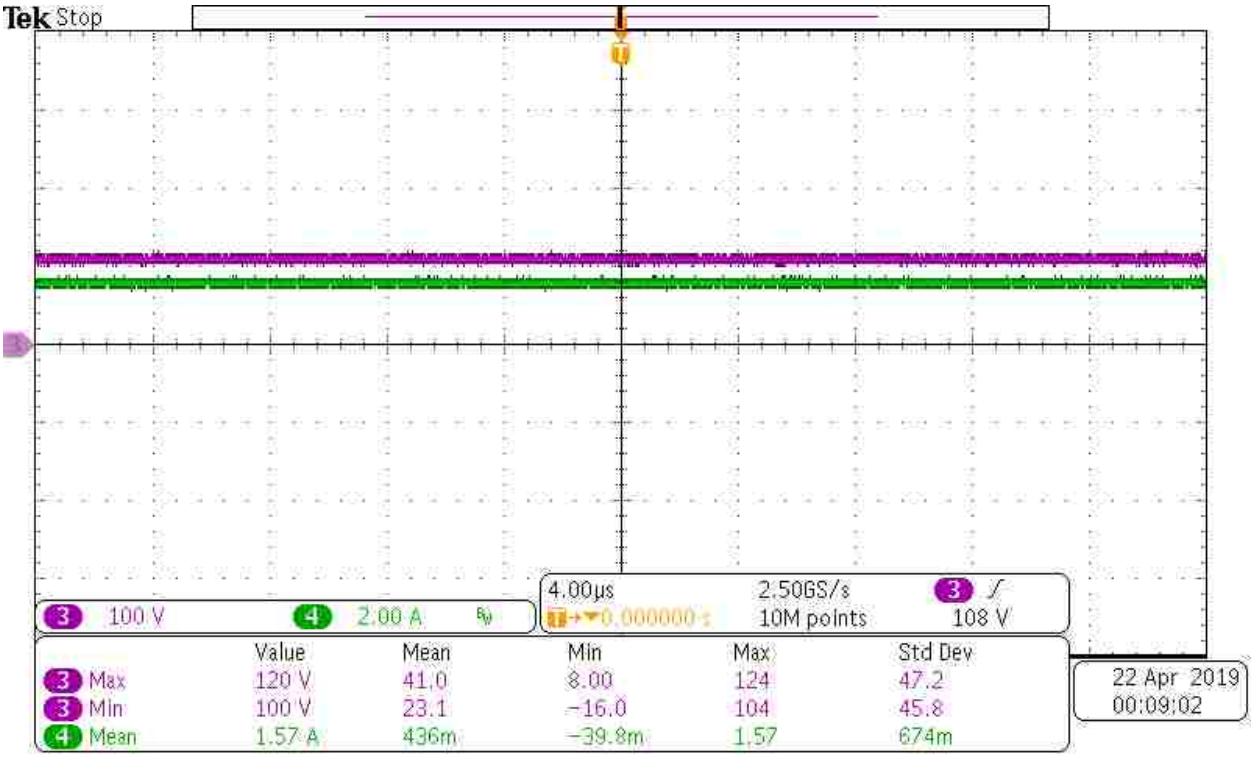
Tek Stop
4.00µs 2.50GS/s
10M points
108 V
3 100 V
4 2.00 A
Value Mean Min Max Std Dev
3 Max 120 V 41.0 8.00 124 47.2
3 Min 100 V 23.1 −16.0 104 45.8
4 Mean 1.57 A 436m −39.8m 1.57 674m
22 Apr 2019
00:09:02

(c)

The next testes are carried out for two WPT systems with SLCC compensation. In the first test, the two coils with 25 turns both in the primary and the secondary are used. In the second test, the primary coil has 14 turns and the secondary coil has 25 turns. The results are shown in Figure 9.7 and Figure 9.11. As it can be seen for both load values (11.5 Ω and 67.5 Ω), the inverter works in ZVS mode. Also, VTR is almost constant and independent of the load value. Considering efficiencies of the two systems, one can conclude that for both low and high load values, WPT with 25 turns both in the primary and the secondary has higher efficiency. This means that for a WPT with SLCC compensation, reduced number of turns in the primary (or in other words, less wire) can lead to low system efficiency.

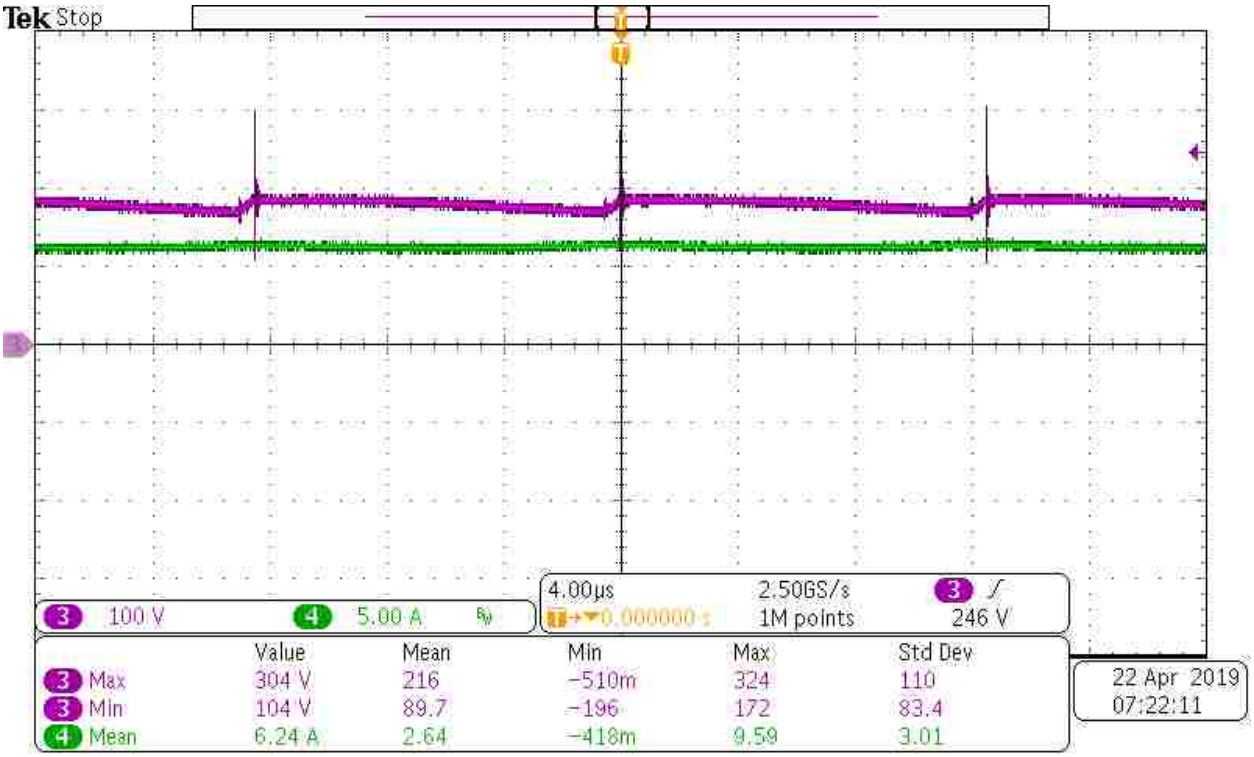

(a)

Figure 9.7. Experimental results for WPT system (25 turns primary and 25 turns secondary) with secondary LCC compensation when output voltage reference set to 110 V and load is 11.5 Ω (a) input voltage and current (b) HF inverter output voltage and current (d) output voltage and current.

(Figure 9.7 continued)

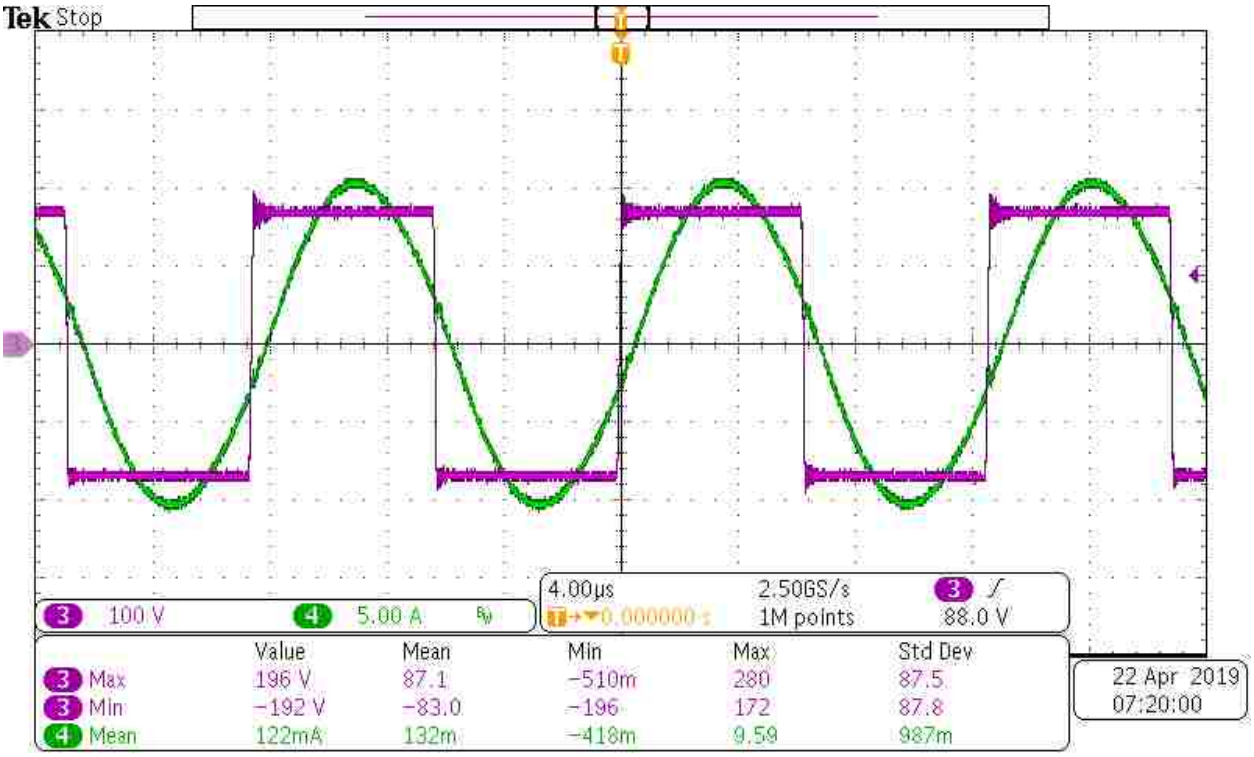
Tek Stop
4.00µs 2.50GS/s
1M points
88.0 V
100 V
5.00 A
Value Mean Min Max Std Dev
Max 196 V 87.1 −510m 280 87.5
Min −192 V −83.0 −196 172 87.8
Mean 122mA 132m −418m 9.59 987m
22 Apr 2019
07:20:00

(b)

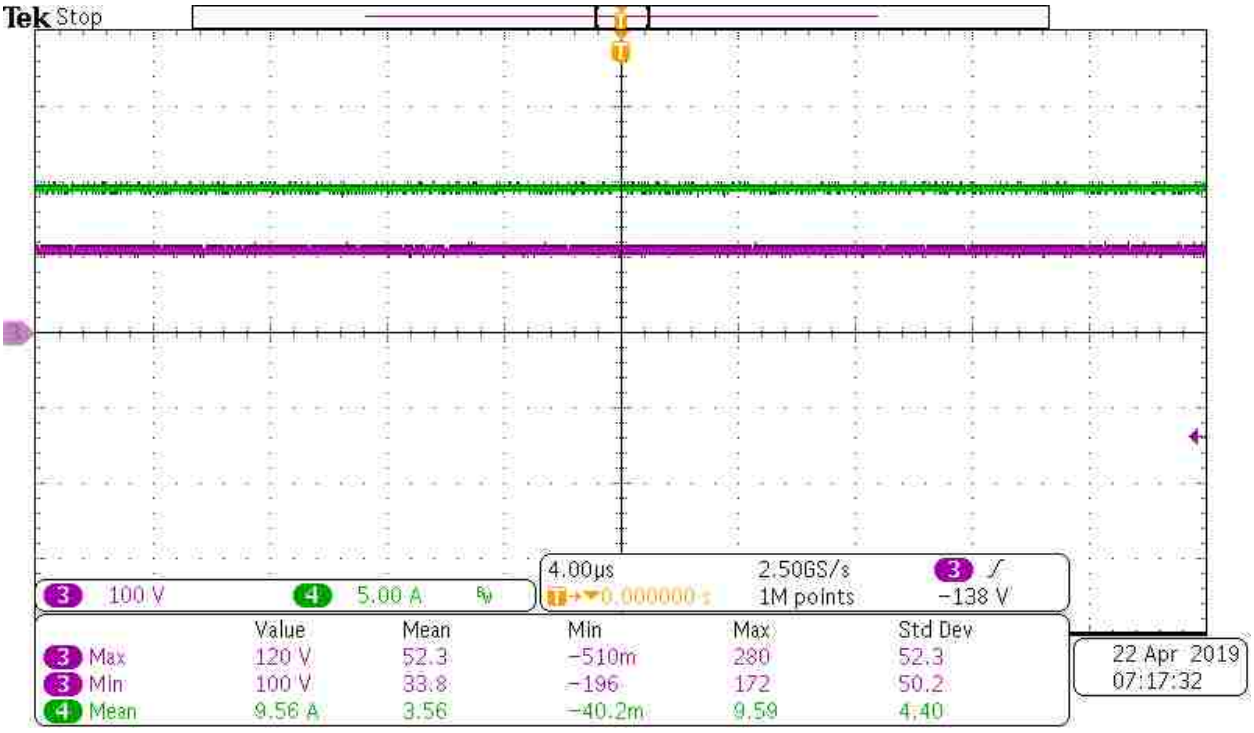
Tek Stop
4.00µs 2.50GS/s
1M points
−138 V
100 V
5.00 A
Value Mean Min Max Std Dev
Max 120 V 52.3 −510m 280 52.3
Min 100 V 33.8 −196 172 50.2
Mean 9.56 A 3.56 −40.2m 9.59 4.40
22 Apr 2019
07:17:32

(c)

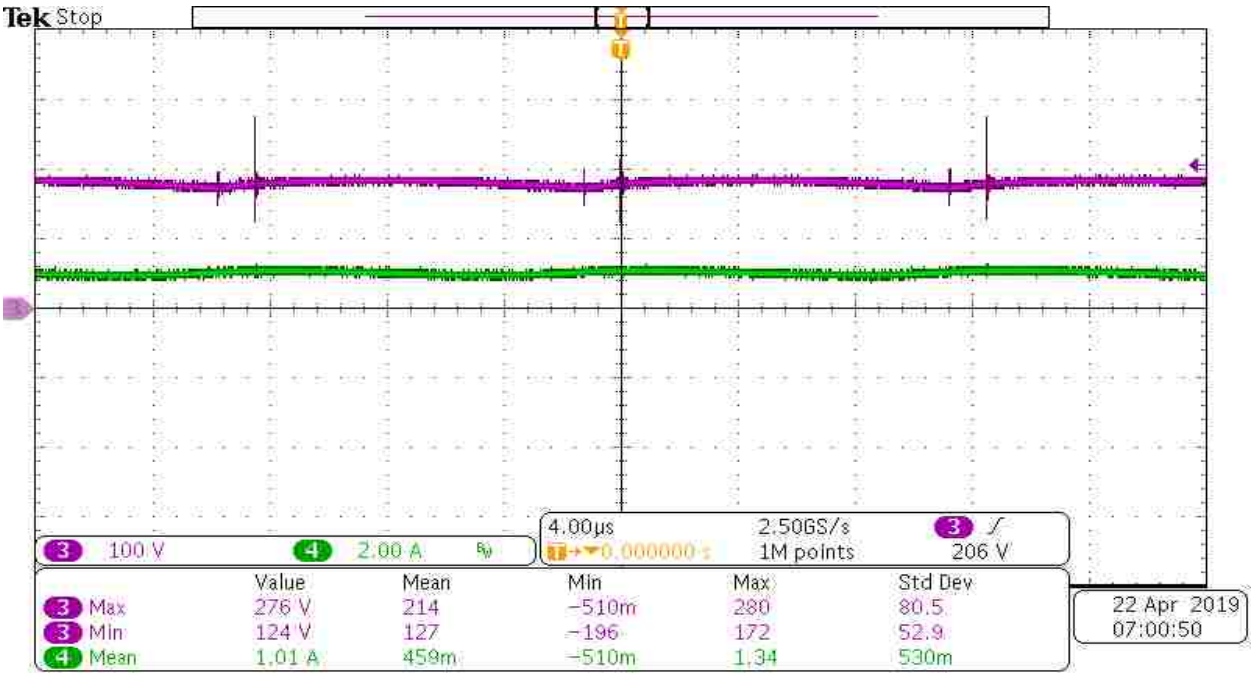

(a)

Figure 9.8. Experimental results for WPT system (25 turns primary and 25 turns secondary) with secondary LCC compensation when output voltage reference set to 110 V and load is 67.5 Ω (a) input voltage and current (b) HF inverter output voltage and current (d) output voltage and current.

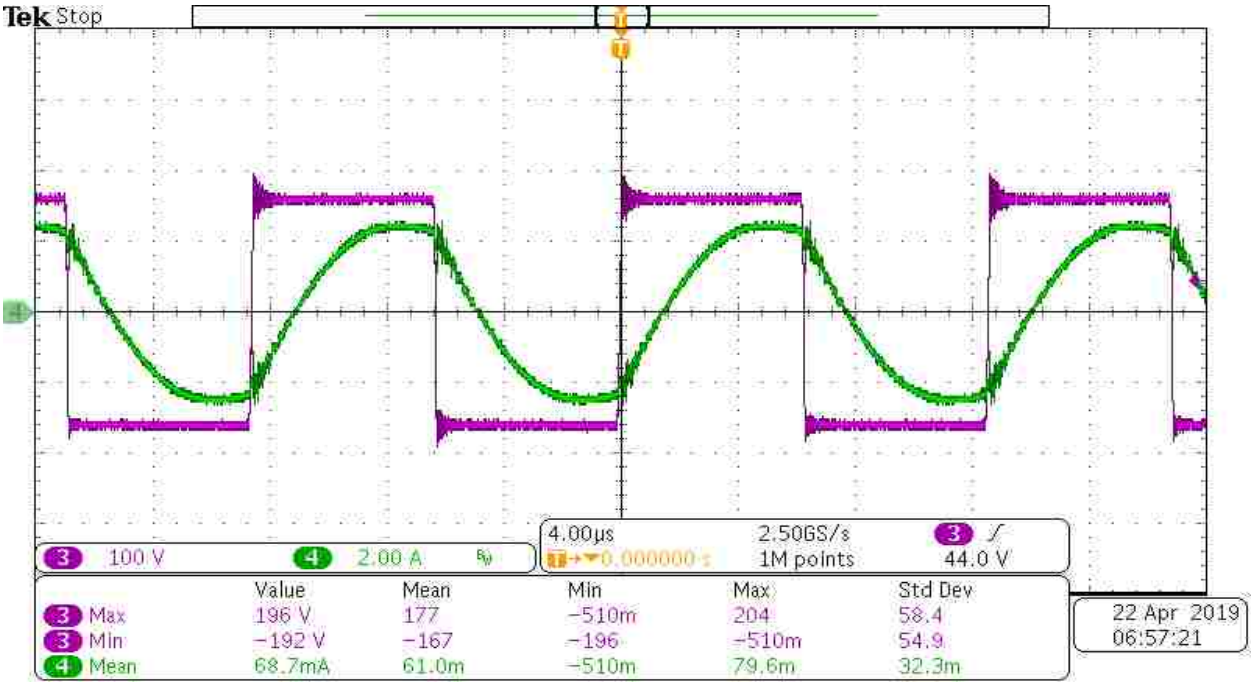

(b)

(Figure 9.8 continued)

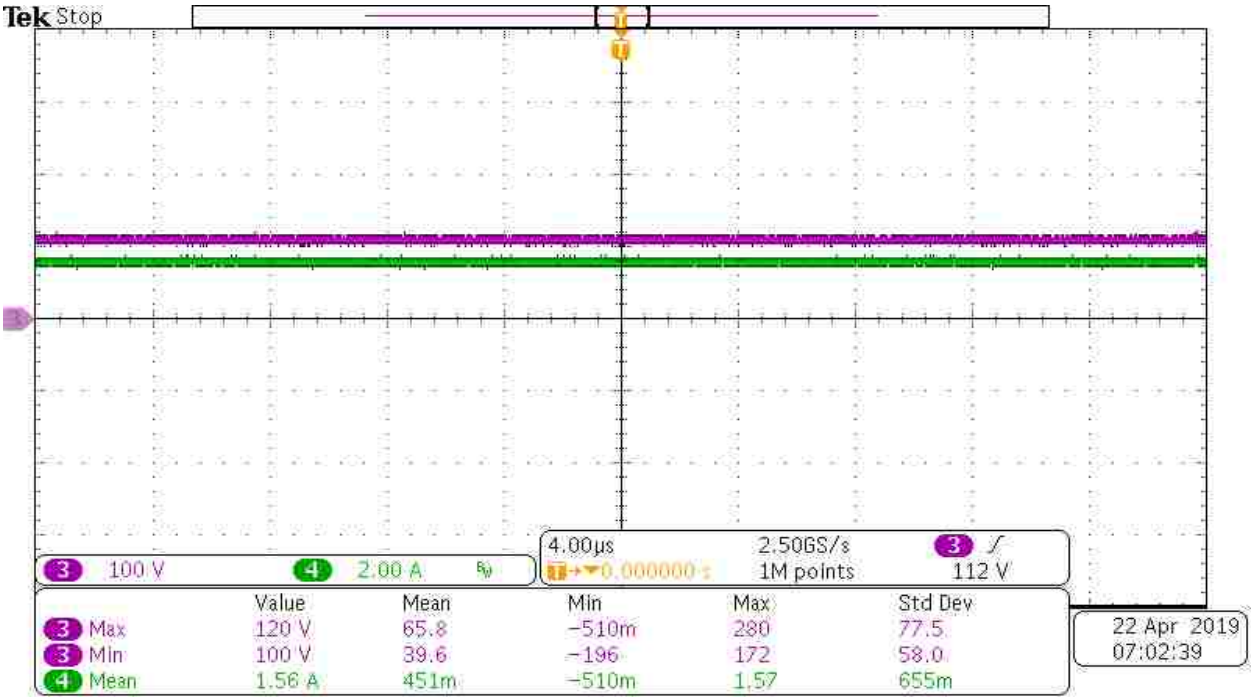

(c)

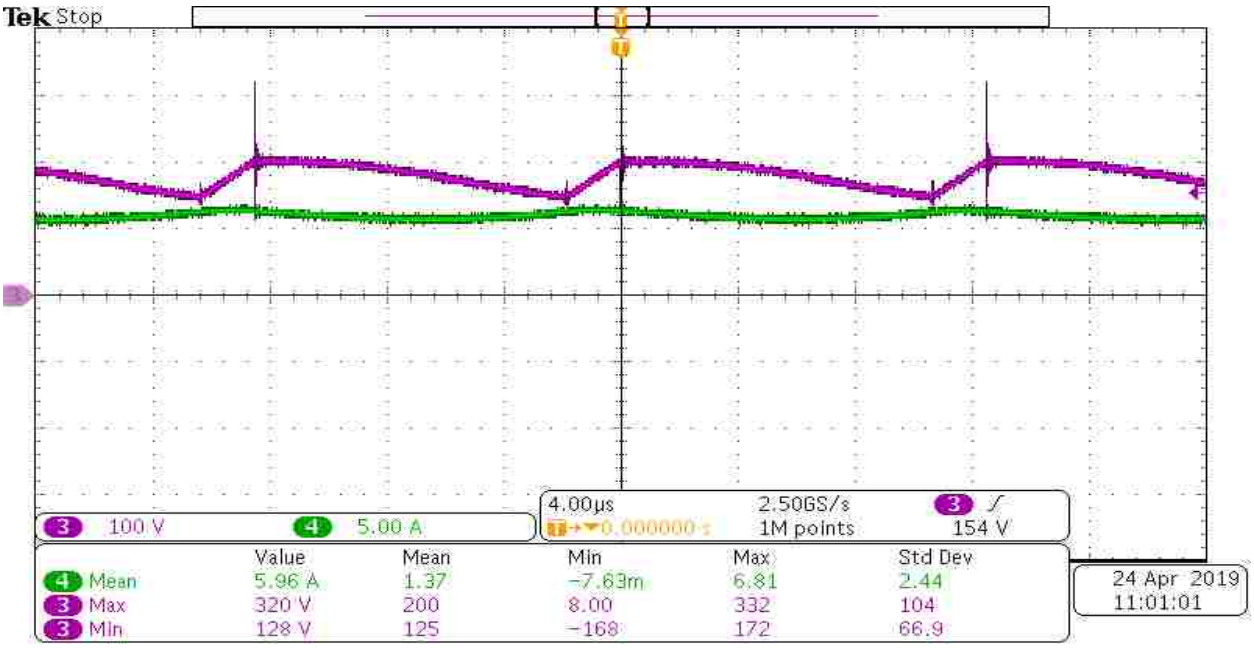

(a)

Figure 9.9. Experimental results for WPT system (14 turns primary and 25 turns secondary) with secondary LCC compensation when output voltage reference set to 110 V and load is 11.5 Ω (a) input voltage and current (b) HF inverter output voltage and current (d) output voltage and current.

(Figure 9.9 continued)

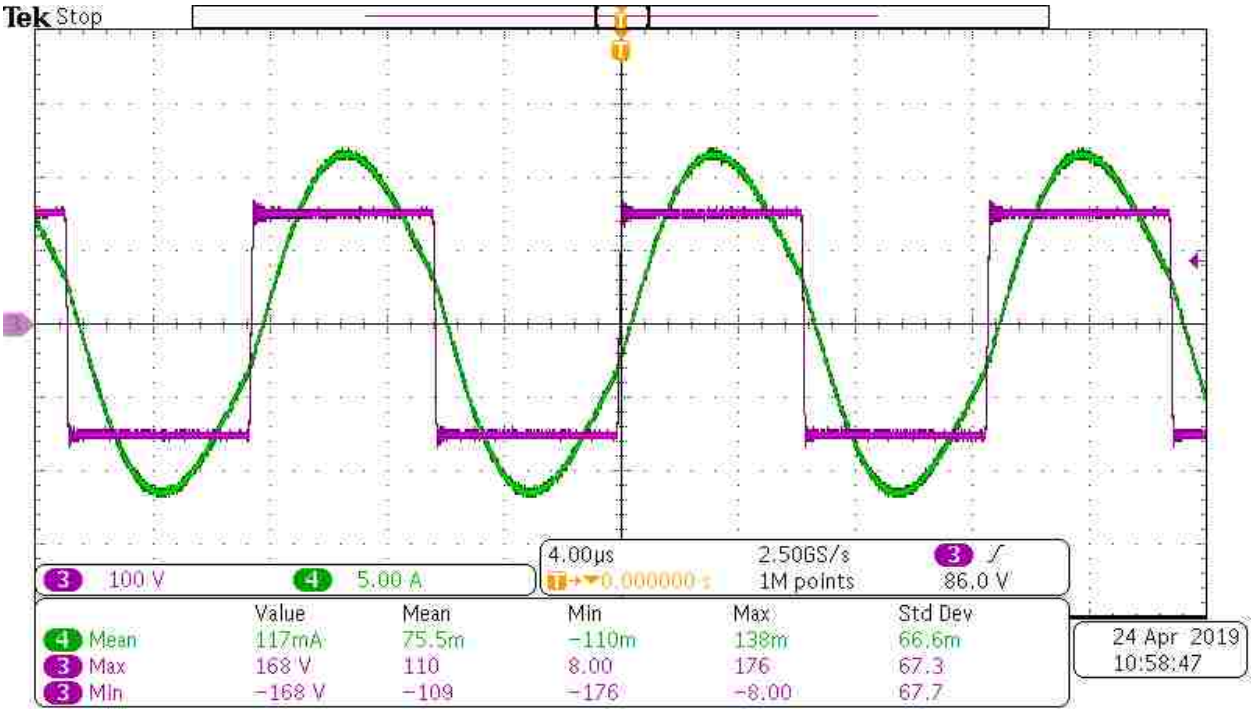
Tek Stop
4.00µs
2.50GS/s
1M points
3 86.0 V
3 100 V
4 5.00 A
Value Mean Min Max Std Dev
4 Mean 117mA 75.5m −110m 138m 66.6m
3 Max 168 V 110 8.00 176 67.3
3 Min −168 V −109 −176 −8.00 67.7
24 Apr 2019
10:58:47

(b)

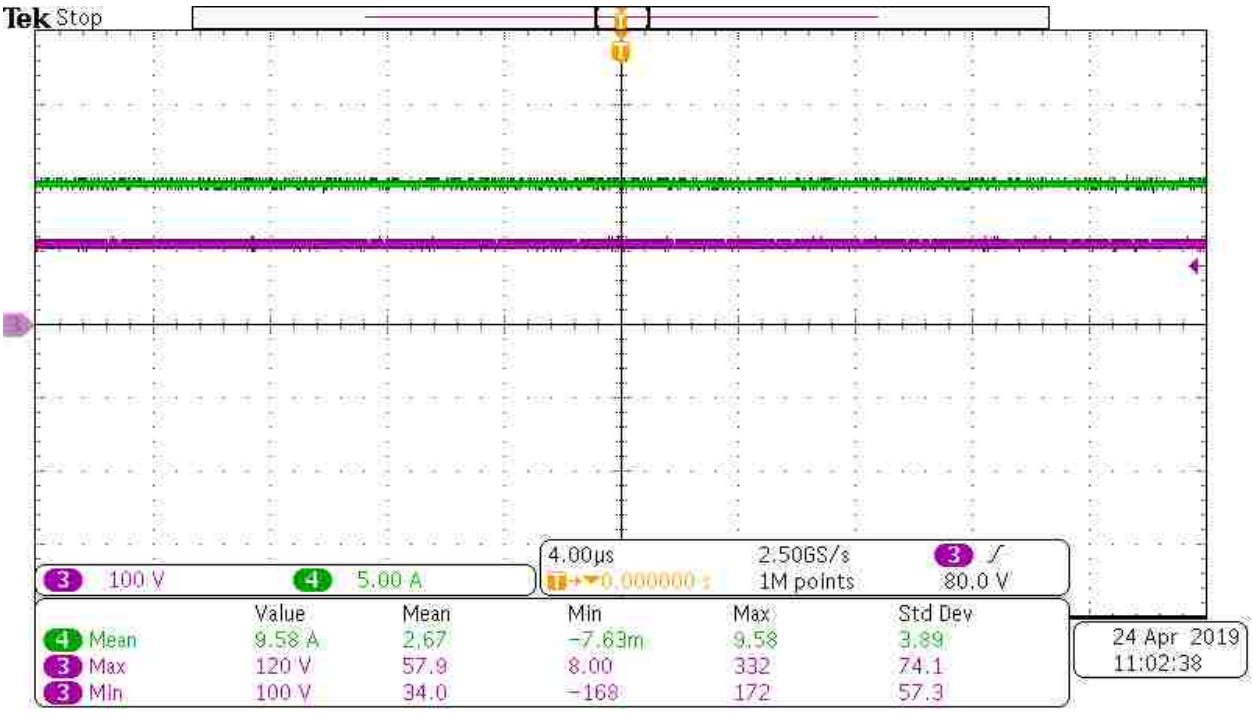
Tek Stop
4.00µs
2.50GS/s
1M points
3 80.0 V
3 100 V
4 5.00 A
Value Mean Min Max Std Dev
4 Mean 9.58 A 2.67 −7.63m 9.58 3.89
3 Max 120 V 57.9 8.00 332 74.1
3 Min 100 V 34.0 −168 172 57.3
24 Apr 2019
11:02:38

(c)

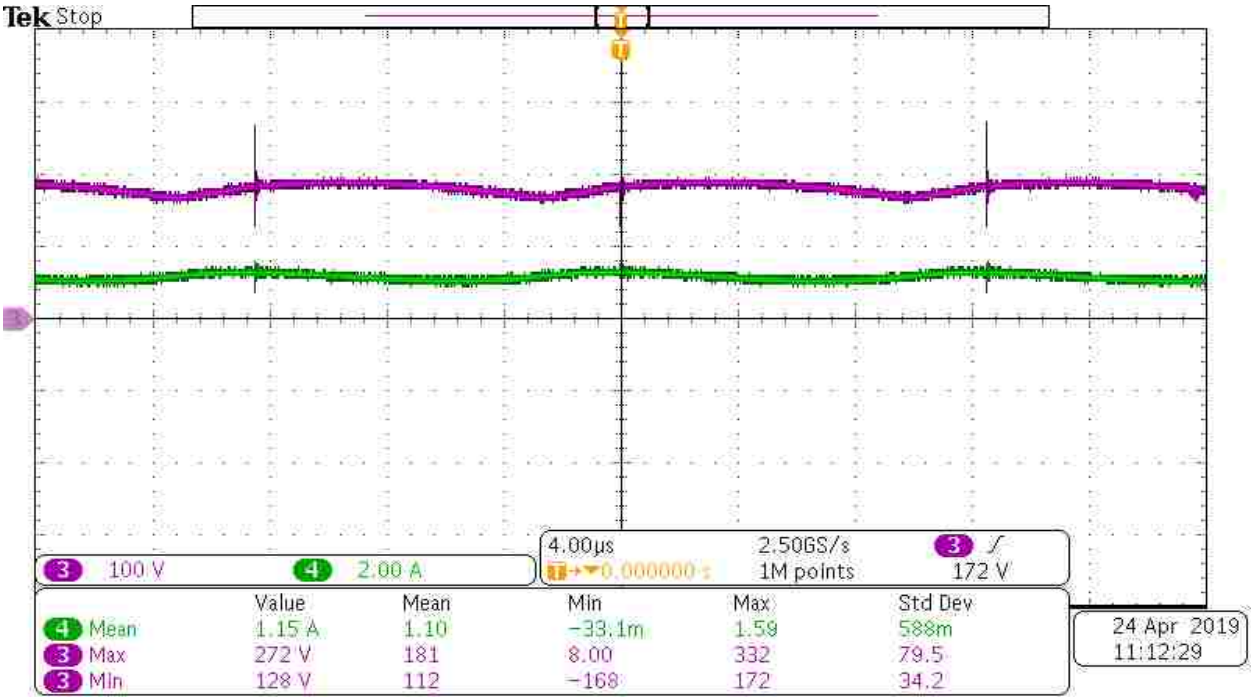

(a)

Figure 9.10. Experimental results for WPT system (14 turns primary and 25 turns secondary) with secondary LCC compensation when output voltage reference set to 60 V and load is 67.5 Ω (a) input voltage and current (b) HF inverter output voltage and current (d) output voltage and current.

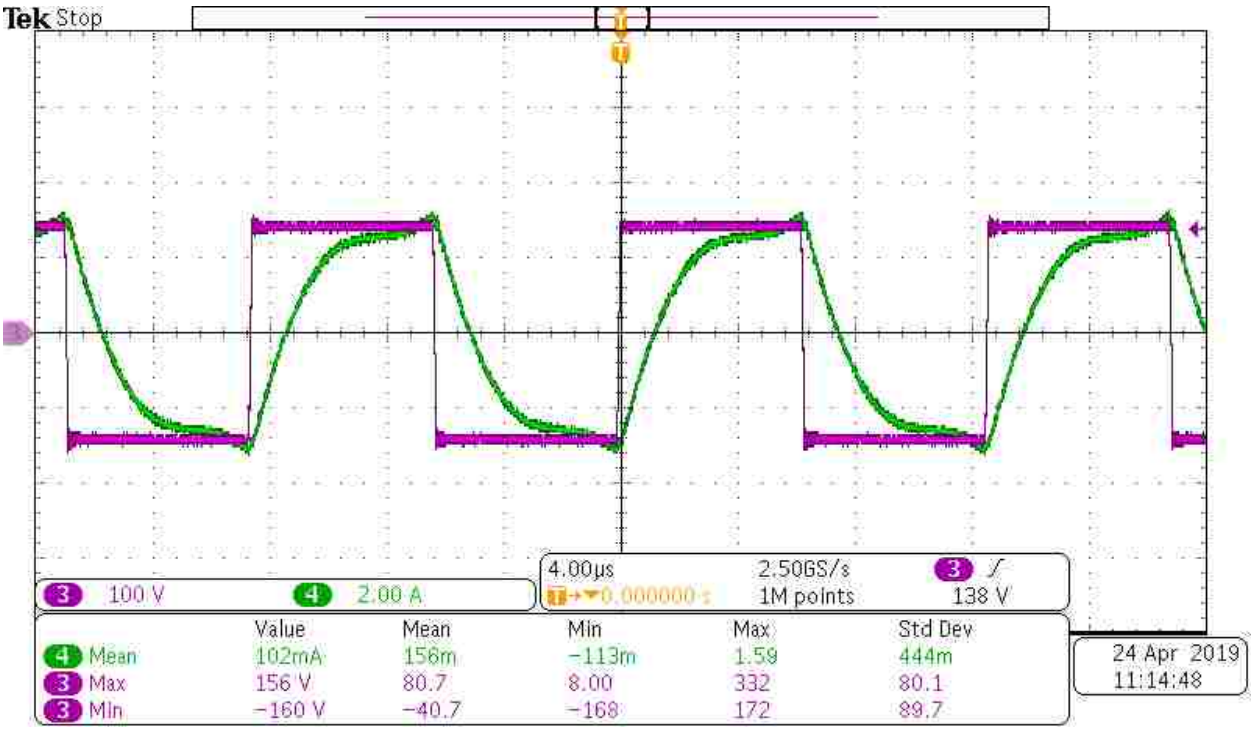

(b)

(Figure 9.10 continued)

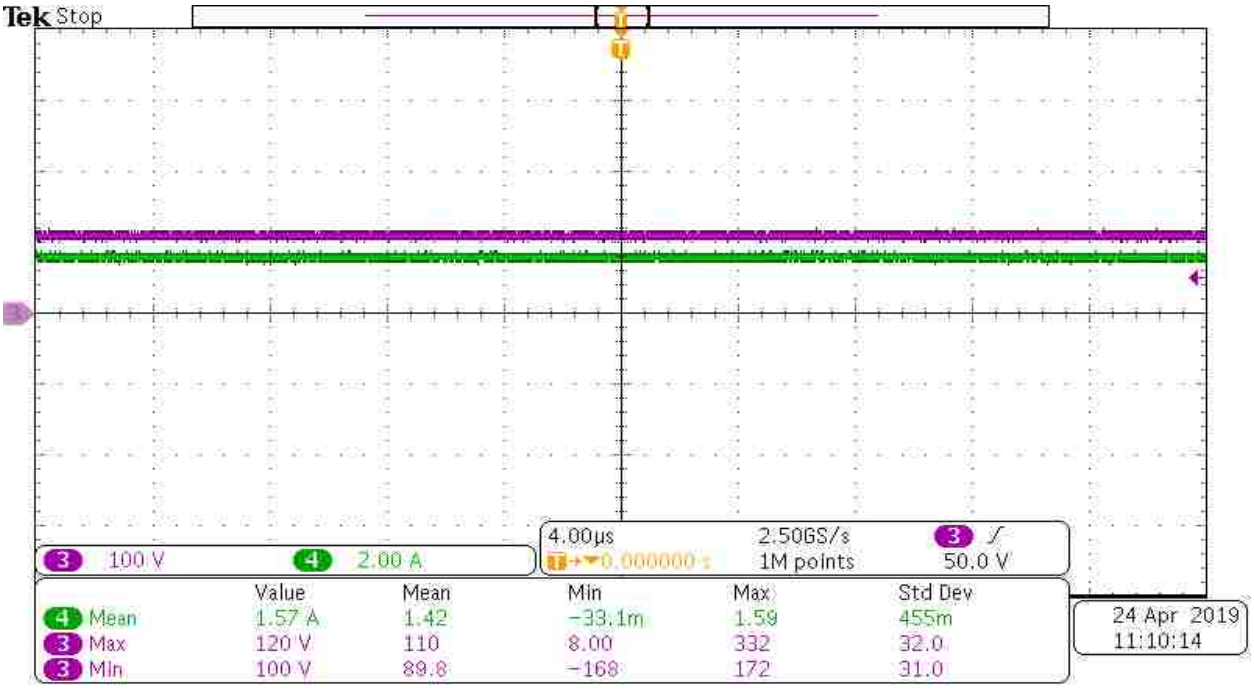

(c)

Table 9.1. WPT systems efficiencies for two constant loads.

Test Description	V_{in} [V]	I_{in} [A]	V_{out} [V]	I_{out} [A]	η_{sys}[%]
PLCC- 25:25 (primary: secondary)- R=11.5Ω	180	6.62	110.85	9.7	90.1
PLCC- 25:25 (primary: secondary)- R=67.5Ω	180	1.13	109.75	1.62	87.4
PLCC- 25:14 (primary: secondary)- R=11.5Ω	180	6.33	109.35	9.55	91.7
PLCC- 25:14 (primary: secondary)- R=67.5Ω	180	1.14	109.64	1.63	87
SLCC- 25:25 (primary: secondary)- R=11.5Ω	180	6.35	109.46	9.57	91.7
SLCC- 25:25 (primary: secondary)- R=67.5Ω	180	1.12	109.82	1.63	88.8
SLCC- 14:25 (primary: secondary)- R=11.5Ω	180	6.41	109.48	9.57	90.8
SLCC- 14:25 (primary: secondary)- R=67.5Ω	180	1.24	109.76	1.63	80.15

9.3. WPT for Charging Battery

To verify the superiority of the proposed coil and compensation network design in improving system average efficiency in comparison to the existing methods, a 2.5 kWh Li-Ion battery is charged by the WPT system. Two WPT systems with primary LCC compensation are tested. In the first case, the primary and the secondary coils have 25 turns. In the second case, the primary coil has 25 turns while the secondary has 14 turns. Figure 9.11 depicts the obtained results for the first case. Figure 9.11 (a) shows the battery's voltage and current waveforms. As it can be seen, the battery is first charged with 9.5 A constant current. The battery voltage increases and when it reaches 111 V, the output voltage is controlled at 111 V. After that, the battery is charged with constant voltage. The current starts to decrease until it reaches 0.2 A. In Figure 9.11 (b), the input and output powers are illustrated. Using these measurements and considering the battery charging time, the input and output energy are calculated. Next, the system average efficiency is obtained based on (7-1). Input and output energy of the system as well as the system average efficiency are shown in Table 9.2.

Table 9.2. WPT systems average efficiencies for 2.5 kWh Li-Ion battery.

Test Description	*Input Energy* [kWh]	*Output Energy* [kWh]	η_{avg} [%]
PLCC- 25:25 (primary: secondary)	2.807	2.511	89.4
PLCC- 25:14 (primary: secondary)	2.878	2.642	91.8
SLCC- 25:25 (primary: secondary)	2.893	2.657	91.84
SLCC- 14:25 (primary: secondary)	2.91	2.627	90.27

Figure 9.12 depicts the obtained results for the second case. As it can be seen, the output voltage and current are very similar to the previous case. However, the difference between the output and

input powers is less. Input and output energies as well as the system average efficiency are shown in Table 9.2. The obtained results verify that the lower number of turns in the secondary coil not only reduces the required material and cost, but also improves the system average efficiency.

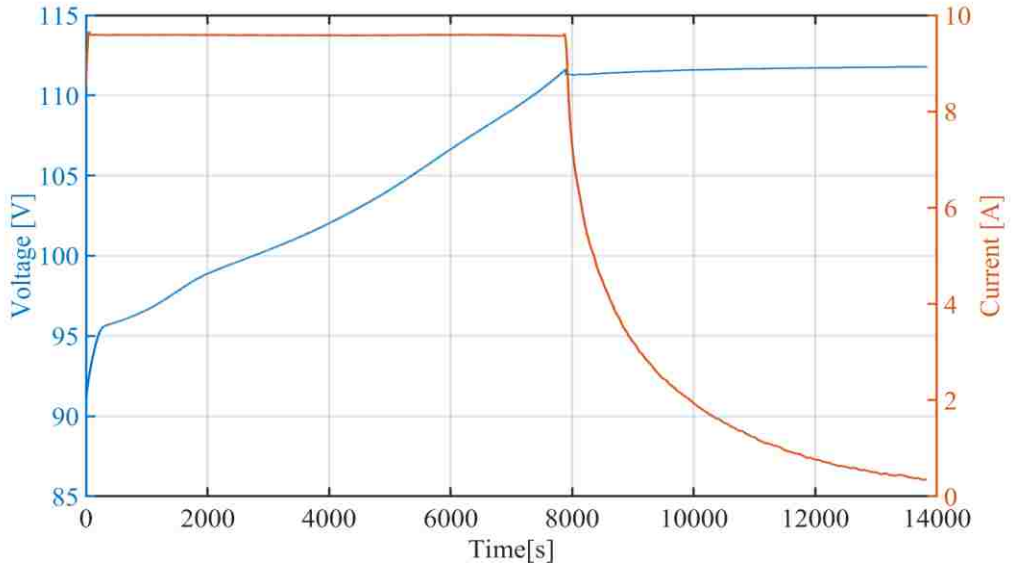

(a)

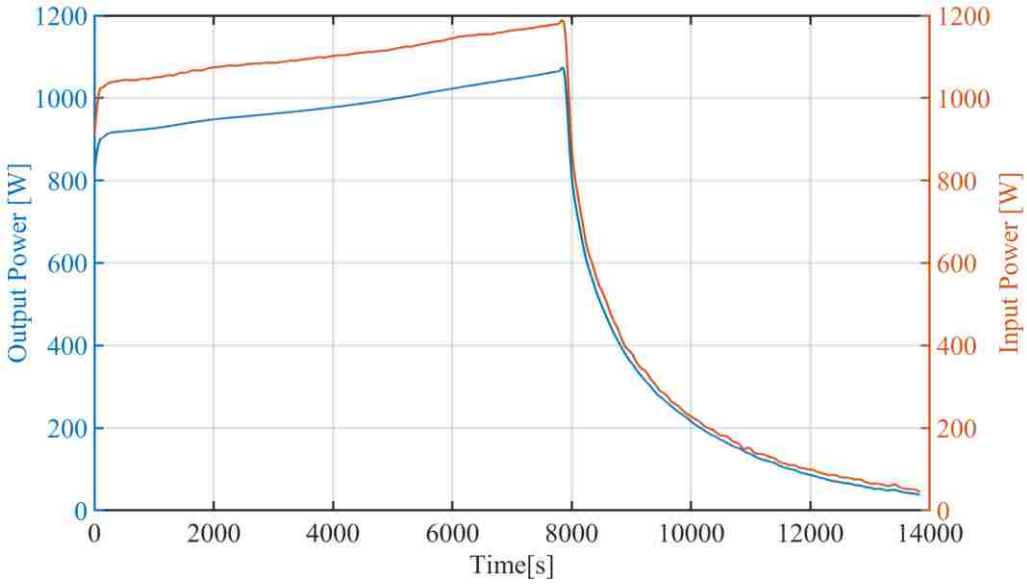

(b)

Figure 9.11. Experimental results of charging battery for WPT system (25 turns primary and 25 turns secondary) with primary LCC compensation (a) output voltage and current (b) input and output power.

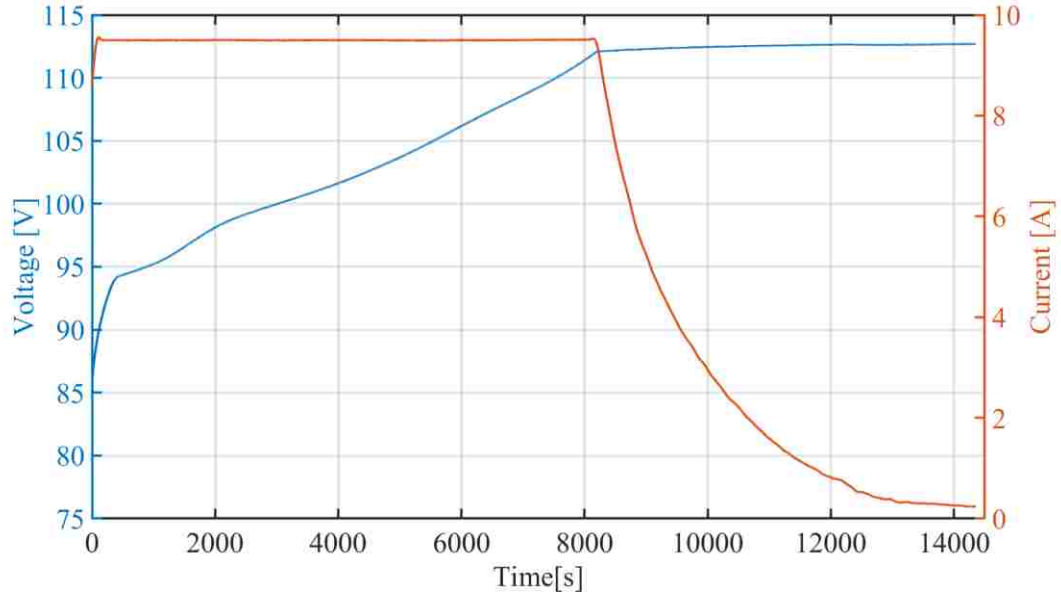

(a)

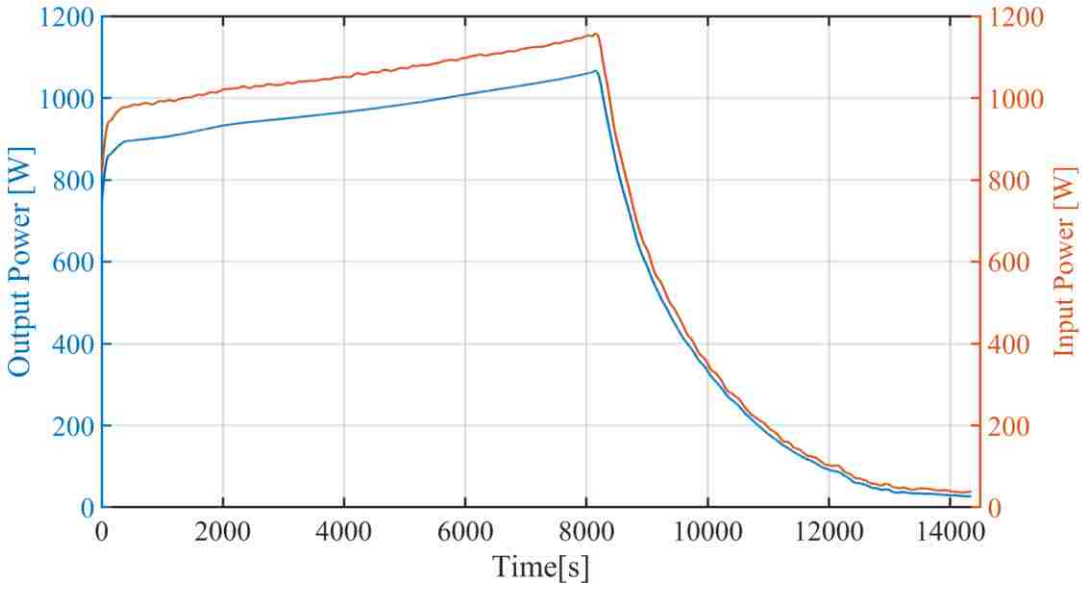

(b)

Figure 9.12. Experimental results of charging battery for WPT system (25 turns primary and 14 turns secondary) with primary LCC compensation (a) output voltage and current (b) input and output power.

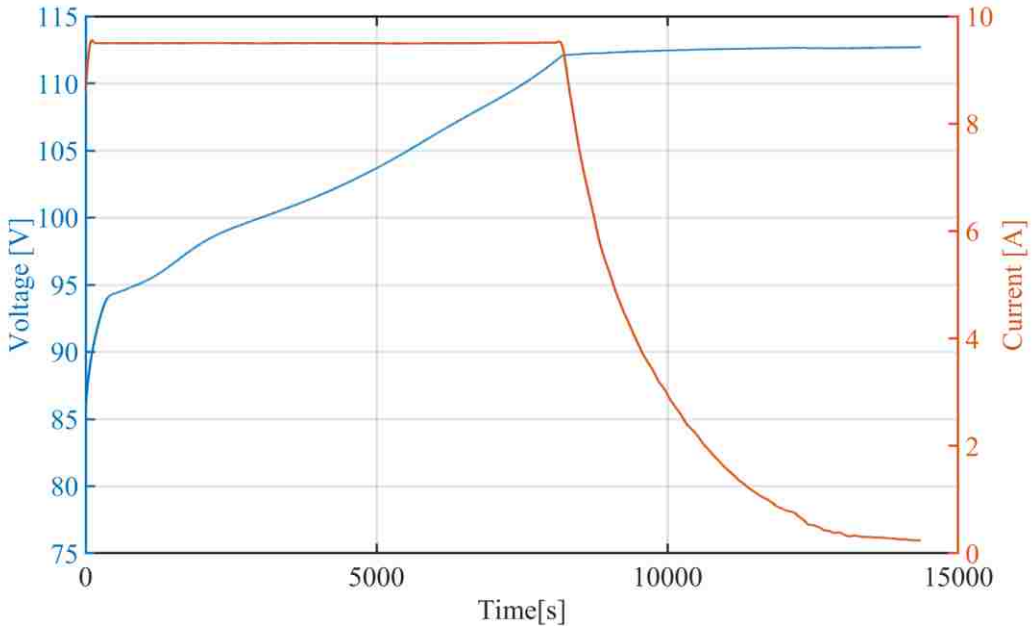

(a)

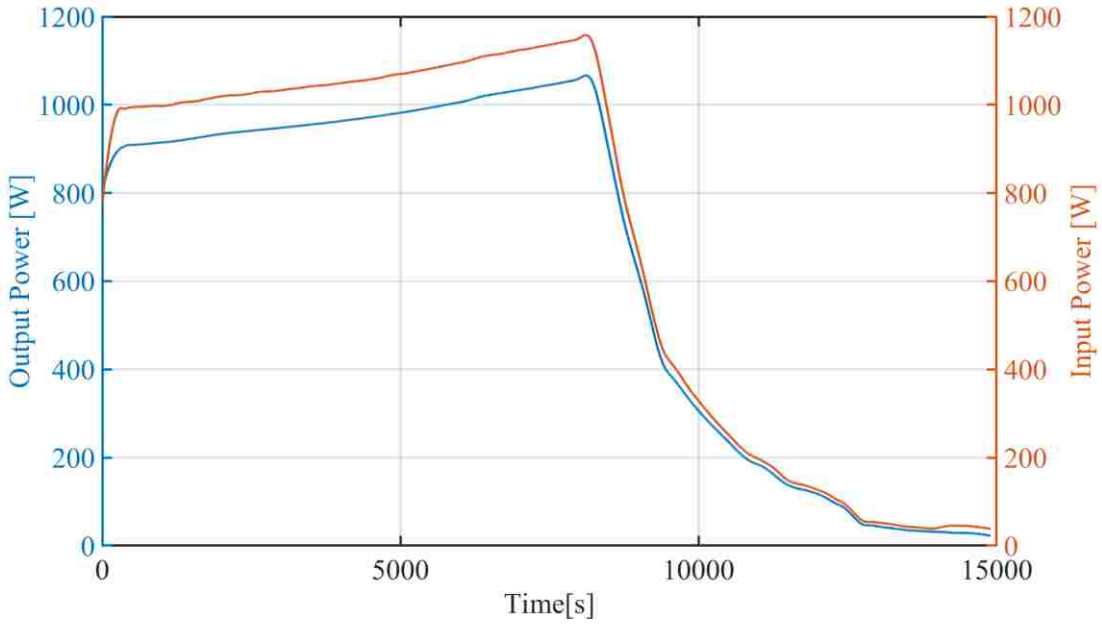

(b)

Figure 9.13. Experimental results of charging battery for WPT system (25 turns primary and 25 turns secondary) with secondary LCC compensation (a) output voltage and current (b) input and output power.

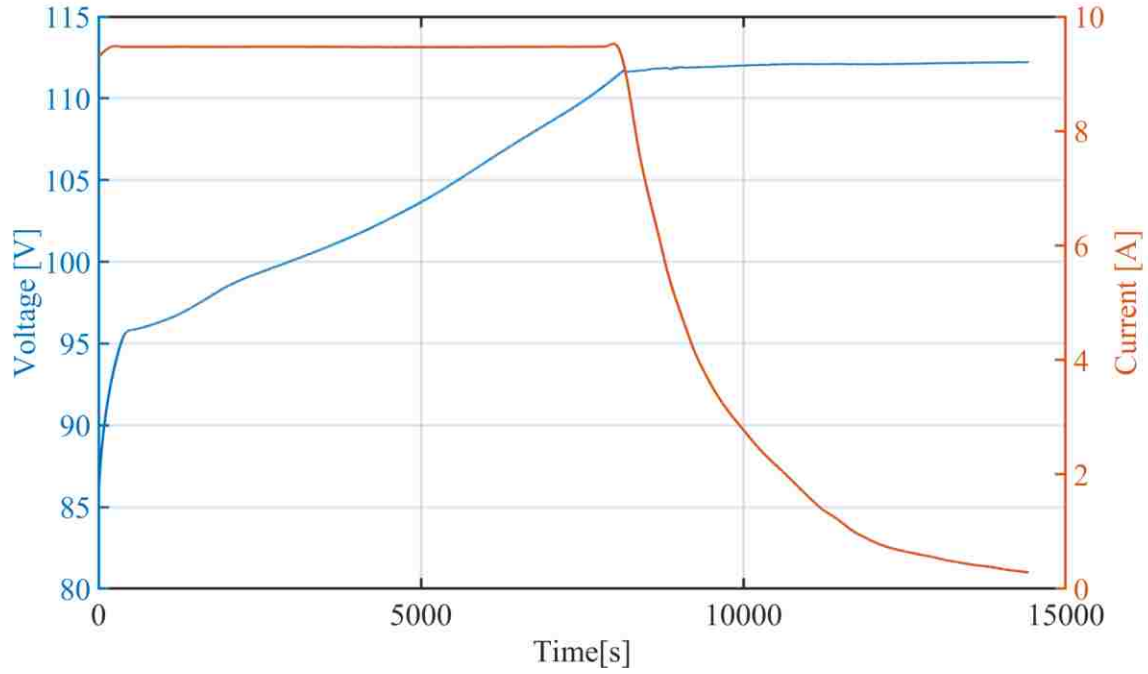

(a)

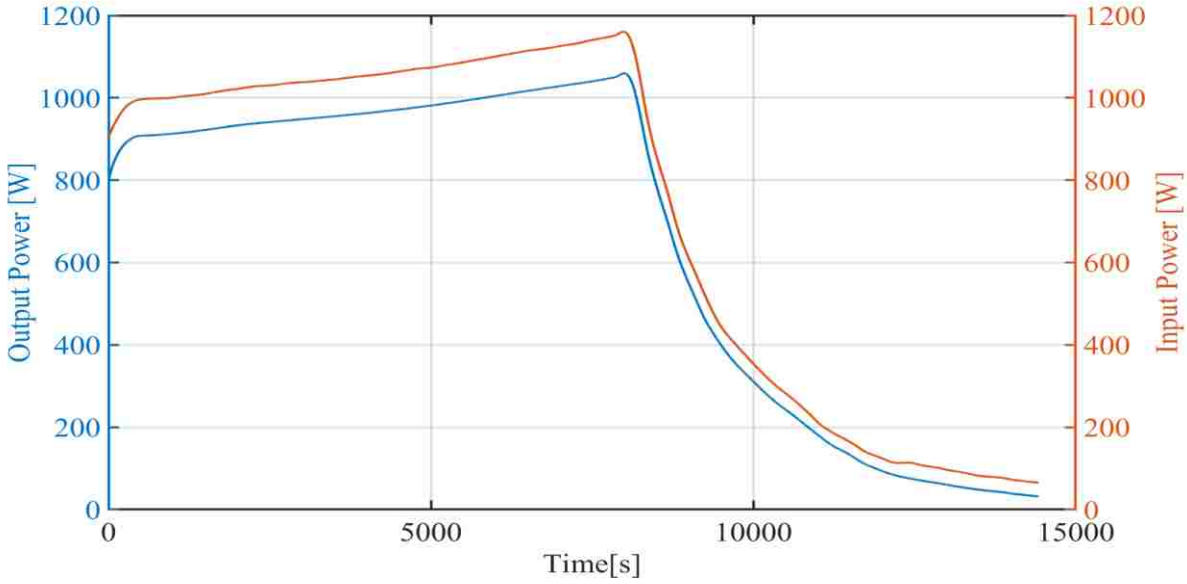

(b)

Figure 9.14. Experimental results of charging battery for WPT system (14 turns primary and 25 turns secondary) with secondary LCC compensation (a) output voltage and current (b) input and output power.

10. CONCLUSION

The interplay between the compensation topology and coil design in WPT systems is demonstrated. Two compensation topologies, i.e. primary LCC and secondary LCC, have been presented and their characteristics such as load-independent VTR and ZPA have been analyzed. Mathematical expressions for calculating the efficiency of each power conversion stage in the WPT system is provided. A novel characteristic, i.e. TWTAE, is defined and used in coil design for improving the overall efficiency. It has been shown that although increasing inductance of the coils or quality factor can improve the system maximum efficiency, it may have negative impact on TWTAE depending on the compensation topology. Therefore, the coil design must be conducted by considering compensation topology. In addition, improving quality factor of the coils may not always lead to the best results. A prototype of the WPT system is designed and built to experimentally verify the proposed theories. Experimental results demonstrate the efficiency improvement under the proposed coil and compensation design procedure.

11. FUTURE WORKS

As future work, the following tasks are suggested

- Detailed analysis of effects of frequency control based on the input impedance of the WPT system and load control to achieve optimum efficiency in design of the compensation network and coils considering the real system's requirements.
- Comparing circular and square shape coils based on system average efficiency and used materials.
- Developing a three-coil system with high robustness against misalignments.
- Proposing a compensation network to provide constant output voltage characteristics for three-coil system.

REFERENCES

[1] R. Severns, E. Yeow, G. Woody, J. Hall, and J. Hayes, "An ultra-compact transformer for a 100 W to 120 kW inductive coupler for electric vehicle battery charging," in *Proc. APEC*, 1996, vol. 1, pp. 32–38.

[2] K. W. Klontz, D. M. Divan, and D. W. Novotny, "An actively cooled 120 kW coaxial winding transformer for fast charging electric vehicles," *IEEE Trans. Ind. Appl*., vol. 31, no. 6, pp. 1257–1263, Nov./Dec. 1995.

[3] S. Mohan, M. del Mar Hershenson, S. P. Boyd and T. H. Lee, "Simple accurate expressions for planar spiral inductances," in *IEEE Journal of Solid-State Circuits*, vol. 34, no. 10, pp. 1419-1424, Oct 1999.

[4] Y. T. Jang and M. M. Jovanovic, "A contactless electrical energy transmission system for portable-telephone battery chargers*," IEEE Trans. Ind. Electron*., vol. 50, no. 3, pp. 520–527, Jun. 2003.

[5] W. Chwei-Sen, G. A. Covic, and O. H. Stielau, "Power transfer capability and bifurcation phenomena of loosely coupled inductive power transfer systems," *IEEE Trans. Ind. Electron*., vol. 51, no. 1, pp. 148–157, Feb. 2004.

[6] Chwei-Sen Wang, O. H. Stielau and G. A. Covic, "Design considerations for a contactless electric vehicle battery charger," *IEEE Trans. on Ind. Electron*., vol. 52, no. 5, pp. 1308-1314, Oct. 2005.

[7] H. L. Li, A. P. Hu, G. A. Covic, and T. Chunsen, "A new primary power regulation method for contactless power transfer," in *Proc. IEEE ICIT,* Feb. 2009, pp. 1–5.

[8] J. U. W. Hsu, A. P. Hu, and A. Swain, "A wireless power pickup based on directional tuning control of magnetic amplifier," *IEEE Trans. Ind. Electron*., vol. 56, no. 7, pp. 2771–2781, Jul. 2009.

[9] N. A. Keeling, G. A. Covic and J. T. Boys, "A Unity-Power-Factor IPT Pickup for High-Power Applications," *IEEE Trans. Ind. Electron*., vol. 57, no. 2, pp. 744-751, Feb. 2010.

[10] A. P. Sample, D. T. Meyer and J. R. Smith, "Analysis, Experimental Results, and Range Adaptation of Magnetically Coupled Resonators for Wireless Power Transfer," *IEEE Trans. Ind. Electron*., vol. 58, no. 2, pp. 544-554, Feb. 2011.

[11] M. Budhia, G. A. Covic and J. T. Boys, "Design and Optimization of Circular Magnetic Structures for Lumped Inductive Power Transfer Systems*," IEEE Trans. Power Electron*., vol. 26, no. 11, pp. 3096-3108, Nov. 2011.

[12] G. A. Covic, M. L. G. Kissin, D. Kacprzak, N. Clausen and H. Hao, "A bipolar primary pad topology for EV stationary charging and highway power by inductive coupling," 2011 *IEEE Energy Conversion Congress and Exposition*, Phoenix, AZ, 2011, pp. 1832-1838.

[13] T. Imura and Y. Hori, "Maximizing air gap and efficiency of magentic resonant coupling for wireless power transfer using equivalent circuit and Neumann formula," *IEEE Trans. Ind. Electron*., vol. 58, no. 10, pp. 4746– 4752, Oct. 2011.

[14] Z. Pantic, B. Sanzhong, and S. Lukic, "ZCS LCC-compensated resonant inverter for inductive-power-transfer application," *IEEE Trans. Ind. Electron*., vol. 58, no. 8, pp. 3500–3510, Aug. 2011.

[15] A. K. Ramrakhyani, S. Mirabbasi, and M. Chiao, "Design and optimization of resonance-based efficient wireless power delivery systems for biomedical implants," *IEEE Trans. Biomed. Circuits Syst*., vol. 5, no. 1, pp. 48–63, Feb. 2011.

[16] O. Lucia, L. A. Barragan, J. M. Burdio, O. Jim´enez, and D. Navarro, "A versatile power electronics test-bench architecture applied to domestic induction heating," *IEEE Trans. Ind. Electron*., vol. 58, no. 3, pp. 998–1007, Mar. 2011.

[17] N. Shinohara, "Power without wires*," IEEE Microw. Mag*., vol. 12, no. 7,pp. S64–S73, Dec. 2011.

[18] F. Zhang, S. Hackworth, W. Fu, C. Li, Z. Mao, and M. Sun, "Relay effect of wireless power transfer using strongly coupled magnetic resonances," *IEEE Trans. Magn*., vol. 47, no. 5, pp. 1478–1481, May 2011.

[19] W. X. Zhong, L. Xun, and S. Y. R. Hui, "A novel single-layer winding array and receiver coil structure for contactless battery charging systems with free-positioning and localized charging features," *IEEE Trans. Ind. Electron*., vol. 58, no. 9, pp. 4136–4144, Sep. 2011.

[20] J. L. Villa, J. Sallan, J. F. S. Osorio, and A. Llombart, "High misalignment tolerant compensation topology for ICPT systems," *IEEE Trans. Ind. Electron*., vol. 59, no. 2, pp. 945–951, Feb. 2012.

[21] S. Lee, G. Jung, S. Shin, Y. Kim, B. Song, J. Shin, and D. Cho, "The optimal design of high-powered power supply modules for wireless power transferred train" in *Proc. Electr. Syst. Aircraft, Railway Ship Propulsion*, 2012, pp. 1–4.

[22] J. M. Miller, C. P. White, O. C. Onar, and P. M. Ryan, "Grid side regulation of wireless power charging of plug-in electric vehicles," in *Proc. IEEE ECCE*, Sep. 2012, pp. 261–268.

[23] H. H. Wu, A. Gilchrist, K. D. Sealy, and D. Bronson, "A high efficiency 5 kW inductive charger for EVs using dual side control," *IEEE Trans. Ind. Informat.*, vol. 8, no. 3, pp. 585–595, Aug. 2012.

[24] B. H. Waters, A. P. Sample, P. Bonde, and J. R. Smith, "Powering a ventricular assist device (VAD) with the free-range resonant electrical energy delivery (FREE-D) system," *Proc. IEEE*, vol. 100, no. 1, pp. 138–149, Jan. 2012.

[25] N. Y. Kim, K. Y. Kim, J. Choi, and C. W. Kim, "Adaptive frequency with power-level tracking system for efficient magnetic resonance wireless power transfer," *Electron. Lett.*, vol. 48, no. 8, pp. 452–454, Apr. 2012.

[26] C. Auvigne, P. Germano, D. Ladas, and Y. Perriard, "A dual-topology ICPT applied to an electric vehicle battery charger," in Proc. 20th ICEM, 2012, pp. 2287–2292.

[27] M. Budhia, J. T. Boys, G. A. Covic, and H. Chang-Yu, "Development of a single-sided flux magnetic coupler for electric vehicle IPT charging systems," *IEEE Trans. Ind. Electron.*, vol. 60, no. 1, pp. 318–328, Jan. 2013.

[28] L. Chen, S. Liu, Y. C. Zhou, and T. J. Cui, "An optimizable circuit structure for high-efficiency wireless power transfer," *IEEE Trans. Ind. Electron.*, vol. 60, no. 1, pp. 339–349, Jan. 2011.

[29] W. Zhong, C. K. Lee, and S. Hui, "General analysis on the use of tesla's resonators in domino forms for wireless power transfer," *IEEE Trans. Ind. Electron.*, vol. 60, no. 1, pp. 261–270, Jan. 2013.

[30] D. Ahn and S. Hong, "A study on magnetic field repeater in wireless power transfer," *IEEE Trans. Ind. Electron.*, vol. 60, no. 1, pp. 360–371, Jan. 2013.

[31] T. C. Beh, M. Kato, T. Imura, S. Oh, and Y. Hori, "Automated impedance matching system for robust wireless power transfer via magnetic resonance coupling," *IEEE Trans. Ind. Electron.*, vol. 60, no. 9, pp. 3689–3698, Sep. 2013.

[32] S. Moon, B. C. Kim, S. Y. Cho, C. H. Ahn and G. W. Moon, "Analysis and Design of a Wireless Power Transfer System With an Intermediate Coil for High Efficiency," *IEEE Trans. Ind. Electron.*, vol. 61, no. 11, pp. 5861-5870, Nov. 2014.

[33] H. Li, J. Li, K. Wang, W. Chen and X. Yang, "A Maximum Efficiency Point Tracking Control Scheme for Wireless Power Transfer Systems Using Magnetic Resonant Coupling," *IEEE Trans. Power Electron.*, vol. 30, no. 7, pp. 3998-4008, July 2015.

[34] K. Lee, Z. Pantic, and S. Lukic, "Reflexive field containment in dynamic inductive power transfer systems," *IEEE Trans. Power Electron.*, vol. 9, no. 9, pp. 4592–4602, Sep. 2014.

[35] W. Zhang, S. C. Wong, C. K. Tse, and Q. Chen, "Design for efficiency optimization and voltage controllability of series-series compensated inductive power transfer systems," *IEEE Trans. Power Electron.*, vol. 29, no. 1, pp. 191–200, Jan. 2014.

[36] W. Zhang, S.-C. Wong, C. K. Tse, and Q. Chen, "Analysis and comparison of secondary series- and parallel-compensated inductive power transfer systems operating for optimal efficiency and load-independent voltage-transfer ratio," *IEEE Trans. Power Electron.*, vol. 29, no. 6, pp. 2979–2990, Jun. 2014.

[37] V. Jiwariyavej, T. Imura, and Y. Hori, "Coupling coefficients estimation of wireless power transfer system via magnetic resonance coupling using information from either side of the system," *IEEE J. Emerg. Sel. Topics Power Electron*., vol. 3, no. 1, pp. 191–200, Jun. 2014.

[38] J. M. Miller, O. C. Onar and M. Chinthavali, "Primary-Side Power Flow Control of Wireless Power Transfer for Electric Vehicle Charging," *IEEE J. Emerg. Sel. Topics Power Electron*., vol. 3, no. 1, pp. 147-162, March 2015.

[39] R. Bosshard, J. W. Kolar, J. Mühlethaler, I. Stevanović, B. Wunsch and F. Canales, "Modeling and η- α-Pareto Optimization of Inductive Power Transfer Coils for Electric Vehicles," *IEEE J. Emerg. Sel. Topics Power Electron*., vol. 3, no. 1, pp. 50-64, March 2015.

[40] G. Buja, M. Bertoluzzo, and K. N. Mude, "Design and experimentation of WPT charger for electric city car," *IEEE Trans. Ind. Electron*., vol. 62, no. 12, pp. 7436–7447, Dec. 2015.

[41] S. Li and C. Mi, "Wireless power transfer for electric vehicle applications," *IEEE J. Emerg. Sel. Topics Power Electron*., vol. 3, no. 1, pp. 4–17, Mar. 2015.

[42] Y.-L. Lyu et al., "A method of using nonidentical resonant coils for frequency splitting elimination in wireless power transfer*," IEEE Trans. Power Electron*., vol. 30, no. 11, pp. 6097–6107, Nov. 2014

[43] A. Zaheer, H. Hao, G. A. Covic, and D. Kacprzak, "Investigation of multiple decoupled coil primary pad topologies in lumped IPT systems for interoperable electric vehicle charging," *IEEE Trans. Power Electron.*, vol. 30, no. 4, pp. 1937–1955, Apr. 2015.

[44] F. Y. Lin, G. Covic, and J. Boys, "Evaluation of magnetic pad sizes and topologies for electric vehicle charging," *IEEE Trans. Power Electron*., vol. 30, no. 11, pp. 6391–6407, Nov. 2015.

[45] M. Ibrahim, L. Bernard, L. Pichon, E. Laboure, A. Razek, O. Cayol, D. Ladas, and J. Irving, "Inductive charger for electric vehicle: Advanced modeling and interoperability analysis*," IEEE Trans. Power Electron*., 2016, to be published.

[46] C. Zheng, J. Lai, and L. Zhang, "Design consideration to reduce gap variation and misalignment effects for the inductive power transfer system*," IEEE Trans. Power Electron*., vol. 30, no. 11, pp. 6108–6119, Nov. 2015.

[47] W. Zhang, J. C. White, A. M. Abraham, and C. C. Mi, "Loosely coupled transformer structure and interoperability study for EV wireless charging systems," *IEEE Trans. Power Electron*., vol. 30, no. 11, pp. 6356–6367, Nov. 2015.

[48] W. X. Zhong and S. Y. R. Hui, "Maximum energy efficiency tracking for wireless power transfer systems," *IEEE Trans. Power Electron*., vol. 30, no. 7, pp. 4025–4034, Jul. 2015.

[49] D. Kobayashi, T. Imura, and Y. Hori, “Real-time coupling coefficient estimation and maximum efficiency control on dynamic wireless power transfer for electric vehicles,” in *Proc. IEEE PELS Workshop Emerging Technol.: Wireless Power*, 2015, pp. 1–6.

[50] M. Fu, H. Yin, X. Zhu, and C. Ma, “Analysis and tracking of optimal load in wireless power transfer systems,” *IEEE Trans. Power Electron.*, vol. 30, no. 7, pp. 3952–3963, Jul. 2015.

[51] 2015-B. Esteban, M. Sid-Ahmed and N. C. Kar, “A Comparative Study of Power Supply Architectures in Wireless EV Charging Systems*,” IEEE Trans. Power Electron*., vol. 30, no. 11, pp. 6408-6422, Nov. 2015.

[52] S. Y. Hoon, B. H. Choi, E. S. Lee, and C. T. Rim, “General unified analyses of two-capacitor inductive power transfer systems: Equivalence of currentsource SS and SP compensations*,” IEEE Trans. Power Electron*., vol. 30, no. 11, pp. 6030–6045, Nov. 2015.

[53] S. Li, W. Li, J. Deng, T. D. Nguyen, and C. C. Mi, “A double-sided LCC compensation network and its tuning method for wireless power transfer,” *IEEE Trans. Veh. Technol*., vol. 64, no. 6, pp. 2261–2273, Jun. 2015.

[54] D. Xin, L. Weiyi, L. Yanling, S. Yugang, T. Chunsen, W. Zhihui, and S. Yue, “Improved LCL resonant network for Inductive Power Transfer system,” in 2015 *IEEE PELS Workshop on Emerging Technologies: Wireless Power* (WoW), 2015, pp. 1–5.

[55] W. Li, H. Zhao, J. Deng, S. Li, and C. C. Mi, “Comparison study on SS and double-sided LCC compensation topologies for EV/PHEV wireless chargers,” *IEEE Trans. Veh. Technol.*, vol. 65, no. 6, pp. 4429–4439, Jun. 2016.

[56] H. Z. Z. Beh, G. A. Covic, and J. T. Boys, “Investigation of magnetic couplers in bicycle kickstands for wireless charging of electric bicycles,” *IEEE J. Emerging Select. Topics Power Electron.*, vol. 3, no. 1, pp. 87–100, Mar. 2015.

[57] W. Zhong, C. Zhang, X. Liu, and S. Hui, “A methodology for making a three-coil wireless power transfer system more energy efficient than a two-coil counterpart for extended transfer distance,” *IEEE Trans. Power Electron.*, vol. 30, no. 2, pp. 933–942, Feb. 2015.

[58] D. Kobayashi, T. Imura, and Y. Hori, “Real-time coupling coefficient estimation and maximum efficiency control on dynamic wireless power transfer for electric vehicles,” in *Proc. IEEE PELS Workshop Emerging Technol*., Wireless Power, 2015, pp. 1–6.

[59] W. Zhang and C. C. Mi, “Compensation topologies for high power wireless power transfer systems,” *IEEE Trans. Veh. Technol*., vol. PP, no. 99, pp. 1–10, Jul. 2015.

[60] S. Moon and G. W. Moon, “Wireless Power Transfer System with an Asymmetric Four-Coil Resonator for Electric Vehicle Battery Chargers,” *IEEE Trans. Power Electron*., vol. 31, no. 10, pp. 6844–6854, Oct. 2016.

[61] R. Tavakoli, A. Jovicic, N. Chandrappa, R. Bohm and Z. Pantic, "Design of a dual-loop controller for in-motion wireless charging of an electric bus," 2016 *IEEE Energy Conversion Congress and Exposition* (ECCE), Milwaukee, WI, 2016, pp. 1-8.

[62] H. Feng, T. Cai, S. Duan, J. Zhao, X. Zhang, and C. Chen, "An LCC compensated resonant converter optimized for robust reaction to large coupling variation in dynamic wireless power transfer," *IEEE Trans. Ind. Electron*., vol. 63, no. 10, pp. 6591–6601, Oct. 2016.

[63] J. Zhang, X. Yuan, C. Wang, and Y. He, "Comparative analysis of two-coil and three-coil structure for wireless power transfer," *IEEE Trans. Power Electron*., vol. 32, no. 1, pp. 341–352, Jan. 2017.

[64] R. Mai, Y. Liu, Y. Li, P. Yue, G. Cao, and Z. He, "An active rectifier based maximum efficiency tracking method using an additional measurement coil for wireless power transfer," *IEEE Trans. Power Electron*., (early access).

[65] X. Dai, X. Li, Y. Li, and P. Hu "Maximum efficiency tracking for wireless power transfer systems with dynamic coupling coefficient estimation," *IEEE Trans. Power Electron*, vol. 33, no. 6, pp. 5005-5015, 2018.

[66] D. Ahn, "Transmitter Coil Resonant Frequency Selection for Wireless Power Transfer," *IEEE Trans. Power Electron.*, vol. 33, no. 6, pp. 5029-5041, June 2018.

[67] Yijie Wang, Yousu Yao, Xiaosheng Liu, Dianguo Xu, and Liang Cai, "An LC/S Compensation Topology and Coil Design Technique for Wireless Power Transfer*," IEEE Trans. Power. Electron.*, vol. 33, no.3, Mar. 2018.

[68] 2018- D. Patil, M. K. McDonough, J. M. Miller, B. Fahimi and P. T. Balsara, "Wireless Power Transfer for Vehicular Applications: Overview and Challenges," *IEEE Trans. Transp. Electrific*, vol. 4, no. 1, pp. 3-37, March 2018.

[69] Tavakoli, Reza, and Zeljko Pantic, "Analysis, Design, and Demonstration of a 25-kW Dynamic Wireless Charging System for Roadway Electric Vehicles" *IEEE J. Emerging Select. Topics Power Electron.*, vol. 6, no. 3, pp. 1378-1393, Sept. 2018.

[70] M. Lu and K. D. T. Ngo, "Systematic Design of Coils in Series–Series Inductive Power Transfer for Power Transferability and Efficiency" *IEEE Trans. Power Electron.*, vol. 33, no. 4, pp. 3333-3345, April 2018.

VITA

Amir Masoud Bozorgi received his B.S. and M.Sc. in Electrical Engineering from Ferdowsi University of Mashhad, Mashhad, Iran, in 2010 and 2013, respectively. His research areas include electric vehicles, modeling and control of power electronics converters and control of electric machine drives. During his PhD program, he published more than ten journal and conference papers. He will receive his PhD degree Electrical and Electronics Engineering from Louisiana State University (LSU), Baton Rouge, LA, USA, in May 2019. After his graduation, he will start his job at Danfoss Turbocor, Tallahassee, FL.